学位論文

Search for Axion Like Particles using Laue-case Conversion in a Single Crystal

**（単結晶中におけるラウエ型変換を用いた
アクシオン様粒子の探索）**

平成 29 年 12 月博士（理学） 申請

東京大学大学院理学系研究科
物理学専攻
山道　智博

Abstract

This thesis proposes and performs an X-ray Light Shinning through a Wall (LSW) search for Axion Like Particles (ALPs) using a Laue-case conversion within a crystal. Compared to prior LSW experiments using external magnetic fields, the X rays-ALPs conversion has two advantages. Firstly, periodic electric fields within crystals are as high as 10^{11} V/m, which correspond to high magnetic fields of $\sim 10^3$ T. Secondly, the sensitive ALPs' mass can reach $m_a = 10$ keV by detuning an X-ray injection angle from the Bragg angle. The X rays-ALPs conversion can provide an additional experimental scheme for the model-independent search for heavy ALPs.

A LSW experiment using the conversion scheme is performed at a third-generation X-ray synchrotron radiation facility, BL19LXU beam line of SPring-8. A novel X ray-ALP conversion system is developed by using a silicon channel-cut crystal with two 600 μm-thick blades. X rays from the beam line are converted into ALPs by the first blade, and then converted ALPs are subsequently reconverted into detectable X rays by the second blade. No significant signals were observed, and a 90% C.L. upper limit on the ALPs-two photon coupling constant is obtained as follows,

$$g_{a\gamma\gamma} < 4.2 \times 10^{-3}\ \mathrm{GeV}^{-1}\ (m_a < 10\ \mathrm{eV}), \quad (1)$$

$$g_{a\gamma\gamma} < 5.0 \times 10^{-3}\ \mathrm{GeV}^{-1}\ (46\ \mathrm{eV} < m_a < 1020\ \mathrm{eV}). \quad (2)$$

This limit is the most stringent limit on ALPs in the sub-keV region as a model-independent laboratorial search.

Contents

List of Figures

List of Tables

Chapter 1

Introduction

This thesis describes a search for Axion-Like-Particles (ALPs) using atomic electric fields in single crystals. ALPs are particles predicted by theories Beyond the Standard Model (BSM). ALPs have properties similar to a pseudo-scalar unknown particle, axion, as their name suggests. A theoretical background for the axion and ALPs is shown firstly in this section. Prior searches for ALPs are introduced secondly. The new experimental scheme will be introduced finally. I distinguish discussion about the standard axion and ALPs by using subscriptions "A" for the axion and "a" for ALPs, respectively, in this thesis.

1.1 Axion

Axion is a pseudo-scalar particle predicted in association with a puzzle referred to as 'strong CP problem'. A theoretical background and properties of axion are introduced briefly in the following subsections.

1.1.1 Strong CP problem

The Standard Model (SM) of particle physics predicts that fundamental forces have CP-violating interactions. A CP-violating effect can take place due to configurations of the vacuum in the quantum-chromodynamics (QCD) [2–5]. The QCD vacuum can have states topologically different from each other. These states are labelled by a phase parameter, θ (0 to 2π). The vacuum parameter introduces an additional term to the QCD Lagrangian as follows,

$$\mathcal{L}_{\mathrm{int},\theta} = \theta \frac{\alpha_s}{4\pi} \mathcal{G}^{b\mu\nu} \tilde{\mathcal{G}}^{b}_{\mu\nu}, \tag{1.1}$$

where $\mathcal{G}^{b}_{\mu\nu}$ is the gluonic field strength tensor, $\tilde{\mathcal{G}}^{b}_{\mu\nu}$ is its dual, $\alpha_s \equiv \frac{g_s^2}{8\pi}$ is the strong coupling constant. The additional term provides finite contribution to the neutron electric dipole moment (EDM), d_n, via a coupling between pions and nucleons. The

contribution can be expressed as follows [6, 7],

$$d_n = -3.3 \times 10^{-16} \bar{\theta}\ e \cdot \mathrm{cm}, \tag{1.2}$$
$$\bar{\theta} = \theta + \mathrm{argdet} M, \tag{1.3}$$

where e is the elementary charge and M is the quark mass matrix. $\bar{\theta}$ is expected to be $\mathcal{O}(1)$ since $\bar{\theta}$ is made up of the unrelated parameters, θ and M. However, the current upper limit on the neutron EDM is much tinier as follows [8, 9],

$$d_n < 3.0 \times 10^{-26}\ e \cdot \mathrm{cm}\ (90\%\ \mathrm{C.L.}). \tag{1.4}$$

The parameters, θ and $\mathrm{argdet} M$, should cancel each other with the precision of 10^{-10} to explain the upper limit. The fine-tuning problem is referred to as the strong CP problem.

A BSM theory introducing an additional $U(1)$ symmetry, $U(1)_{\mathrm{PQ}}$, was introduced to resolve the problem [10, 11]. The theory prompts the vacuum parameter, $\bar{\theta}$, to a dynamical massless field, A, with a global $U(1)$ symmetry. The field can interact with photons, gluons and other particles in SM. The low-energy effective Lagrangian involving the dynamical field, photons and gluons can be represented as follows [6],

$$\mathcal{L}_A = \frac{1}{2}\partial_\mu A \partial^\mu A + \frac{\alpha_s}{4\pi f_A} A \mathcal{G}^{b\mu\nu} \tilde{\mathcal{G}}^b_{\mu\nu} + \frac{s\alpha}{8\pi f_A} A \mathcal{F}^{\mu\nu} \tilde{\mathcal{F}}_{\mu\nu}, \tag{1.5}$$

where f_A is a symmetry breaking scale, s is a model-independent parameter, α is the fine structure constant, $\mathcal{F}^{\mu\nu}$ is the electromagnetic field strength tensor and $\tilde{\mathcal{F}_{\mu\nu}}$ is its dual. The parameter, $\bar{\theta}$, can be absorbed into the second term of Eq. (1.5) by shifting A to $A = A' - \bar{\theta} f_A$. The term containing $\bar{\theta}$ can be automatically reduced to zero when the $U(1)$ symmetry is spontaneously broken into a preferred vacuum with $\langle \bar{A} \rangle = 0$. The mechanism resolves the fine tuning problem of $\bar{\theta}$.

1.1.2 Axion and its property

The spontaneous symmetry breaking of $U(1)_{\mathrm{PQ}}$ generates inevitably a neutral pseudo-Nambu-Goldstone boson referred to as axion [12, 13]. The axion obtains mass, m_A, by mixing with neutral mesons such as π^0. The general expression for the axion mass can be obtained by using chiral perturbation theory as follows [14, 15],

$$m_A = \frac{m_\pi f_\pi}{f_A} \frac{\sqrt{z}}{1+z} \simeq 0.6\ \mathrm{meV} \times \left(\frac{10^{10}\ \mathrm{GeV}}{f_A} \right), \tag{1.6}$$

where m_π is the pion mass, f_π is the pion decay constant and $z = \frac{m_u}{m_d} \sim 0.56$ is the ratio of the up-quark mass to the down-quark mass [16].

The axion can interact with two photons via an anomaly diagram of exotic fermions with $U(1)_{\mathrm{PQ}}$ charges. The interaction can be described by the following Lagrangian,

$$\mathcal{L}_{A\gamma\gamma} = -\frac{1}{4} g_{A\gamma\gamma} A \mathcal{F}_{\mu\nu} \tilde{\mathcal{F}}^{\mu\nu} = g_{A\gamma\gamma} A \mathbf{E} \cdot \mathbf{B} \tag{1.7}$$

where $\mathbf{E} \cdot \mathbf{B}$ is the odd-parity product of electromagnetic fields and $g_{A\gamma\gamma}$ is an axion-two photon coupling constant. The coupling constant depends on the electromagnetic and color anomalies of exotic fermions. The interaction mediates a mixing of axions and photons in external electromagnetic fields. The mixing interaction is referred to as the Primakoff effect [17, 18]. The coupling constant can be described as follows [19–21],

$$g_{A\gamma\gamma} = \frac{\alpha}{2\pi f_A}\left(\frac{E}{N} - \frac{2}{3}\frac{1+4z}{1+z}\right) = \frac{\alpha}{2\pi}\left(\frac{E}{N} - 1.95\right)\frac{1+z}{\sqrt{z}}\frac{m_A}{m_\pi f_\pi} \tag{1.8}$$

$$\sim 10^{-13}\ \mathrm{GeV}^{-1} \times \left(\frac{10^{10}\ \mathrm{GeV}^{-1}}{f_A}\right). \tag{1.9}$$

The coupling constant is proportional to the axion mass. The proportionality factor between m_A and $g_{A\gamma\gamma}$ is determined by the model-dependent ratio $\frac{E}{N}$, where E is the electromagnetic anomaly and N is the color anomaly.

1.1.3 Invisible axion models

The axion mass and couplings to SM particles can be roughly parameterized by the symmetry breaking scale, f_A. The original axion model, PQWW axion [10–13], assumes that f_a is the order of the electroweak scale, and that the axion mass is $\sim$ 100 keV. Axion models with much higher scales and much weaker couplings were proposed after the PQWW axion had been excluded by extensive efforts. These models referred to as 'invisible axion models' have two major branches: KSVZ [22, 23] and DFSZ models [24, 25].

KSVZ model

KSVZ models assume that $U(1)_{\mathrm{PQ}}$ charges are carried only by exotic colored fermions. The symmetry breaking scale of KSVZ models can be arbitrarily large since the force of these fermions is not responsible for the electroweak symmetry breaking. The low-energy spectrum of the theory includes composite invisible axions. These axions can couple neither to heavy quarks nor to leptons. The axions without couplings to leptons are referred to as hadronic axions. The model-dependency of axion-nucleon couplings is comparatively small for hadronic axions. On the contrary, the axion-photon coupling is strongly model-dependent because the exotic fermions can have arbitral electric charges. $\frac{E}{N}$ becomes zero when the exotic fermions are electrically neutral [20].

DFSZ model

DFSZ models require at least two Higgs doublets and assume that ordinal SM particles carry $U(1)_{\mathrm{PQ}}$ charges. DFSZ models are also referred to as Grand Unified Theories (GUT) models since these models can be easily combined with GUT. The symmetry breaking scales of GUT and DFSZ models are considered to be much

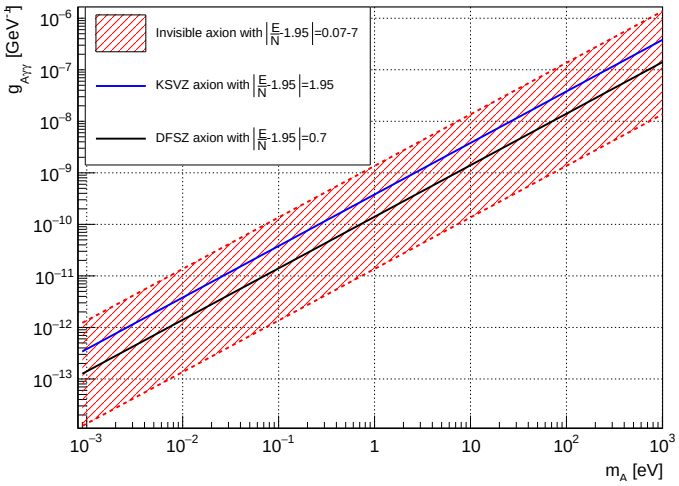

Figure 1.1: The axion mass, m_A, and the axion-two photon coupling constant, $g_{A\gamma\gamma}$, in invisible axion models. The values of m_A and $g_{A\gamma\gamma}$ are typically considered to be within the red band. The blue and black solid lines show the prediction of KSVZ models with neutral exotic fermions ($\left|\frac{E}{N} - 1.95\right| = 1.95$) and that of DFSZ models with SU(5) symmetry ($\left|\frac{E}{N} - 1.95\right| = 0.7$), respectively.

higher than the electroweak breaking scale. The axion-electrons coupling is strongly model-dependent in the DFSZ models. $\frac{E}{N}$ becomes $\frac{8}{3}$ in a SU(5) GUT theory [21].

The ratio, $\frac{E}{N}$, can take a wide range of values [26]. The coupling between hadronic axions and photons can be easily reduced by $10^{-1} \sim 10^{-2}$ when $\frac{E}{N}$ is tuned to be ~ 2 for example. The plausible range of $\left|\frac{E}{N} - 1.95\right|$ is typically between 0.07 and 7 in invisible axion models. The candidates for m_A and $g_{A\gamma\gamma}$ are represented by the red band shown in Fig. 1.1. Searches for invisible axions are equivalent to searches within the narrow band.

1.1.4 Axion Like Particles

Axion Like Particles (ALPs) are pseudo-Nambu-Goldstone bosons with properties similar to the original axion. ALPs are predicted by theories beyond the Standard Model. Theoretically-motivated candidates for ALPs are as follows [27]:

1. The axion, A, shown above.

2. Majoron [28,29], a Nambu-Goldstone boson associated with the global lepton number symmetry. The particle can provide possible explanation for the extremely tiny mass of neutrinos.

3. Familion associated with the global family symmetries [30–32]

4. ALPs arising as Kaluza-Klein zero modes of antisymmetric tensor fields in string theories [33–35].

Although ALPs have properties similar to the standard axion, the proportionality between ALPs' mass, m_a, and ALP-two photon coupling constant, $g_{a\gamma\gamma}$, are no longer related to each other. Searches for ALPs should cover the whole $m_a - g_{a\gamma\gamma}$ plane without restrictions.

In addition to the theoretical point of view, ALPs are also of astronomical interest. ALPs are viable candidates for dark matter [36, 37], and they can provide possible explanation for various astrophysical phenomena such as the transparency of the universe to high-energy photons [38, 39] and the observational dwarf luminosity function [40]. Searches for ALPs have a particular importance in astronomy as well as in elementary particle physics.

ALPs with a sub-keV mass

This thesis describes a search for ALPs with a sub-keV mass. String theories predict multiple ALPs with masses related to the compactifications of the extra dimensions in which ALPs can propagate (the forth candidate for ALPs shown above). The number of multiple ALPs can be countless since there are various ways of the compactifications. The plenitude of string ALPs is referred to as an axiverse [41–43]. The masses of ALPs may have a uniform distribution in the logarithm containing the sub-keV range.

One viable candidate for these ALPs is solar Kaluza-Klein axion [44]. Kaluza-Klein axions are string-motivated ALPs containing members with a mass of $0.1 \sim 10$ keV (sub-keV$\sim$keV range). The Kaluza-Klein axion model has an invisible (QCD) axion with a mass of m_{a_0} and the infinite number of excitations with masses of m_{a_n}. These axion fields are compactificated on a $\mathbf{Z}_2$ orbifold. Although they share the same coupling constant determined by m_{a_0}, the masses of excitations can be much heavier than m_{a_0} as follows [45],

$$m_{a_n} \simeq \frac{n}{R}, \tag{1.10}$$

$$n \equiv |\mathbf{n}| = \sqrt{n_1^2 + n_2^2 + \cdots + n_\delta^2} > 0, \tag{1.11}$$

where $R \ll m_{a_0}^{-1}$ is the compactification radius of the extra dimension, δ is the number of the extra dimension in which ALPs can propagate and $n_{1\cdots\delta}$ are integers labeling the individual excitations. The compactification also reduces the fundamental scale of the string theory, M_F, from the Plank scale. Solar Kaluza-Klein axions are produced within the sun via the Primakoff effect under the electric fields of nucleons ($\gamma Z \to aZ$) and photon coalescence ($\gamma\gamma \to a$). Some of solar Kaluza-Klein axions (mainly produced by photon coalescence) are gravitationally trapped by the sun. These ALPs revolving around the sun act as an X-ray source between the sun and the earth, which explains various astrophysical phenomena shown below. Kaluza-Klein axion model with two total extra dimensions, $\delta = 2$,

$M_F = 100$ TeV, $R = 10^3$ keV^{-1} and $g_{a\gamma\gamma} = 9.2 \times 10^{-14}$ GeV^{-1} is suggested in Ref. [44] to explain an experimentally measured X-ray luminosity of the quiet sun.

Although Kaluza-Klein axion also has members within the keV-range, members with a sub-keV mass are more strongly motivated since they can provide possible explanations for the following various astrophysical phenomena [44]:

1. The anomalously high temperature of the solar corona and stellar coronae (relevant ALPs' mass: $m_a = 0.1 \sim 0.7$ keV) [46–50].

2. The observed X rays from the dark side of the moon ($m_a = 0.2 \sim 0.8$ keV) [51].

3. The soft X-ray background radiation ($m_a = 0.2 \sim 0.8$ keV) [52–55].

As shown above, ALPs with a sub-keV mass have particular theoretical and astrophysical importance, which cannot be complemented by lighter ALPs.

1.2 Previous searches for ALPs

Extensive searches have been performed so far to observe the invisible axion and ALPs. These searches will be summarized in this section. The most stringent limits on ALPs have been obtained by model-dependent searches: the observation of stellar evolution and telescope experiments. Model-independent laboratorial experiments have been performed by using the Primakoff effect in an external magnetic field. Exclusion regions obtained by these previous searches are summarized in Fig. 1.2.

1.2.1 Stellar evolution

ALPs can be generated within stellar systems via couplings to ordinal particles. These ALPs can affect the stellar evolution by enhancing the energy loss of the stellar system. Some of the most stringent constraints on ALPs are obtained by observing stellar systems such as white dwarf cooling [73,74], the SN1987A neutrino burst [75] and the absence of the SN1987A gamma-ray burst [58, 59]. The most stringent upper limit on $g_{a\gamma\gamma}$ in a broad range of m_a is obtained by observing horizontal branch (HB) stars in the open clusters M67 [56, 57].

1.2.2 Telescope experiments

Two kinds of telescope experiments have been performed to detect cosmologically generated ALPs: axion helioscope and haloscope experiments [76]. These telescope experiments convert cosmological ALPs into detectable photons by the Primakoff effect in an external magnetic field.

Axion helioscope experiments detect ALPs emitted from the sun. The sun is considered to be a potential intense source of ALPs due to intense photon density

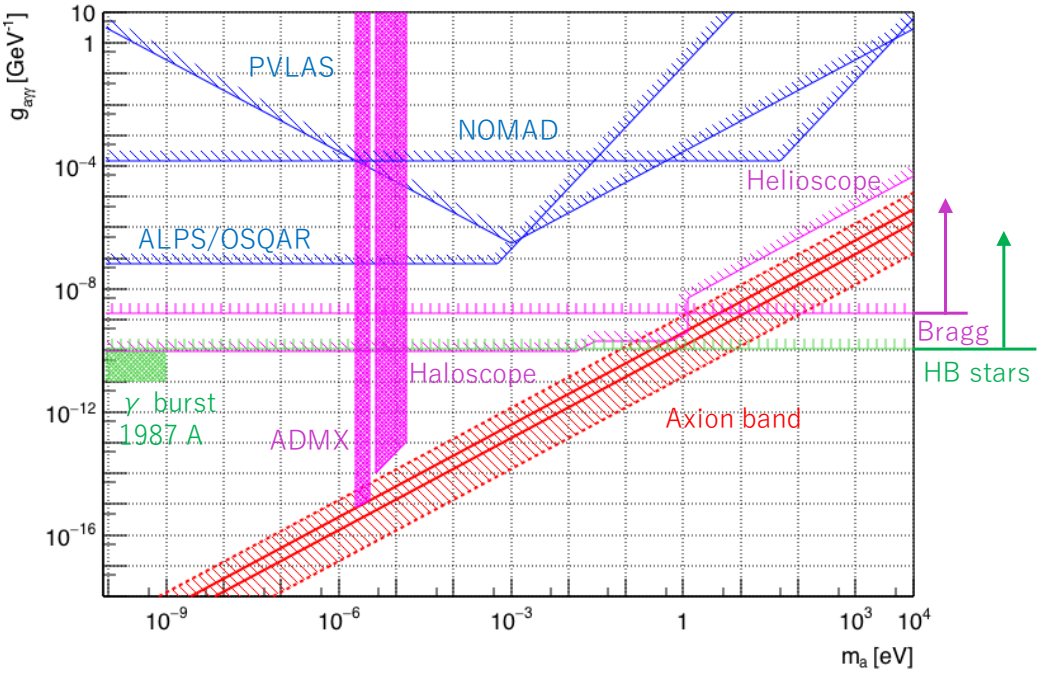

Figure 1.2: Exclusion regions on the ALPs' mass, m_a, and ALP-two photon coupling constant, $g_{a\gamma\gamma}$. The figure is cited from Ref. [6, 7]. Red: the invisible axion band shown by Fig. 1.1. Green: exclusion regions obtained from astronomical observation. The most stringent constraint on $g_{a\gamma\gamma}$ is obtained by observing HB stars [56, 57]. An exclusion region from the absence of the SN1987A gamma-ray burst [58, 59] is also shown. Pink: exclusion regions from Haloscope [60–63] and Helioscope [64] experiments. That of solar axion searches using Bragg reflection [65–68] are also shown. Blue: exclusion regions from laboratorial experiments using a LSW technique (NOMAD [69] / ALPS [70] / OSQAR [71]) and photon-photon interaction (PVLAS [72]).

and its huge volume. An axion helioscope is made up of a telescope oriented toward the sun, conversion magnets and detectors for converted photons. The axion helioscope has been utilized by CAST [64] and SUMICO [77] experiments. CAST experiment excludes KSVZ axions ($\left|\frac{E}{N} - 1.95\right| = 1.95$) in a mass range of 0.6 eV$< m_A <$1.17 eV.

The axion is also considered as a viable candidate for the dark matter. An axion haloscope searches the dark matter axion [60–63]. A microwave cavity is installed into the haloscope to enhance the detection efficiency of microwaves converted from the dark matter axions with a mass of the microwave region. ADMX experiment [63] utilized an axion haloscope and excluded KSVZ axions in a mass range of 3.3 μeV$< m_A <$3.69 μeV.

1.2.3 Laboratorial experiments

Laboratorial experiments searching for ALPs utilizes artificial photon sources. These experiments are roughly classified into two types: measurement of photon-photon interaction and photon-regeneration experiments. The latter will be explained in detail since it has many properties to do with this thesis,.

Although the most stringent limits on ALPs in a broad mass range has been obtained by astronomical observations, their limits inevitably depend on models of stellar evolution and cosmological systems. Telescope experiments are less model-dependent because ALPs are directly detected. However, these experiments have also uncertainties on production of ALPs. Upper limits obtained by these experiments can be relaxed by possible reduction effects. ALPs flux from stellar systems can be reduced when ALPs mass and couplings depend on environmental parameters in stellar systems, such as temperature and matter densities [78]. For example, a model can be considered in which the $a\mathcal{F}\mathcal{F}$-type interaction in the vacuum becomes an $a\phi\mathcal{F}\mathcal{F}$-type interaction in an environment with temperature of $T >\sim$ keV, where ϕ is an additional scalar field with a mass of ~ 30 keV [79]. The model can reduce strongly the production rate of stellar ALPs.

The uncertainty of solar axion searches is considered to be much smaller than other searches since the solar activity is better understood by Standard Solar Model (SSM). However, there are some anomalous solar activities such as the solar coronal heating. Moreover, solar axions can be detected only when they can actually escape from the sun. The ALPs mean free path within the sun can be expressed to be $\sim \left(\frac{g_{a\gamma\gamma}}{10^{-10}\mathrm{GeV}^{-1}}\right)^{-2} 8 \times 10^{13} R_\odot$, where $R_\odot$ is the solar radius [75]. Solar axions can be absorbed by the sun itself and may evade the detection of these helioscope experiments with the sensitivity of $g_{a\gamma\gamma} > 1 \times 10^{-9}$ GeV^{-1} when the coupling constant is larger than $\sim 5 \times 10^{-3}$ GeV^{-1}. Although the coupling is so strong that it contradicts with SSM [80], the coupling range has not yet been experimentally excluded in a broad mass range.

Laboratorial experiments have importance as totally model-independent searches. These experiments can complement for more model-dependent searches, astronomical observation and telescope experiments.

Photon-photon interaction

Although photons cannot interact with each other in the framework of the classical electrodynamics, quantum-electrodynamics (QED) predicts that photon-photon interaction can be mediated by a fourth-order Feynman diagram with a virtual electron-positron loop (the box diagram) [81–83] as shown in Fig. 1.3 (a). The interaction may be also mediated by ALPs as shown in Fig. 1.3 (b). ALPs can be searched indirectly by measuring possible enhancement of the interaction cross section. For example, the photon-photon interaction causes vacuum magnetic birefringence (VMB), an anisotropy of vacuum refractive index under an external magnetic field. VMB has been searched by experiments such as BMV [84] and PVLAS [72].

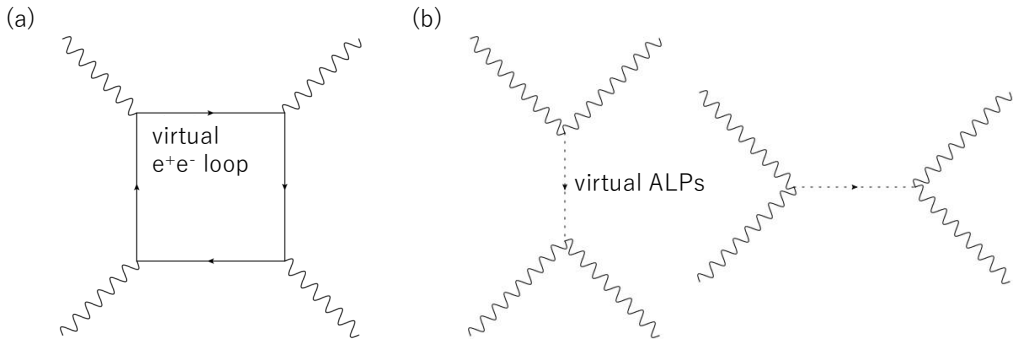

Figure 1.3: Feynman diagrams of photon-photon interaction. (a): The first order Feynman diagram of photon-photon interaction in QED (the box diagram). (b) Photon-photon interaction mediated by ALPs.

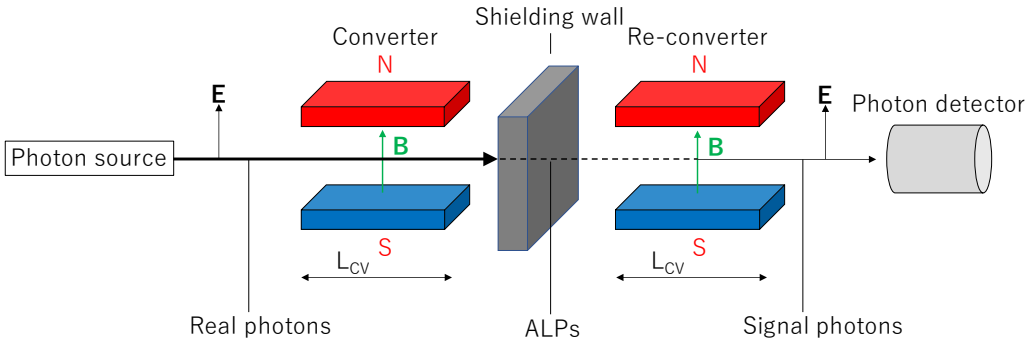

Figure 1.4: Schematics of a LSW experiment.

One of the most stringent laboratorial limit on ALPs is obtained by the PVLAS experiment.

Photon regeneration experiments

Photon-regeneration experiments measure photons passing through a photon-shielding wall under external magnetic fields as shown in Fig. 1.4. Injected photons from artificial sources are converted into ALPs by the Primakoff effect in an external magnetic field parallel to the polarization of photons. These ALPs pass through an opaque wall without absorption due to weak couplings to matters. Then ALPs are subsequently reconverted into detectable photons by an inverse process. The experimental scheme are referred to as Light-Shining-through-a-Wall (LSW) [85]. The telescope experiment shown above is equivalent to a LSW experiment with celestial sources of ALPs.

The conversion in an external magnetic field can be described as an oscillation between photons and ALPs similar to neutrino oscillation. The conversion and

re-conversion probability can be calculated by the following formula,

$$P_{a\leftrightarrow\gamma} = \left(\frac{g_{a\gamma\gamma}}{2}\right)^2 \frac{k_\gamma}{k_a} \left| \int_0^{L_{\rm CV}} B(z) e^{iqz} dz \right|^2 , \tag{1.12}$$

where $k_{\gamma,a}$ are the wavenumber of photons and ALPs, $B(z)$ is a magnetic field strength and $L_{\rm CV}$ is the conversion length (the longitudinal length of the magnetic field). The momentum transfer of the conversion, $q = k_a - k_\gamma$, can be approximated as

$$q = \frac{m_\gamma^2 - m_a^2}{2k_\gamma}, \tag{1.13}$$

where $m_\gamma \simeq 28.9 \text{ eV}\sqrt{\frac{Z}{A}(\rho/\text{g}\cdot\text{cm}^{-3})}$ is the plasma frequency of the media on the photon path, Z is the atomic number, A is the mass number and ρ is the density of the media. The conversion probability can be simplified when the magnetic field is uniform, $B(z) = B_0$, and $k_\gamma \simeq k_a$,

$$P_{\gamma\leftrightarrow a} \simeq \left(\frac{1}{2} g_{a\gamma\gamma} B_0 L_{\rm CV}\right)^2 \left| \frac{\sin\frac{qL_{\rm CV}}{2}}{\frac{qL_{\rm CV}}{2}} \right|^2 . \tag{1.14}$$

The conversion is resonant when the momentum transfer satisfies $\frac{qL_{\rm CV}}{2} < 1$. The resonant condition is equivalent to a resonant mass of ALPs as follows,

$$\left| m_a^2 - m_\gamma^2 \right| < \frac{4k_\gamma}{L_{\rm CV}}, \tag{1.15}$$

where the bandwidth is defined as the half maximum of $(P_{\gamma\leftrightarrow a})^2$. The resonant ALPs' mass is roughly proportional to $\sqrt{k_\gamma}$. The experimental sensitivity to heavier ALPs deteriorates due to the oscillating factor of Eq. (1.14).

The expected value of detectable photons reconverted from ALPs can be evaluated as follows,

$$N_{\rm obs} = N_\gamma (P_{\gamma\leftrightarrow a})^2 \epsilon_{\rm d}, \tag{1.16}$$

where N_γ is a photon flux and $\epsilon_{\rm d}$ is the detection efficiency of reconverted photons. The dependency of the sensitivity to $g_{a\gamma\gamma}$ is summarized in Tab. 1.1 for later convenience.

Many LSW experiments with optical lasers have been performed by BFRT [86, 87], BMV [88, 89], GammaV [90], LIPSS [91, 92], ALPS [70, 93] and OSQAR [71, 94] collaborations. The most stringent limits among these experiments are obtained by OSQAR and ALPS experiments. The resonant ALPs' masses of these experiments are ~ 1 meV.

High-energy LSW experiments have been also performed by using X-ray sources and a neutrino beam line to enhance the sensitivity to heavier ALPs. LSW experiments using X-ray synchrotron radiation facilities have been proposed [95, 96] and performed at ESRF [97] and SPring-8 [98]. These experiments utilized hard X rays

Table 1.1: The dependency of the sensitivity to $g_{a\gamma\gamma}$ when the LSW scheme is used.

parameter	$g_{a\gamma\gamma}$ dependency (exponent)
intensity of conversion fields	-1
conversion length	-1
photon flux	$-\frac{1}{4}$
detection efficiency	$-\frac{1}{4}$
background rate	$+\frac{1}{8}$
DAQ time	$-\frac{1}{4}$ (0 BG) or $-\frac{1}{8}$

with a photon energy of $\mathcal{O}(10)$ keV and searched ALPs with a mass of $m_a \sim 1$ eV. The highest-energy LSW experiment has been performed by the NOMAD [69] experiment. This experiment searched the heaviest ALPs with $m_a < 40$ eV by using photons with an energy of ~ 40 GeV from the CERN SPS neutrino target.

Table 1.2 summarizes the major LSW experiments, ALPS, X-ray LSW experiments at ESRF/SPring-8 and NOMAD experiment.

Table 1.2: The summary of major previous LSW searches for ALPs. ω is the photon energy, N_γ is the effective photon flux, B is the magnitude of magnetic fields and L is the length of the magnetic fields. The NOMAD experiment is performed by injecting 1.1×10^{19} protons to a target of the neutrino beam line.

Experiment	ω	N_γ [photon/s]	B [T]	L [m]	m_a (resonant)
ALPS [70]	2.3 eV	3.2×10^{21}	5	4.2	<1 meV
ESRF [97]	50.2/90.7 keV	$1.2 \times 10^{12}/3.1 \times 10^{10}$	3	0.15	<1 eV
SPring-8 [98]	9.5 keV	3×10^{13}	9	0.4	<0.1 eV
NOMAD [69]	~ 40 GeV	$\star$	2	7	<40 eV

1.3 Searches using atomic electric fields

The photon-ALP conversion can take place also under an electric field such as an atomic electric field within a crystal. It is well known that atomic electric fields in crystals are as high as $\sim 10^{11}$ V/m, which correspond to magnetic fields of $\sim 10^3$ T. The effective magnetic fields are much higher than currently available magnets. These high electric fields can provide an additional conversion scheme for LSW experiments.

The feasibility to use the electric field has been explored by Ref. [99, 100]. Figures 1.5 show the ALP-photon conversion schemes theoretically considered. The conversion of nearly massless ALPs under Bragg-case reflection is firstly studied

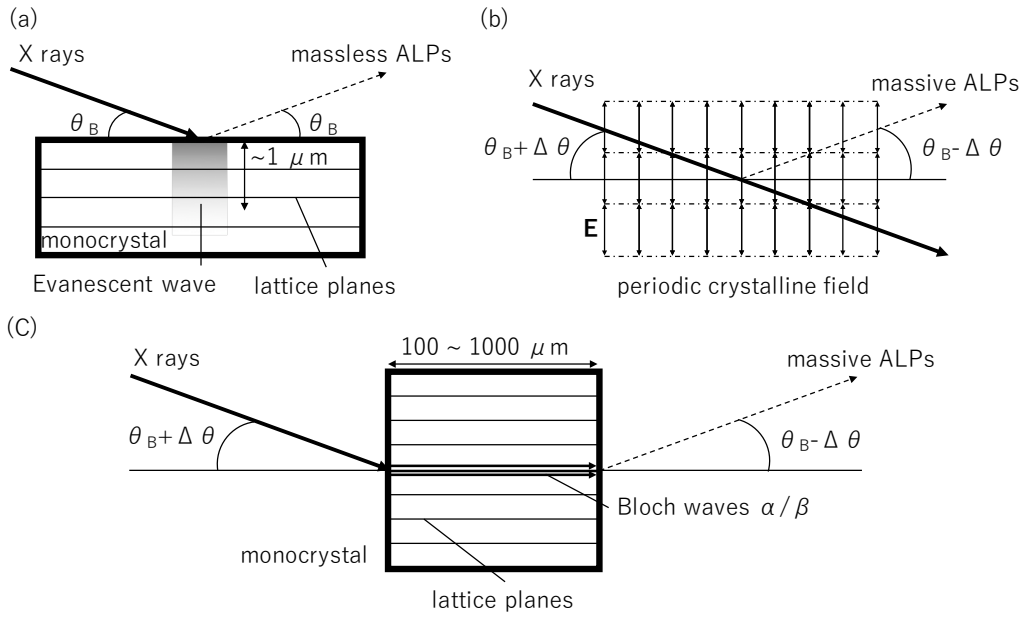

Figure 1.5: Schematics of X ray-ALP conversion schemes using atomic electric fields. These figures are cited from Ref. [1]. (a) The Bragg-case conversion of nearly-massless ALPs under the Bragg angle [99]. (b) The conversion of massive ALPs by a periodic electric field without X-ray diffraction and scattering [100]. (c) The Laue-case conversion utilized in this thesis. [1]

by *Buchmuüller and Hoogeveen* [99]. Incident X rays with a photon energy of $\mathcal{O}(10)$ keV fall on a crystal with reflecting planes parallel to its surface (Bragg-case) under the Bragg angle, $\theta_{\rm B}$, as shown in Fig. 1.5 (a). These injected X rays can be coherently converted into ALPs since the X-ray wavelength is the same order as the periodic length of the atomic electric field. The conversion process is studied in the framework of the Darwin dynamical theory of X-ray diffraction. The conversion probability can be calculated as follows [99],

$$P_{a\leftrightarrow\gamma} = \left(\frac{1}{2} g_{a\gamma\gamma} E_T L_{\rm B} \cos\theta_{\rm B}\right)^2, \tag{1.17}$$

where E_T is an effective electric field in the crystal and $L_{\rm B} \sim 1$ μm is an X-ray penetration length under the Bragg condition. The equation is quite analogous to that of the Primakoff effect under a magnetic field, Eq. (1.14).

Solar axion can be searched by using the conversion scheme since the energy scale of the coherent conversion is the same as that of solar axions [101, 102]. Solar axion searches of this kind have been performed by making use of a germanium [65–67] and a NaI [68] detector itself as an ALP-X ray converter. These detectors convert solar axions and detect converted photons by themselves as shown in Fig. 1.6. The X-ray detector is sensitive to solar axions which satisfy the Bragg

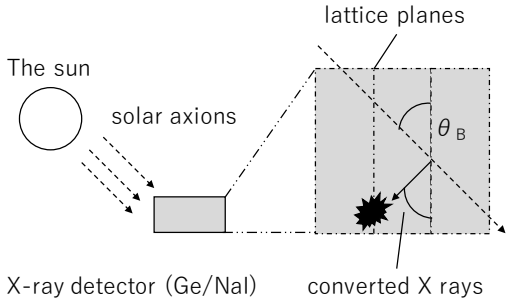

Figure 1.6: Schematics of a solar axion search using an atomic electric field.

condition, $2d\sin\theta_T^A = \lambda_A$, where θ_T^A is the injection angle of axions and λ_A is the axion wavelength. Solar axions with a broad range of energy can be searched by a long-time measurement since the angle, θ_T^A, changes temporally due to the rotation and the revolution of the earth. Solar axion searches of this kind constrain axions with a mass of $m_A < \mathcal{O}(1)$ keV and the 90% C. L. upper limit of $g_{A\gamma\gamma} < 1.7 \times 10^{-9}$ GeV^{-1} [68].

However, a photon-regeneration experiments using atomic electric field had not yet been performed. It is because the Bragg-case X-ray diffraction reduces the X-ray penetration length and the production efficiency of ALPs. Reference [99] suggested that Laue-case conversion, in which lattice planes are perpendicular to the crystal surface, may have a longer X-ray penetration length and higher conversion probability. Laue-case X-ray diffraction enhances the X-ray penetration length and the conversion probability by causing X-ray standing waves within a crystal referred to as the Bloch waves α and β.

The effect of nonzero ALPs' mass is taken into account by *Liao* later [100]. This study showed that massive ALPs can be converted only when the X-ray injection angle is away from the Bragg angle. The resonant ALPs' mass can reach up to $m_a \sim 10$ keV by detuning the X-ray injection angle. The conversion scheme can enhance the sensitivity to heavier ALPs than previous LSW experiments.

This study approximates crystals as a periodic electric field as shown in Fig.1.5 (b) and ignores X-ray absorption, scattering and diffraction in a realistic crystal. A rigorous calculation including these effects is required to conduct a new-type LSW experiment. *Yamaji* studies the Laue-case conversion within a crystal as shown in Fig. 1.5 (c) by taking into account X-ray diffraction and the relation between ALPs' mass and the detuning angle at the same time [1].

1.4 Structure of this thesis

The first LSW experiment using the Laue-case conversion will be proposed and performed in this thesis based on the calculation. The experiment searches sub-keV ALPs ($m_a < 1$ keV) theoretically and astronomically motivated as shown in

Sec. 1.1.4.

The new LSW scheme using the Laue-case conversion will be proposed in the second chapter. The detailed experimental setup will be explained in the third chapter. The experimental result will be shown in the fourth chapter. The discussion about the result and future experiments will be shown in the fifth chapter. And then I will conclude the thesis in the sixth chapter. The theoretical background for the Laue-case conversion will be described in detail in Appendix A.

Chapter 2

Laue-case conversion

This chapter proposes a new scheme for the LSW experiment using the Laue-case conversion within a single crystal. The detailed theoretical backgrounds for the chapter are explained in Appendix A.

2.1 Interaction between crystals and X rays

Crystals are solids whose constituents are arranged in a periodic structure referred to as the crystal lattice. The crystal lattice can be divided into unit cells as shown in Figs. 2.1, whose physical dimensions are referred to as the lattice constant ($d_{1\sim3}$ for three dimensional axis $a_{1\sim3}$). Figure 2.1 (a) shows the homogeneous lattice unit cell of diamond-like crystals with the lattice constant of $d_{1\sim3} = d_0$. The diamond-like crystals such as C(diamond), Si and Ge are frequently used in X-ray optics. It can be assumed that all atoms in crystals are arranged on lattice planes as shown in Fig 2.1 (b). These planes are defined as planes whose $a_{1\sim3}$-interceptions are $\frac{nd_1}{h}$, $\frac{nd_2}{k}$, $\frac{nd_3}{l}$, respectively, where (hkl) are lattice indexes and n is an integer. The (hkl) lattice planes of diamond-like crystals has a spacing of $d_{hkl} = \frac{d_0}{\sqrt{h^2+k^2+l^2}}$.

The lattice constants (~ 1 $\mathring{A}$) are generally the same order as the wavelength of X rays. The reflection or transmission probability of X rays injected into a crystal have an anomalous structure (a peak or a dip) around the angle referred to as the Bragg angle, θ_{B}. The phenomenon is referred to as X-ray diffraction. Figure 2.2 (a) shows schematics of X-ray diffraction. Injected X rays are scattered by atomic electrons on lattice planes. The scattering amplitudes from lattice planes can interfere constructively with each other when the X-ray injection angle, θ_T^γ, and the angle of scattered X rays, θ_S^γ, coincide with the Bragg angle as follows,

$$2d_{hkl}\sin\theta_{\mathrm{B}} = \lambda_\gamma, \tag{2.1}$$

where λ_γ is the X-ray wavelength. The condition is equivalent to the one that the X-ray path difference between X rays scattered by adjacent lattice planes is equal to the X-ray wavelength.

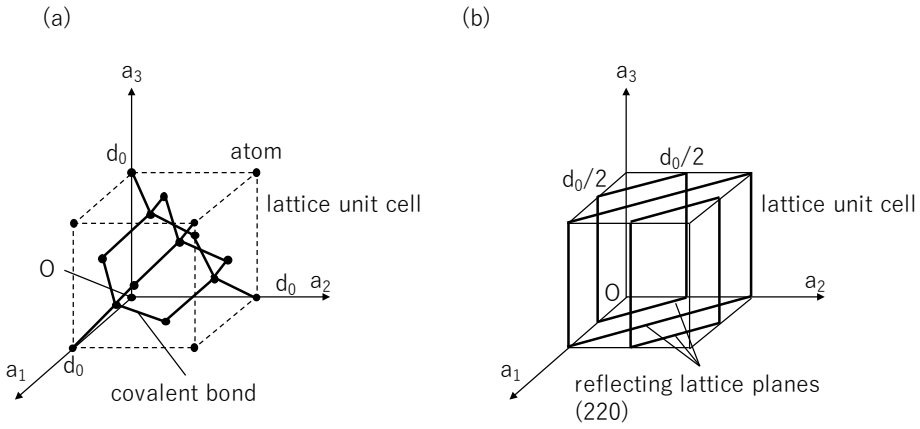

Figure 2.1: Schematics of an unit cell and lattice planes of a crystal lattice. (a): an unit cell of diamond-like crystals. (b) (220) lattice planes of diamond-like crystals.

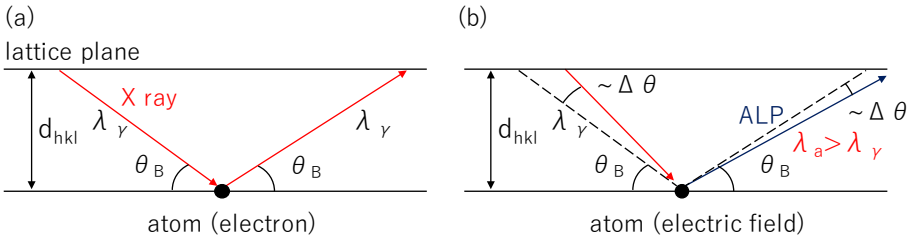

Figure 2.2: Schematics of the interaction between crystals and X rays. Left: X-ray diffraction. Right: conversion from X rays into ALPs.

The conversion between X rays and ALPs within a crystal is analogous to X-ray diffraction. The schematics of the conversion is also shown by Fig. 2.2 (b). Injected X rays can be converted into massive ALPs by atomic electric fields close to lattice planes. The resonant X-ray injection angle for the conversion becomes larger than the Bragg angle, $\theta_T^\gamma = \theta_\mathrm{B} + \Delta\theta$, since the wavelength of generated ALPs, λ_a, is larger than λ_γ due to ALPs' mass. The detuning angle, $\Delta\theta$, depends on the ALPs' mass, m_a. The angle of converted ALPs, θ_S^a, becomes smaller than the Bragg angle, $\theta_S^a = \theta_\mathrm{B} - \Delta\theta$, due to the Fresnel diffraction condition. The detailed explanation for the $\Delta\theta$ dependence of the resonant mass and the conversion probability will be given in the following section.

2.2 Laue-case conversion in a single crystal

Figures 2.3 show schematics of the Laue-case conversion between X rays and ALPs. The left figure shows the Laue-case conversion from X rays into ALPs. The injected

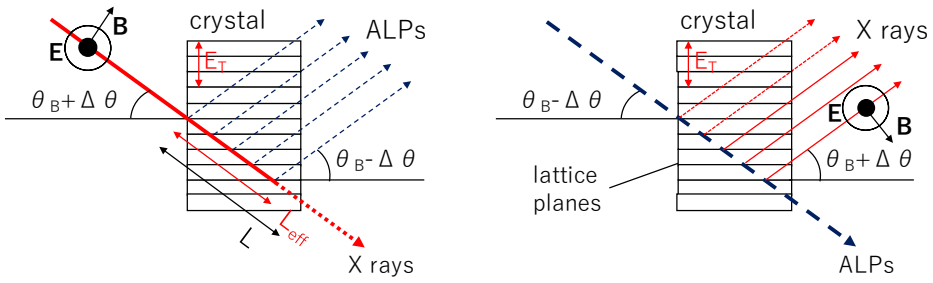

Figure 2.3: Schematics of the Laue-case conversion between X rays and ALPs. Left: the conversion from X rays into ALPs. Right: the re-conversion from ALPs into X rays.

X rays are coherently converted into ALPs by the high electric fields, E_T, perpendicular to the lattice planes of a single crystal. The lattice planes are perpendicular to surfaces of the crystal in this case. The injected X rays are required to be σ-polarized since the conversion takes place only when E_T is parallel to the magnetic fields of X rays.

The following two cases are explained below: the conversion under the Bragg condition and the one when the injection angle is away from the Bragg angle.

Under the Bragg condition

The conversion under the Bragg condition has two contributions from X-ray standing waves, the Bloch waves α/β. These standing waves originate from the composition of transmitted and reflected X rays under the Bragg condition. One of the important effects caused by the Bloch waves is the anomalous X-ray transparency of crystals referred to as the Borrmann effect [103, 104]. The attenuation lengths of the Bloch waves, $L_{\mathrm{att},\alpha/\beta}$, are different from those of normal X rays as follows,

$$L_{\mathrm{att},\alpha/\beta} = \frac{L_{\mathrm{att}}}{1 \mp \kappa}, \tag{2.2}$$

where L_{att} is the normal X-ray attenuation length and κ is a parameter close to unity defined by Eq. (A.57). The attenuation length of the Bloch wave α is much longer than normal X rays.

The conversion probability has two maxima corresponding to the Bloch waves under the following condition,

$$\left| m_a^2 - (m_\gamma^2 \mp \Delta m_\gamma^2) \right| \lesssim \frac{4k_\gamma}{L} \tag{2.3}$$

where m_γ is the plasma frequency of the crystal, Δm_γ is its modification due to X-ray diffraction and L is the X-ray path length within the crystal. The resonant condition is quite analogous to previous LSW experiments, except that the plasma frequencies are $m_\gamma \mp \Delta m_\gamma \sim \mathcal{O}(10)$ eV.

When the resonant condition is exactly satisfied, the conversion probability has the peak value of

$$\begin{aligned} P_{a\leftrightarrow\gamma} &= \left(\frac{1}{4}g_{a\gamma\gamma}E_T L_{\mathrm{eff},\alpha/\beta}\cos\theta_{\mathrm{B}}\right)^2 \\ &= 8.6\times10^{-8}\times\left(\frac{g_{a\gamma\gamma}}{10^{-3}\ \mathrm{GeV}^{-1}}\frac{E_T}{10^{11}\ \mathrm{V/m}}\frac{L_{\alpha/\beta}\cos\theta_{\mathrm{B}}}{1\ \mathrm{mm}}\right)^2 \qquad (2.4) \\ L_{\alpha/\beta} &\equiv 2L_{\mathrm{att},\alpha/\beta}\left(1-\exp\left(-\frac{L}{2L_{\mathrm{att},\alpha/\beta}}\right)\right), \qquad (2.5) \end{aligned}$$

where $L_{\alpha/\beta}$ are the effective conversion lengths of the Bloch waves. The effective conversion length is reduced from the X-ray path length within the crystal due to X-ray absorption. Although the expression is quite analogous to that of Bragg-case conversion, Eq. (1.17), the conversion length, $L_{\alpha/\beta}\sim L_{\mathrm{att}}\sim\mathcal{O}(100)$ μm, is much longer than that of Bragg-case conversion, $L_{\mathrm{B}}\sim\mathcal{O}(1)$ μm. The conversion length of the Bloch wave α can be enhanced further by the Bormann effect in particular.

The mass dependence of conversion probability is numerically calculated as shown in Fig. 2.4. It is assumed in this calculation that injected X rays have a photon energy of 17 keV and that the converter is a 600 μm-thick Si(220) crystal. The ALPs-two photon coupling constant is assumed to be an arbitral value of $g_{a\gamma\gamma}=10^{-3}$ GeV^{-1}, which is a typical upper limit obtained by X-ray LSW experiments. The calculated conversion probability (the red line) is compared with the result of simplified approximation (the blue line) in Ref. [100]. The probability has two maxima around m_γ, which correspond to contributions from the Bloch waves α ($\sqrt{m_\gamma^2-\Delta m_\gamma^2}=19.6$ eV) and β ($\sqrt{m_\gamma^2+\Delta m_\gamma^2}=39.4$ eV). There widths determined by Eq. (2.3) are 1.1 eV and 0.56 eV, respectively. There is an oscillation structure around the two main peaks due to the X-ray standing waves. The contribution from the Bloch waves destructively interfere with each other at the plasma frequency, $m_a=m_\gamma=31$ eV.

The calculation is far different from that of simplified calculation without X-ray diffraction and absorption. The effect of X-ray diffraction divides the single peak at $m_a=m_\gamma$ in Ref. [100] into two peaks corresponding to the Bloch waves, and the height of peaks are reduced by the division of standing waves and the effect of X-ray absorption.

Away from the Bragg angle

X rays behave normally within crystals when the X-ray injection angle is away from the Bragg angle and the effect of X-ray diffraction is negligible. The resonant condition of ALPs' mass depends on $\Delta\theta$ as follows,

$$\left|m_a^2-m_\gamma^2-2q_T\left(k_\gamma\sin\theta_T^\gamma-\frac{q_T}{2}\right)\right|\lesssim\frac{4k_\gamma}{L}, \qquad (2.6)$$

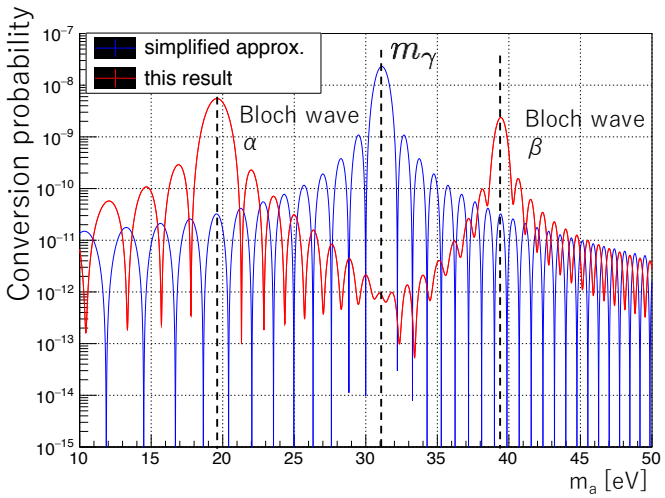

Figure 2.4: The mass dependence of the conversion probability under the Bragg condition. It is assumed in this figure that a 600 μm-thick Si(220) crystal and X rays with a photon energy of 17 keV are used.

where $q_T = \frac{2\pi}{d_{hkl}}$ is the reciprocal lattice spacing and $\theta_T^\gamma = \theta_B + \Delta\theta$ is the X-ray injection angle. Although the equation is also analogous to Eq. (1.15), the resonant mass increases by the factor of $2q_T\left(k_\gamma \sin\theta_T^\gamma - \frac{q_T}{2}\right)$. The factor within the parenthesis is equivalent to the deviation from the Bragg condition $\left(k_\gamma \sin\theta_T^\gamma = \frac{q_T}{2}\right)$. Fig. 2.5 (a) shows the $\Delta\theta$ dependence of the resonant mass under the same condition as Fig. 2.4. The resonant mass in this condition can have large values as much as $m_a = 1$ keV at $\Delta\theta = 4.6$ mrad, and $m_a = 10$ keV at $\Delta\theta = 510$ mrad. Figure 2.6 shows the $\Delta\theta$ dependence close to the Bragg angle ($|\Delta\theta| < 4$ μrad). The Bloch waves coexist in this region as shown above and have resonant ALP's mass different from each other. Since the contribution of the Bloch waves vanishes when $|\Delta\theta| >\sim 3$ μrad, ALPs with a mass close to the plasma frequency, $m_\gamma \sim 31$ eV, cannot be resonantly converted no matter what angles.

When the resonant condition is exactly satisfied, the conversion probability have the peak value as follows,

$$\begin{aligned} P_{a\leftrightarrow\gamma} &= \left(\frac{1}{2} g_{a\gamma\gamma} E_T L_{\rm eff} D\cos\theta_{\rm T}\right)^2 \\ &= 3.5\times10^{-7}\times(D\cos\theta_{\rm T})^2\times\left(\frac{g_{a\gamma\gamma}}{10^{-3}\ {\rm GeV}^{-1}}\frac{E_T}{10^{11}\ {\rm V/m}}\frac{L_{\rm eff}}{1\ {\rm mm}}\right), \quad (2.7) \\ L_{\rm eff} &\equiv 2L_{\rm att}\left(1-\exp\left(-\frac{L_T}{2L_{\rm att}}\right)\right), \quad (2.8) \end{aligned}$$

where $L_{\rm eff}$ is an effective conversion length and $D < 1$ is a factor representing the effect of the detuning defined by Eq. (A.53). The conversion probability is enhanced

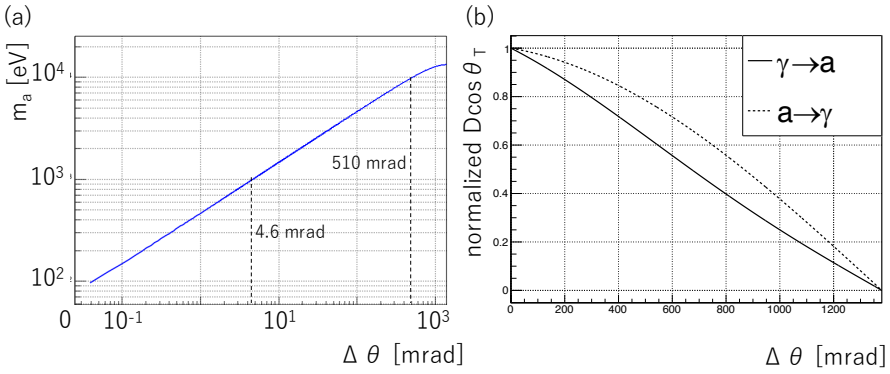

Figure 2.5: The $\Delta\theta$ dependence of resonant ALPs' mass and relative sensitivity to $g_{a\gamma\gamma}$. (a): the resonant mass. The same condition as Fig. 2.4 is assumed. The upper limit of $\Delta\theta$ corresponds to $\theta_T^\gamma = 90$ deg. (b) the factor, $D\cos\theta_{\rm T}$, normalized by its maximum value of $\cos\theta_{\rm T}$ ($\Delta\theta = 0$). The normalized value corresponds to the relative sensitivity to $g_{a\gamma\gamma}$.

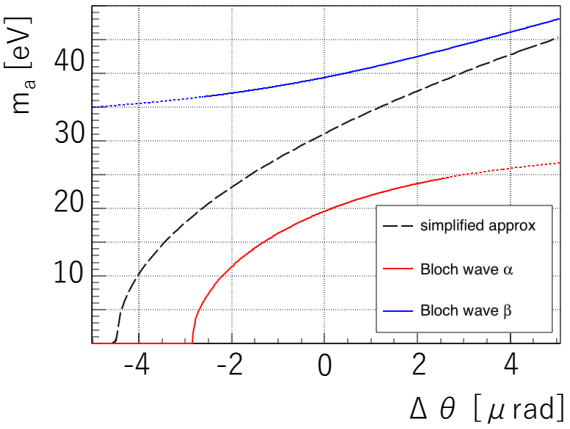

Figure 2.6: The $\Delta\theta$ dependence of resonant ALPs' mass close to the Bragg angle. The red and blue solid lines show the resonant ALP's mass corresponding to the Bloch waves α/β. The dotted lines show the region where the amplitudes of the Bloch waves are reduced. The dashed line shows the resonant mass obtained by neglecting X-ray diffraction [100].

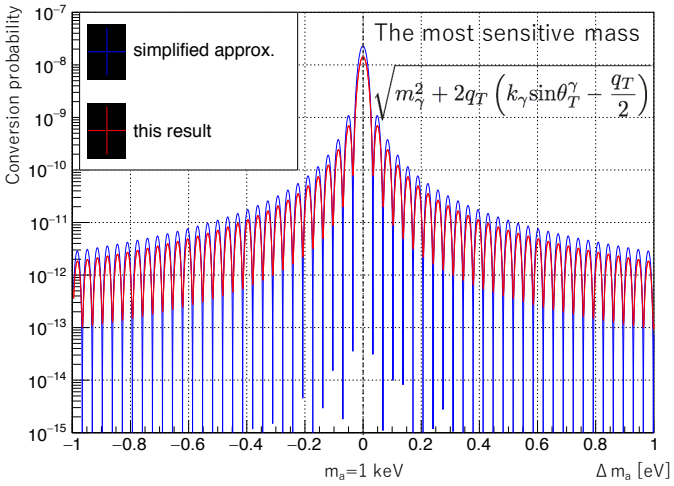

Figure 2.7: The mass dependence of conversion probability far away from the Bragg condition. (the red line). The same condition as Fig. 2.7 is considered in this figure, except that the detuning angle is $\Delta\theta = 4.6$ mrad. The result of the simplified approximation [100] is also shown by the blue line. The horizontal axis represents the deviation of m_a from the resonant mass of 1 keV.

from that of Bragg-case conversion since the effective conversion length is also much longer than that of Bragg case one. The factor, $D\cos\theta_{\rm T}$, is a monotonically decreasing function of $\Delta\theta$ as shown in Fig. 2.5 (b). The factors for the conversion and re-conversion normalized by their maxima ($\cos\theta_T^\gamma$ at $\Delta\theta = 0$) are shown by the solid and dotted lines. The $\Delta\theta$ dependence of the factor is equivalent to the relative experimental sensitivity to $g_{a\gamma\gamma}$. The normalized factor is ~ 1 for sub-keV ALPs, ~ 0.7 for $m_a = 10$ keV and vanishes when $\theta_T^\gamma = 90$ deg.

The mass dependence of the conversion probability is also numerically calculated as shown by the red line in Fig. 2.7. The same condition as Fig. 2.4 is considered in this figure except that the X-ray injection angle is detuned by $\Delta\theta = 4.6$ mrad. The result of the simplified approximation [100] is also shown by the blue line. On the contrary to the case under the Bragg condition, the conversion probability has a narrow peak around the resonant mass of 1 keV. The peak has the width (22 meV) determined by Eq. (2.6) and sub peaks around it. The peak probability is reduced by the simplified calculation due to X-ray absorption in the crystal.

The effective conversion lengths, $L_{\alpha/\beta}$ and $L_{\rm eff}$, are much longer ($\mathcal{O}(10^{2\sim3})$) than the X-ray penetration length of Bragg-case conversion under the Bragg condition. It can be said that the Laue-case conversion is suitable to convert and reconvert ALPs in a LSW experiment since the conversion probability of the Laue-case conversion is also $10^{2\sim3}$ higher than the Bragg-case one.

2.3 Suitable crystals for the Laue-case conversion

The conversion probability depends on the following properties of the crystal: the effective electric field, E_T, the X-ray attenuation length, $L_{\rm att}$, and the ratio, κ. These parameters depend strongly on the kinds of crystals. The candidate for the crystals are diamond-like crystals frequently used in X-ray optics such as C(diamond), Si and Ge crystals.

The (220) lattice planes have the most intense electric fields among lattice planes of diamond-like crystals. The parameters of C(220), Si(220) and Ge(220) crystals for X rays with a photon energy of 17 keV are summarized in Tab. 2.1. The diamond crystals have the most ideal specs among them with strong electric fields, long attenuation lengths and κ close to unity. The runner-up candidates are Si crystals. Ge crystals are disfavored due to its short attenuation lengths.

The diamond crystals have a major disadvantage that large diamond single crystals cannot be easily manufactured. A silicon crystal is used to convert between X rays and ALPs in this thesis. Although silicon crystals are less sensitive to $g_{a\gamma\gamma}$ (in particular, for $m_a \sim 10$ keV due to the D factor), they are suitable to a proof-of-concept experiment since silicon crystals with a geometry of $\mathcal{O}(1 \sim 10)$ cm are currently available. The large crystals can be used to make a channel-cut crystal as shown in the next section.

Table 2.1: The parameters of C(220), Si(220) and Ge(220) lattice planes for X rays wth a photon energy of 17 keV.

lattice planes	q_T [keV]	$\theta_{\rm B}$ [deg]	E_T [V/m]	$L_{\rm att}$	κ
C(220)	9.85	16.8	6.8×10^{10}	7.7 mm	0.981
Si(220)	6.46	10.9	4.4×10^{10}	650 μm	0.969
Ge(220)	6.20	10.5	7.3×10^{10}	27 μm	0.965

2.4 LSW experiment using the Laue-case conversion

The schematics of an experiment using the Laue-case conversion is shown by Fig. 2.8. This setup is similar to those of prior LSW experiments except that Primakoff effect takes place under atomic electric fields. Incident X rays fall on the converter crystal with lattice planes perpendicular to the crystal surface. These injected X rays are converted into ALPs whose mass satisfies the resonant condition, Eq. (2.6). The converted ALPs pass through a shielding wall blocking unconverted X rays. These ALPs are subsequently reconverted into detectable X rays by the re-converter crystal. The ALPs' mass can be continuously searched by scanning the detuning angle, $\Delta\theta$.

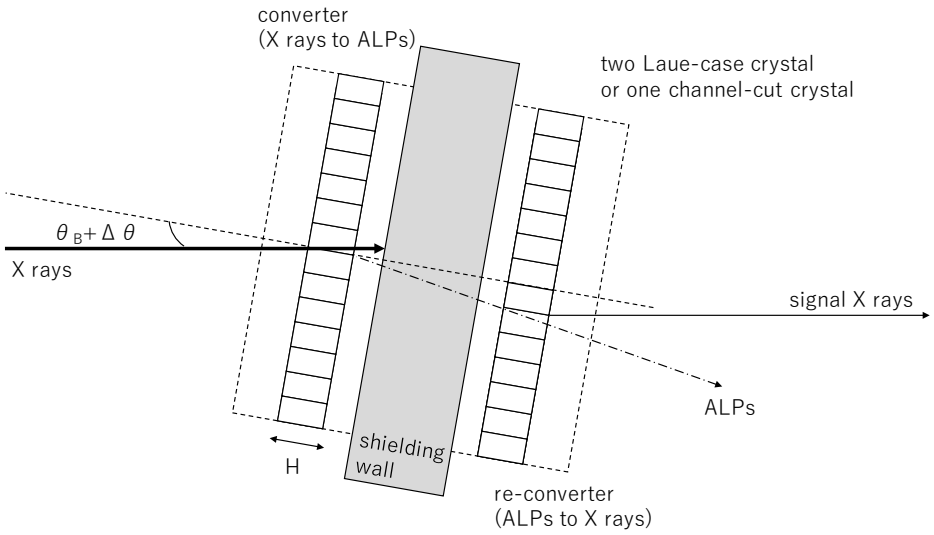

Figure 2.8: Schematics of an experimental setup using the Laue-case conversion. This figure is cited from Ref. [1]

Requirement for the LSW experiment

The conversion scheme requires as a matter of course that the resonant ALPs' mass of the conversion coincides with that of the re-conversion. Their resonant masses deviate from each other if the lattice planes of the re-converter is not exactly parallel to that of the converter. The parallelism between them is required to perform the photon-regeneration experiment efficiently. The required angular precision can be deduced from Eq. (2.6) as follows,

$$\Delta\theta_{\mathrm{CV}} = \frac{2d_{hkl}}{\pi H}, \tag{2.9}$$

where H is the thickness of the crystal and the width corresponds to the full width at a half maximum of $P_{\gamma\to a}P_{a\to\gamma}$. The required angular precision is $\Delta\theta_{\mathrm{CV}} = \mathcal{O}(100\ \mathrm{nrad})$ since d_{hkl} and H are the order of $\mathcal{O}(1\ \mathring{A})$ and $\mathcal{O}(1\ \mathrm{mm})$, respectively. It is recommended to use a channel-cut crystal with two blades manufactured on a single crystal in order to guarantee the required precision. ALPs converted by the one blade can be resonantly reconverted into X rays by the other blade since lattice planes within these blades are exactly parallel to each other.

Experimental sensitivity

The expectation number of signal X rays detected by the LSW experiment can be described as follows when the parallelism between the converter and the re-

converter is guaranteed,

$$N_{obs} = N_\gamma T_{\rm DAQ} \frac{\Delta\theta_{\rm CV}}{\Delta\theta_{\rm BL}} \epsilon_d \epsilon_S P_{\gamma\to a} P_{a\to\gamma}, \tag{2.10}$$

where N_γ is the intensity of injected X rays, $T_{\rm DAQ}$ is the DAQ time, $\Delta\theta_{\rm BL}$ is the effective angular divergence of injected X rays, ϵ_d is the X-ray detection efficiency and ϵ_S is a reduction factor of the conversion probability shown in the next section. The sensitivity to $g_{a\gamma\gamma}$ (90% C.L.) can be simplified when backgrounds do not exist as follows,

$$g_{a\gamma\gamma} > 2\times10^{-4} \left(\frac{N_\gamma}{10^{13}\ {\rm Hz}} \frac{T_{\rm DAQ}}{10^3\ {\rm s}} \frac{\Delta\theta_{\rm CV}}{\Delta\theta_{\rm BL}} \epsilon_d\epsilon_S\right)^{-\frac{1}{4}} \times \left(\frac{E_T}{10^{11}\ {\rm V/m}} \frac{L_{\rm eff}}{1\ {\rm mm}} D\cos\theta_T\right)^{-1}. \tag{2.11}$$

The experimental sensitivity to $g_{a\gamma\gamma}$ has the dependence summarized in Tab. 2.2. The dependence is almost similar to that of prior LSW experiments shown in Tab. 1.1, except that the dependence on the conversion length is modified due to the dependence of $\Delta\theta_{\rm CV}$.

The resonant ALP's mass will be scanned up to 1 keV with the sensitivity of $g_{a\gamma\gamma} \sim 5\times10^{-3}$ GeV^{-1} in this thesis, which is the same order as previous X-ray LSW experiments and corresponds to the coupling scale evading the detection of helioscope experiments. The factor, D, can be reduced to unity in this mass range. The DAQ time for a certain detuning angle is inversely proportional to the square of the scanning mass range since the resonant mass, m_a, is proportional to $\sqrt{\Delta\theta}$. The sensitivity to $g_{a\gamma\gamma}$ is inversely proportional to the square root of the upper limit on the scanning mass range from Eq. (2.11). If the scanning mass range is expanded to $m_a = 10$ keV, the sensitivity to $g_{a\gamma\gamma}$ is reduced by a factor of 5.

Table 2.2: The dependence of the sensitivity to $g_{a\gamma\gamma}$ in the experimental setup using the Laue-case conversion.

parameter	symbol	$g_{a\gamma\gamma}$ dependency (exponent)
intensity of conversion fields	E_T	-1
conversion length	$L_{\rm eff}$	$-\frac{3}{4}$
photon flux	N_γ	$-\frac{1}{4}$
effective angular divergence	$\Delta\theta_{\rm BL}$	$\frac{1}{4}$
detection efficiency	ϵ_d	$-\frac{1}{4}$
reduction factor of the conversion	ϵ_S	$-\frac{1}{4}$
background rate	$N_{\rm BG}$	$+\frac{1}{8}$
DAQ time	$T_{\rm DAQ}$	$-\frac{1}{4}$ (0 BG) or $-\frac{1}{8}$

2.5 Possible shift of the Bragg angle

The experimental sensitivity shown by Eq. (2.11) can be reduced even if the parallelism between the converter and the re-converter is exactly guaranteed. The Bragg angles of the converter and the re-converter can deviate from an ideal value. The shift of the Bragg angle, $\Delta\theta_{\rm B}$, is also required to be less than $\Delta\theta_{\rm CV}$ since the shift changes the resonant mass. The shift originates from the following effects: the fluctuation of lattice constant, X-ray refraction at the crystal surfaces and thermal deposit at the converter.

Fluctuation of lattice constant

The lattice constant of single crystals fluctuates slightly around its mean value. The fluctuation can be observed as Moiré stripes in X-ray interferometry [105], and it is estimated to be $\frac{\Delta d}{d} \sim 10^{-8}$. The fluctuation shifts the Bragg angle as follows,

$$\Delta\theta_{\rm Bd} = \frac{\Delta d}{d}\tan\theta_{\rm B} \simeq \mathcal{O}(1\ \text{nrad}). \tag{2.12}$$

The Laue-case conversion can occur only when $\Delta\theta_{\rm Bd} < \Delta\theta_{\rm CV}$. The condition imposes an upper limit on the effective conversion length, $L_{\rm eff}$.

X-ray refraction at the crystal surfaces

The refractive index of X rays in crystals can be represented as $n = 1 - \delta$, where δ is $\mathcal{O}(10^{-6})$. X rays are refracted on the crystal surfaces when X rays fall on the crystal diagonally. The crystal surfaces are not perfectly perpendicular to the lattice planes in a realistic experimental setup. The refraction on surfaces produces the following shift of the Bragg angle,

$$\Delta\theta_{\rm BR} = \delta\Delta\theta_{\rm S}, \tag{2.13}$$

where $\Delta\theta_{\rm S}$ is the angular precision of the crystal surfaces. The shift is up to $\mathcal{O}(1$ nrad) since the value of $\Delta\theta_{\rm S}$ is typically much less than 1 mrad for silicon crystals used in X-ray optics.

Thermal deposit at the converter crystal

Injected X rays are absorbed only by the converter in the experimental setup shown above. The thermal deposit, ΔW, warms the injection point on the converter by ΔT. The temperature rise expands the crystal lattices on the point and changes the Bragg angles. The shift can be roughly estimated as follows,

$$\Delta\theta_{\rm BT} \sim -\alpha_l \Delta T \tan\theta_{\rm B}, \tag{2.14}$$

where α_l is the linear thermal expansion coefficient of the crystal. The condition $\Delta\theta_{\rm BT} < \Delta\theta_{\rm CV}$ imposes an upper limit on the intensity of injected X rays.

The thermal deposit changes the Bragg angle most significantly among the contribution shown above. The shift of the Bragg angle reduces the efficiency of the conversion and reconversion, $P_{\gamma\to a}P_{a\to\gamma}$. The reduction factor due to the shift, ϵ_S, will be evaluated by simulation in this thesis.

2.6 Specific motivation for the Laue-case conversion

The Laue-case conversion within a crystal can provide an alternative scheme of LSW searches for ALPs. This experimental scheme is sensitive to heavier ALPs than previous LSW experiments. Previous LSW experiments using an external magnetic field have resonant ALP's mass limited to $\sim m_\gamma$ (up to 40 eV) due to the resonant condition, Eq. (1.15). The conversion probability of previous experiments fluctuates as a function of m_a when the resonant condition is not satisfied. The sensitivity of previous experiments to ALPs heavier than their resonant masses are not only strongly reduced, but also unreliable. The new experimental scheme can search sub-keV ALPs effectively in contrast to previous LSW experiments. ALPs with a sub-keV mass are theoretically and astronomically motivated as shown in Sec. 1.1.4.

Although the parameter region has been excluded by the observation of stellar evolution and telescope experiments, this region has not ever been searched model-independently. There are some ways to evade the detection of ALPs in these celestial searches as shown in Sec. 1.2.3. The new conversion scheme is scientifically important in that it can complement the results of these model-dependent searches.

There is another advantage of the new conversion scheme: the tunability of the resonant ALPs' mass. The resonant mass of previous LSW experiments cannot be easily tuned because it depends on the photon energy, the conversion length and the plasma frequency of the media on the photon path. By contrast, the Laue-case conversion has resonant ALPs' mass dependent on the detuning angle. The resonant mass can be easily scanned only by rotating the conversion system.

Chapter 3

Setup and devices

This chapter describes a setup of the experiment performed at an X-ray facility, SPring-8. The whole experimental setup including beamline optics is briefly described firstly. It is followed by more detailed explanation for beamline optics, a conversion-reconversion system and an X-ray detector.

3.1 X-ray source: SPring-8 BL19LXU

An intense X-ray source is also required to perform the new-type LSW experiment because the sensitivity to $g_{a\gamma\gamma}$ is proportional to a $\frac{1}{4}$ power of an X-ray flux. BL19LXU beam line of SPring-8 is one of the most suitable X-ray sources for the experiment [106]. SPring-8 (Fig. 3.1) is a third-generation synchrotron radiation facility optimized to generate intense X-ray beams. BL19LXU beam line is the most strong beam line among all beam lines of SPring-8. The X-ray flux of BL19LXU is 2.5×10^{13} Hz at an X-ray photon energy of 17 keV. The experiment is performed during a beam time between 2017/10/01 10:00 and 2017/10/05 10:00 (96 hours).

Figure 3.1: The aerial picture of SPring-8. This picture is cited from http://www.spring8.or.jp/. The position of BL19LXU beam line is also indicated.

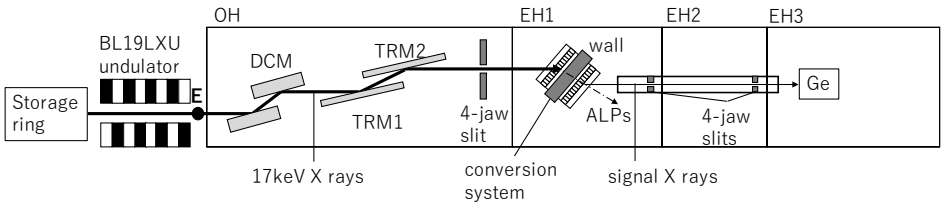

Figure 3.2: Schematics of the whole experimental setup.

3.2 Whole experimental setup

Figure 3.2 shows the schematics of the whole experimental setup. The storage ring of SPring-8 accelerates and stores electron beams with an electron energy of 8 GeV. The electrons are injected into a 25-m undulator of BL19LXU beam line, and then radiate horizontally-polarized X-ray synchrotron radiation with a photon energy of $\omega_1 = 17$ keV (fundamental waves). The energy is selected because its attenuation length within a conversion crystal accords with the crystal thickness. The time structure of X rays depends on the bunch modes of the storage ring.

The X-ray beams are monochromatized by a double crystal monochromator (DCM) within an optical hatch (OH) of BL19LXU. The monochromatized X rays contain higher harmonics with a photon energy of $n\omega_1$, where n is an integer larger than unity. These higher harmonics are eliminated by two total reflection mirrors (TRM1 and TRM2) located at the downstream of DCM to enhance the S/N ratio of the experiment. Stray X rays from DCM and TRMs are cut by a four-jaw slit within OH.

The X-ray beams are subsequently injected to a conversion-reconversion system located at an experimental hutch (EH) 1. The system is composed of two blades on a silicon channel-cut crystal with lattice planes perpendicular to its surfaces (Laue-case). An atomic electric field within the first blade converts X rays into ALPs. Unconverted X rays are blocked by a shielding wall between blades. ALPs passing through the wall are reconverted into detectable X rays by the second blade. A germanium detector located at EH3 measures signal X rays with a photon energy of 17 keV. The resonant mass of ALPs is scanned by varying the X-ray injection angle to the blades.

The X-ray path are evacuated except around the conversion system and the detector (The path length in the air is $\sim$ 80 cm). Materials on the X-ray path, such as atmospheric molecules, X-ray vacuum windows and the conversion system itself, scatter X rays and generate stray X rays. These stray X rays are also cut by two four-jaw slits located at the downstream of the crystal (EH1 and EH2). Table 3.1 summarizes the optical parameters of the setup.

parameter	value
electron beam energy	8 GeV
electron bunch interval (F mode)	342.1 ns
electron current	100 mA (80.8+1.6×12)
electron bunch duration	342.1 ns/40 ps
X-ray polarization	horizontal
X-ray energy	17 keV
X-ray intensity	2.5×10^{13} Hz
X-ray bandwidth after DCM	2.1 eV (full width)
X-ray beam width	0.8×1.2 mm^2 (full width)

Table 3.1: Summary of optical parameters.

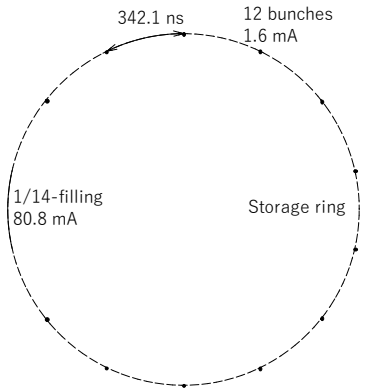

Figure 3.3: Schematics of the F-mode bunch structure.

3.3 Beamline optics

3.3.1 Bunch mode of the storage ring

The bunch mode of the storage ring determines the timing structure of X-ray synchrotron radiation. The bunch mode during the beam time is F mode (1/14-filling + 12 bunches). Figure 3.3 shows the bunch structure of F mode. F mode has thirteen electron bunches equally spaced within the storage ring. The longest and strongest electron bunch fills one fourteenth of the storage ring and has an electron current of 80.8 mA. Other twelve bunches have an electron current of 1.6 mA. The timing structure of X rays is so fine that the X-ray detector cannot distinguish individual X-ray pulses. The X-ray beams are effectively regarded as continuous waves in this thesis.

Beam dumps take place at 10/03 17:43∼20:43 and 10/04 09:53∼12:34 during the beam time. The total intensity of electron beams is reduced to 70 mA after the second beam dump.

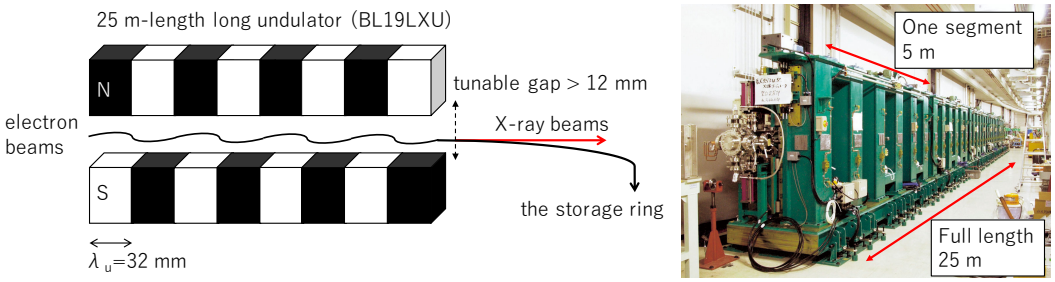

Figure 3.4: The undulator of BL19LXU. Left: schematics of the undulator. Right: a picture of the undulator cited from Ref. [107]. The undulator is composed of five in-vacuum undulators with a length of 5 m.

3.3.2 Undulator

BL19LXU has the longest undulator in SPring-8 as shown in Fig. 3.4. The magnetic period of the undulator is λ_u =32 mm and the length of the undulator is 25 m (780 periods). The periodic magnetic fields within the undulator fluctuate an electron trajectory, and then electron beams radiate horizontally-polarized X-ray synchrotron radiation.

The properties of synchrotron radiation depend on the following two parameters: the Lorentz factor of electrons, $\gamma = \frac{E}{m_e}$ ($\gamma = \frac{8\ \mathrm{GeV}}{511\ \mathrm{keV}} \sim 1.6 \times 10^4$ for SPring-8) and K factor. K is represented as follows,

$$K = \frac{eB_0\lambda_u}{2\pi m_e} = 0.934\lambda_u[\mathrm{cm}]B_0[\mathrm{T}], \tag{3.1}$$

where B_0 is a magnitude of magnetic fields within the undulator, e is the elementary electric charge and m_e is the electron mass. The wavelength of fundamental waves can be calculated to be

$$\lambda_1 = \frac{\lambda_u}{2\gamma^2}\left(1 + \frac{K^2}{2}\right). \tag{3.2}$$

The K factor of BL19LXU can be continuously tuned by varying the gap length of magnets. The energy range of fundamental waves is between 7.4 and 18.8 keV. The energy is set to be 17 keV in this experiment. The undulator also radiates higher harmonics with a photon energy of $n\omega_1$, where n is an integer larger than unity.

3.3.3 Double-crystal monochromator (DCM)

BL19LXU has a double-crystal monochromator (DCM) [108,109] within its OH as shown in Fig. 3.5. DCM is composed of two Si(111) crystals with lattice planes parallel to their surfaces (Bragg-case). The first crystal reflects injected X rays vertically when the X-ray injection angle satisfies the Bragg condition. The reflected X rays are also reflected by the second crystal to preserve the horizontality of the

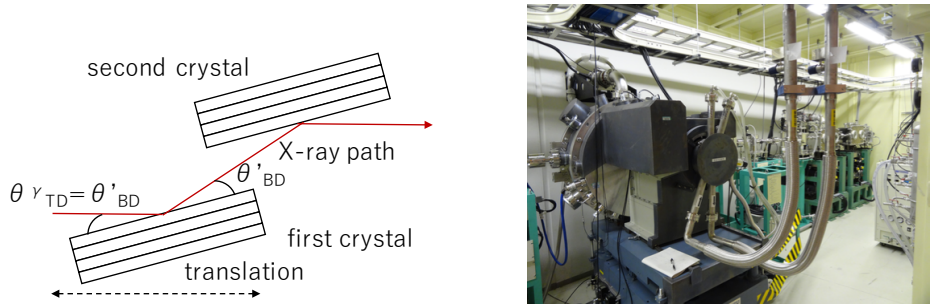

Figure 3.5: The double-crystal monochromator (DCM). Left: schematics of DCM. Right: a picture of DCM.

X-ray path. The reflection angle, $\theta'_{\rm BD}$, is determined by the Bragg condition with refraction,

$$2d_{111}\sin\theta'_{\rm BD}\left(1-\frac{1-n}{\sin^2\theta_{\rm BD}}\right)=\lambda_\gamma, \tag{3.3}$$

where $d_{111}=3.1$ [$\mathring{A}$] is the lattice spacing of Si(111), $\theta_{\rm BD}$ is the Bragg angle without refraction, λ_γ is the wavelength of X rays and n is the refractive index of the crystal as follows,

$$n\equiv 1-\delta=1-\frac{\rho r_e\lambda_\gamma^2}{2\pi}, \tag{3.4}$$

where ρ is the electron density of the crystal and r_e is the classical electron radius. The reduction factor, δ, is an order of 10^{-6}. The Bragg angle of DCM is $\theta'_{\rm BD}\simeq\theta_{\rm BD}=6.68$ deg for X rays with a photon energy of 17 keV.

The injection angle dependence of the reflection efficiency can be calculated by using the dynamical theory of X-ray diffraction as shown by Fig. 3.6. The reflection efficiency has a narrow peak with the full width of $\Delta\theta_{\rm FW}\sim 14.5$ μrad. The acceptable angular divergence is equivalent to the acceptable bandwidth of the reflection as follows,

$$\frac{\Delta E_{\rm FW}}{E}=\Delta\theta_{\rm FW}\cot\theta'_{\rm BD}. \tag{3.5}$$

The acceptable bandwidth is $\Delta E_{\rm FW}=2.1$ eV for Si(111) lattice planes and X rays with a photon energy of 17 keV.

The crystals are aligned by three automatic stages adjusting the elevation angles of crystals and the horizontal position of the first crystal along the X-ray path. The horizontal position is tuned for X rays to fall on the center of the second crystal. The crystals are cooled by using liquid nitrogen to prevent thermal expansion of the crystals due to the X-ray heat load on the injection point (~ 400 W/mm^2).

3.3.4 Total reflection mirror system (TRM)

Higher harmonics from the undulator are also reflected by DCM since they satisfy the Bragg condition of Si(n,n,n) lattice planes except the forbidden reflection of

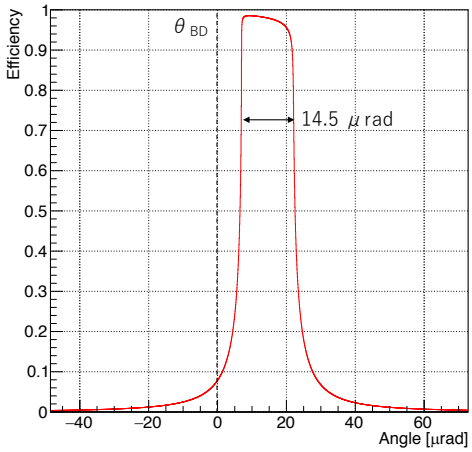

Figure 3.6: The injection angle dependence of the reflection efficiency for a Si(111) crystal (Bragg-case) and X rays with a photon energy of 17 keV. The horizontal axis shows the difference between an X-ray injection angle, $\theta^{\gamma}_{\mathrm{TD}}$, and the Bragg angle without refraction, θ_{BD}.

Si(222). The strongest and the most problematic higher harmonics among them is the third one. The third harmonics of BL19LXU after DCM is about three orders of magnitude weaker than that of fundamental waves when the photon energy of fundamental waves is $\omega_1 = 17$ keV. These higher harmonics are not easily absorbed by materials including an X-ray shielding wall. When these higher harmonics are injected into the conversion system, they can possibly reach an X-ray detector by directly penetrating through the wall or going around behind the wall via multiple X-ray scattering of materials within EH1. It is required to block the higher harmonics within the beamline optics in order to enhance the S/N ratio of the experiment.

A total reflection mirror system as shown in Fig. 3.7 is installed into the downstream of DCM to exclude higher harmonics. The total reflection mirror system is composed of two silicon crystals (TRM1 and TRM2) coated with a 100 nm-thick platinum layer. When X rays fall on materials with an injection angle less than a critical angle, X rays can be totally reflected. The critical angle, α_c, can be calculated from Eq. (3.4) as follows,

$$\alpha_c = \sqrt{2\delta} = \lambda_\gamma \sqrt{\frac{\rho r_e}{\pi}}. \tag{3.6}$$

TRMs can exclude higher harmonics with smaller critical angles by tuning the X-ray injection angle. The second mirror is installed to preserve the horizontality of the X-ray path and to exclude higher harmonics more strongly.

The critical angle of TRMs is $\alpha_c = 0.5$ deg for 17 keV X rays. The injection

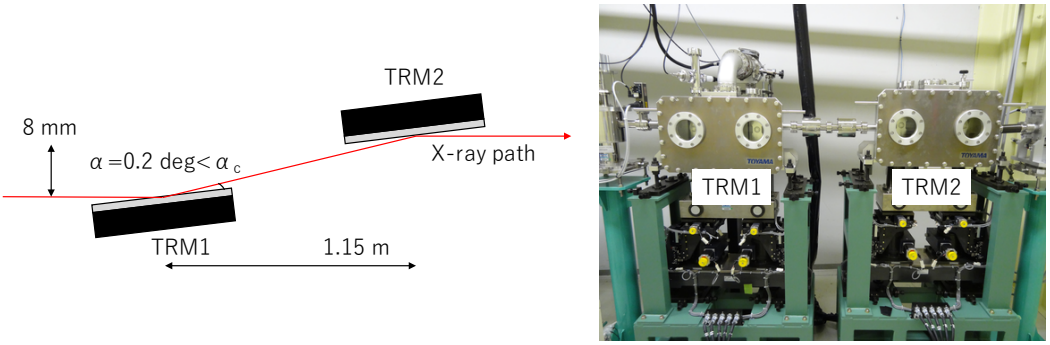

Figure 3.7: Total reflection mirror system installed into the downstream of DCM. Left: schematics of TRMs. Right: a picture of TRMs.

angle is set to 0.2 deg in this experiment. The reflection probability of TRMs with the injection angle is 80% and $\sim 10^{-2.5}$ for the fundamental wave and the third harmonics, respectively. The total reflection raises the beam height by 8 mm.

3.3.5 Four-jaw slit in OH

A four-jaw slit located at the most downstream position of OH is used to block stray X rays scattered by beamline optics such as DCM and TRMs. The slit is composed of four 1 mm-thick tantalum blades as shown in Fig. 3.8. The opening window of the slit is set to be 2(H) × 2(V) mm^2 in this experiment.

The profile of X-ray beams is measured by scanning the vertical and horizontal position of the opening window with a step length of 0.1 mm and measuring the intensity of transmitted beams. The beam intensity is measured by using a PIN photodiode as will be shown. The measured beam profiles are shown in Fig. 3.9. The vertical profile is distorted due to a speckle from TRMs. The vertical and horizontal widths of X-ray beams are 0.8 mm and 1.2 mm (full width), respectively.

3.4 Conversion-reconversion system

A conversion-reconversion system is installed into EH1 of BL19LXU as shown in Fig. 3.10. The system is covered with a vinyl sheet to reduce temperature change and drift of a goniometer angle.

3.4.1 Channel-cut crystal

Injected X rays are converted and reconverted by a Si(220) channel-cut crystal with lattice planes parallel to the crystal surfaces (Laue-case) as shown in Fig. 3.11. The channel-cut crystal has two 600 μm-thick blades manufactured on a single silicon crystal with a spacing of 25 mm. The first blade (converter) converts injected X rays into ALPs with a resonant mass, and the second blade (re-converter) reconvert

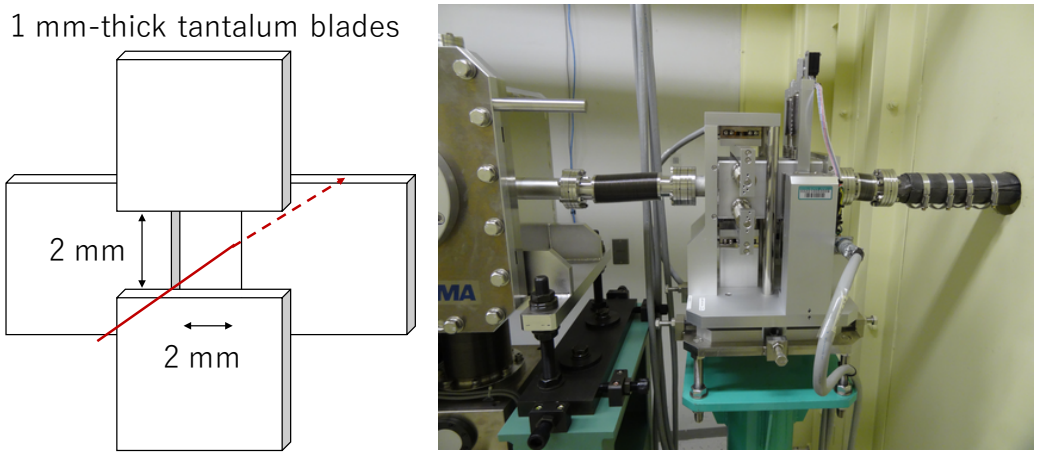

Figure 3.8: The four-jaw slit located at the most downstream position of OH. Left: schematics of the four-jaw slit. Right: a picture of the slit.

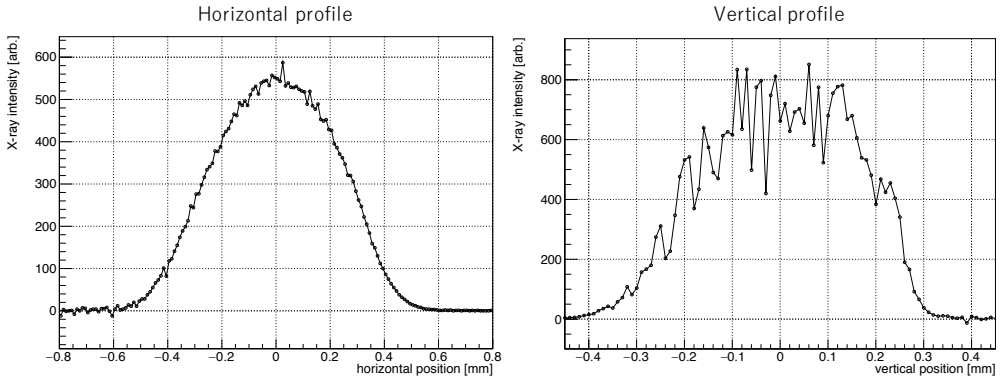

Figure 3.9: The profile of X-ray beam measured by the four-jaw slit within OH. Left: the horizontal profile. Right: the vertical profile.

these ALPs into detectable X rays. The converted ALPs can automatically satisfy the re-conversion condition of the second blade due to the parallelism between lattice planes within the blades, namely the perfectness of the silicon single crystal. The perfectness of silicon single crystals has been well established by X-ray interferometry [105]. The conversion takes place in the vertical direction ($\sigma-$polarization), and the X-ray beam height is lowered by 9.5 mm.

The crystal is originally developed for an X-ray photon-photon scattering experiment [110]. The X-ray energy is tuned to 17 keV because its attenuation length accords with the blade thickness in this experiment. The Bragg angle is $\theta_{\rm B}$ =10.95 deg, and the effective conversion length is $L_{\rm eff}$ = 488 μm for 17 keV X rays. The detuning angle from the Bragg angle, $\Delta\theta$, is scanned from 0 to 4.6 mrad. The detuning angle corresponds to the resonant ALPs' mass of $m_a < 1$ keV. The

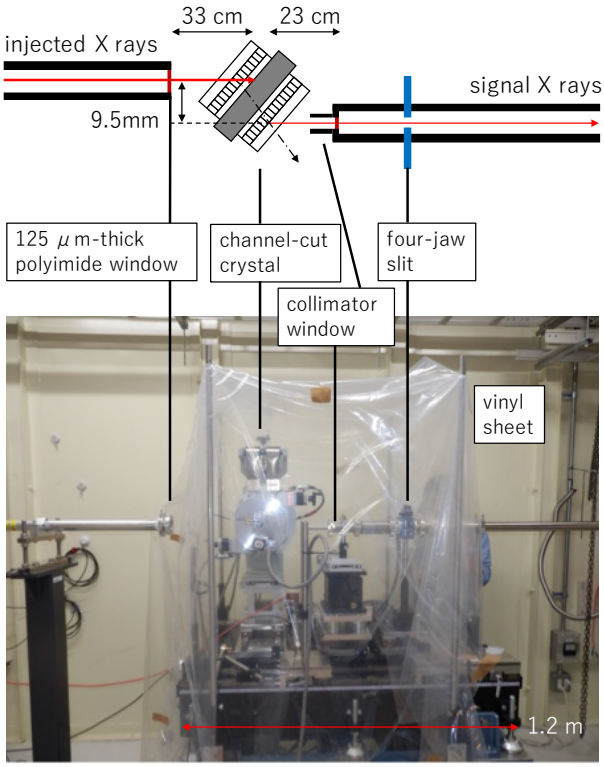

Figure 3.10: The conversion-reconversion system. The system is installed into EH1 of BL19LXU. Upper: schematics of the system. Lower: a picture of the system.

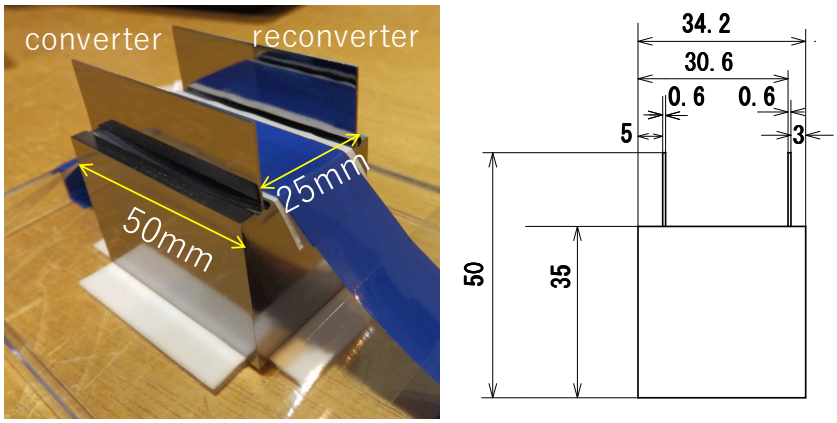

Figure 3.11: The Si(220) channel-cut crystal used in this experiment. Left: a picture of the crystal. Right: a detailed geometry of the crystal.

properties of the crystal are summarized in Table 3.2.

Table 3.2: Properties of the channel-cut crystal for X rays with a photon energy of 17 keV.

parameter	symbol	value
lattice index	(hkl)	(220)
lattice constant	d_{hkl}	1.92 Å
reciprocal lattice spacing	q_T	6.46 keV
the Bragg angle	θ_{B}	10.95 deg
effective electric field	E_T	4.4×10^{10} V/m
X-ray attenuation length	L_{att}	650 μm
effective conversion length	L_{eff}	488 μm
required parallelism	$\Delta\theta_{\mathrm{CV}}$	204 nrad
plasma frequency	m_γ	31 eV

3.4.2 Goniometer and rotating stage

The channel-cut crystal is angularly aligned by using a precision motorized goniometer RA20-21. The goniometer has a θ motorized stage with an angular resolution of 0.87 μrad (half step). The θ stage is connected to a stepping motor via gears. The angular resolution can be enhanced by dividing a step angle of a stepping motor. The step is divided by ten (an angular resolution of 0.087 μrad) in this experiment. The channel-cut crystal is connected to the θ stage via a rotation coupler MSTS-25-10×12 and a rotating stage as shown in Fig. 3.12. The channel-cut crystal is fixed to the rotating stage by using caul plates and pushing screws not to distort the crystal lattice. The signal X rays are collimated by a 5 mm-thick stainless steel plate with a 5 mm-diameter hole.

The angular alignment of the rotating stage can slip from the position of the stepping motor (specified by the number of pulses) when the rotating stage itself or an X-ray shielding wall are moved by stages as follows:

1. When an X-ray shielding wall is closed and opened by a motorized X stage, the angle of the rotating stage changes by $\sim$ 30 pulses=5.2 μrad due to the movement of the wall and the heat production of the motorized X stage.

2. When the goniometer angle is scanned fast by 27000 pulses=4.7 mrad, the angle of the rotating stage shifts temporally by 10 pulses=1.7 μrad due to the distortion of the rotation coupler. The temporal shift lasts about 30 minutes.

3. During the drive of the θ stage, the angle of the rotating stage shifts temporally by 20 pulses=3.5 μrad in the direction of the driving. It is considered to be also attributed to the distortion of the rotation coupler.

The angular alignment can also drift slowly due to the change of the room temperature. The drift will be measured and taken into account as a systematic uncertainty.

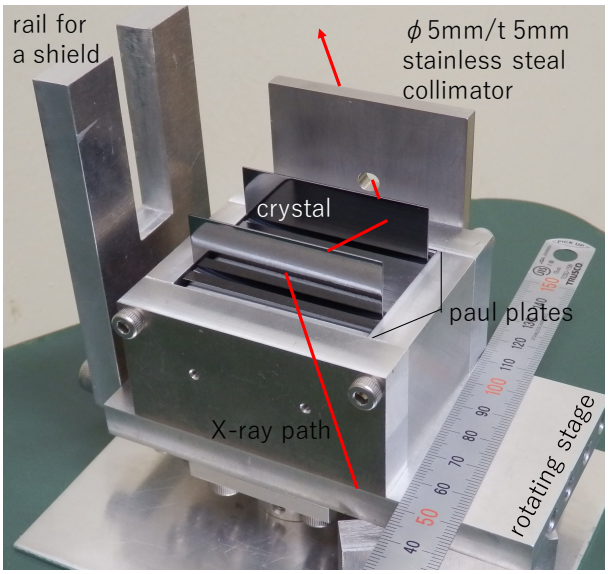

Figure 3.12: The rotating stage.

3.4.3 Shielding wall

A 15 mm-thick shielding wall made of stainless steel is installed between the converter and the re-converter in order to block unconverted X rays as shown in Fig. 3.13. The shielding wall is mounted on a motorized X stage XA05A-R with a stroke of 15 mm fixed to the rotating stage. The closest gap between the wall and the crystal is 200 μm. The position of the wall is mechanically aligned by using knock pin holes on the rotating stage and the wall. A PIN photodiode is installed into the shielding wall to measure the intensity of injected X rays and to evaluate the goniometer angle. The X-ray window is an aluminum plate with the thickness of 302.7 ± 1.6 μm. The property of the photodiode will be explained in Sec. 3.7.

3.4.4 Four-jaw slits between the system and an X-ray detector

Some of injected X rays are scattered by materials on the X-ray path such as the converter, an X-ray window and atmospheric molecules. The scattered X rays can come around behind the shielding wall by being scattered by other materials. An X-ray detector is installed into EH3 to reduce backgrounds due to the stray X rays. Two four-jaw slits are also installed into an evacuated pipe between the channel-cut crystal and an X-ray detector as shown in Fig. 3.14. The slits are composed of four 1 mm-thick tantalum blades similar to the slit within OH shown in Sec. 3.3.5.

The conversion-reconversion system expands the beam width of signal X rays vertically as shown in Fig. 3.15. When the crystal thickness is thin compared to the attenuation length, injected beams mainly pass along the direction of the injected beams (O-Tm), and converted beams are expanded within the triangle area

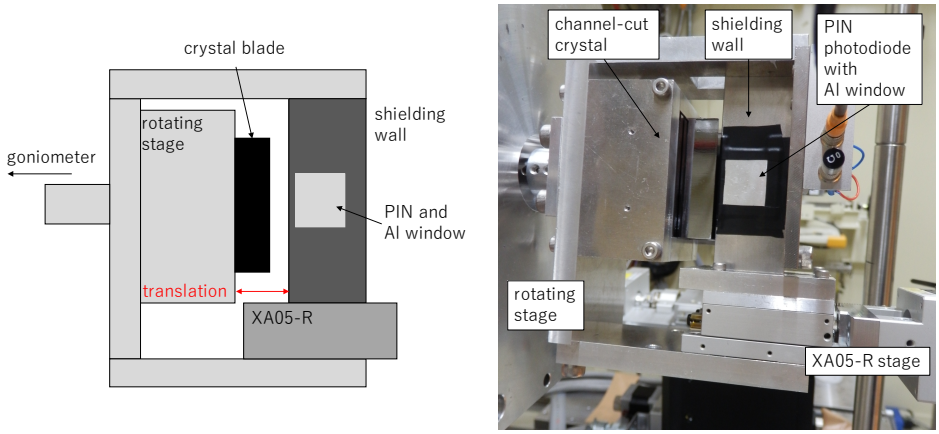

Figure 3.13: The X-ray shielding wall. Left: schematics viewed from the upstream of the channel-cut crystal. Right: a picture.

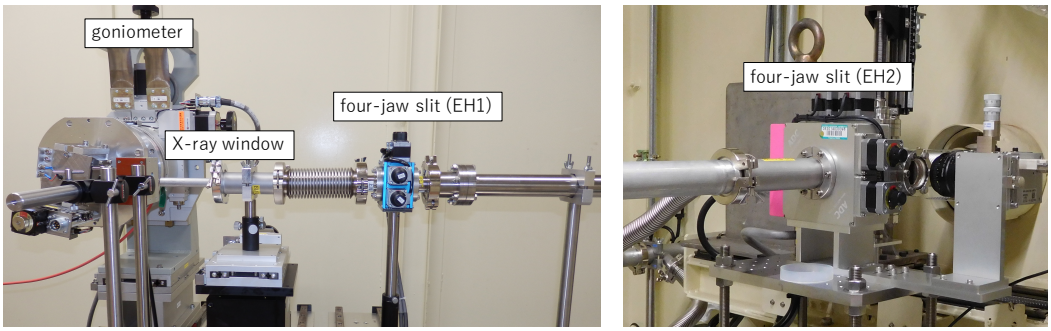

Figure 3.14: The four-jaw slit within the downstream optics. Left: the four-jaw slit (SLT-100-10) installed into the downstream of the channel-cut crystal. Right: the four-jaw slit (SLT-100-P) located at EH2.

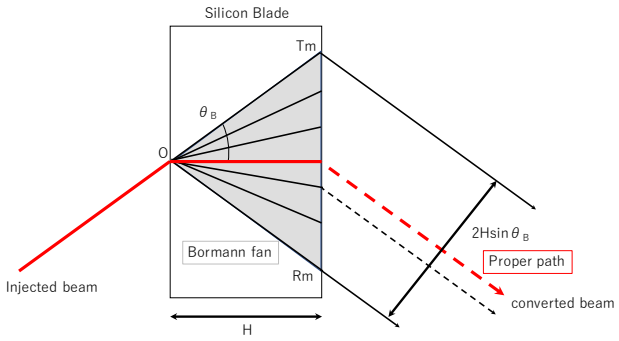

Figure 3.15: Schematics of the Bormann fan.

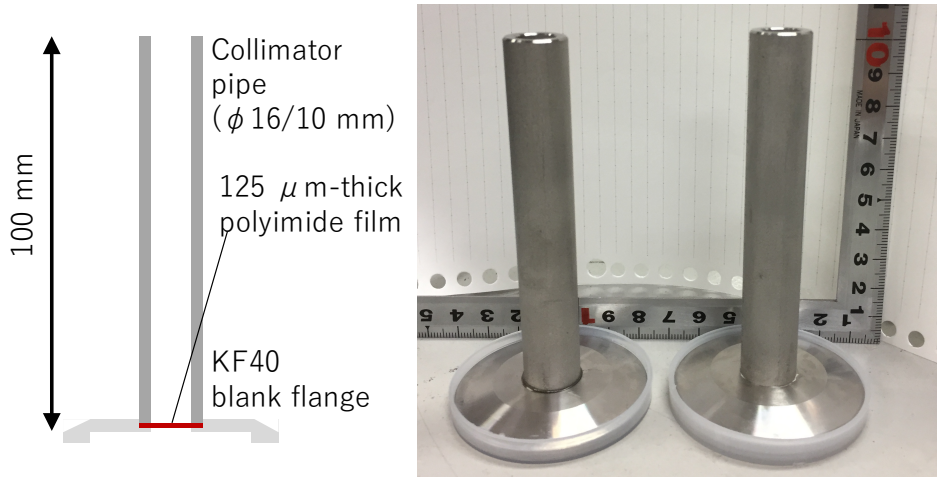

Figure 3.16: The X-ray windows located at the downstream of the system. The thickness and the outer/inner diameter of the collimator pipe are 100 mm and 16/10 mm, respectively. Left: schematics of the X-ray window. Right: a picture of the X-ray window.

of O-Rm-Tm in Fig. 3.15. The expansion of the beam width is referred to as the Borrmann fan. The effect of the Bormann fan cannot be ignored in this experiment since the crystal thickness is equal to the X-ray attenuation length and the ALP attenuation length is considered to be much longer than X rays. The Borrmann fan can expand vertically the converted beams by up to $4H\sin\theta_{\rm B} = 0.44$ mm (full width). The opening window of the four-jaw slits is set to be 2(H) $\times$ 2(V) mm^2 by taking into account the Borrmann fan.

3.4.5 X-ray window with a collimator pipe

An X-ray window located at the downstream of the system is shown in Fig. 3.16. The X-ray window is made of a 125 μm-thick polyimide film and a stainless steel pipe glued to a KF40 flange. The pipe collimates the path of signal X rays and prevents stray X rays in EH1 from entering into the downstream optics.

3.5 X-ray detection system: Germanium detector

A germanium detector (Canberra GL0210) is installed into EH3 to detect signal X rays reconverted from ALPs. The detected X rays are recorded by a DAQ electronics composed of NIM and CAMAC modules. The output of the germanium detector is amplified by an amplifier (ORTEC 572), and then the pulse height is recorded by a peak hold ADC (HOSIN C011). The internal trigger of the DAQ is made from the output with a threshold energy of 0.5 keV.

Environmental X rays with a photon energy of $\sim$ 17 keV can be misidentified

as signal X rays. It is required that the detection system has high energy resolution and a low environmental background rate.

3.5.1 Summary of detector properties

Table 3.3 shows detector properties related to the experimental sensitivity. Detailed explanation for the parameters will be given in the following subsections.

Table 3.3: Summary of the detector properties.

parameters	values
Crystal geometry	ϕ16 mm $\times$ t10 mm
Energy resolution	110.9 ± 1.9 eV (σ) at 17 keV
Gain stability during the beam time	$\pm$10 eV at 17 keV
Detection efficiency of signal X rays	82.0$\pm$1.2 %
BG count rate	0.51 ± 0.10 mHz at 17$\pm$0.23 keV

3.5.2 Energy resolution

The energy resolution of the detector is measured by using checking sources (^{241}Am, ^{57}Co and ^{55}Fe). Photon energy of these sources are 6.5 keV (^{55}Fe), 14.4 keV (^{57}Co), 26.3 and 59.5 keV (^{241}Am), respectively. The measured resolution is shown by Fig. 3.17. The energy resolution, σ, as a function of a photon energy, ω, can be deduced by using the fitting function as follows,

$$\sigma(\omega) = \sqrt{FW_{\mathrm{Ge}}\omega + \sigma_0^2} \tag{3.7}$$

where F is the Fano factor (0.05-0.13 for germanium detectors), $W_{\mathrm{Ge}} = 2.95$ eV is the work function of Ge and σ_0 is an electrical noise. The fitted values of the Fano factor and σ_0 are $F = 0.1187 \pm 0.0025$ and $\sigma_0 = 79.7 \pm 2.2$ eV, respectively. The energy resolution at a photon energy of 17 keV is calculated to be 110.9 ± 1.9 eV (1σ) from these fitted values.

3.5.3 Gain stability during the beam time

The stability of the germanium detector during the beam time is evaluated by using a ^{241}Am checking source. Figure 3.18 shows the measured calibration errors of X rays with a photon energy of 13.95 keV and 17.75 keV. The calibrated energy changes by $\sim$0.02 keV during the period (between 10/01 09:00 and 10/04 09:00) due to instability after the application of high voltage (09/29 08:30). The calibration error at the signal energy is evaluated to be 0.01 ± 0.01 keV by interpolating the errors at 13.95 keV and 17.75 keV. An energy window for signal X rays is set to be 17.01 ± 0.23 keV by taking into account the calibration error and the detector resolution (2σ).

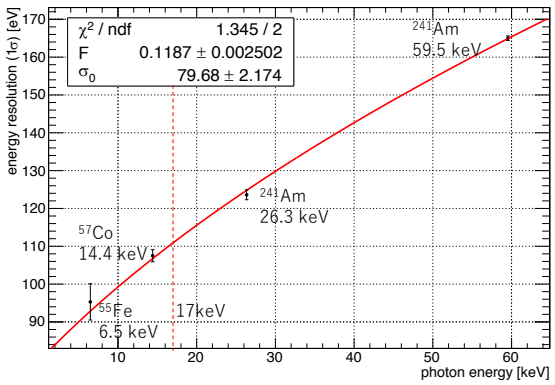

Figure 3.17: The energy resolution of the germanium detector. Data points show the energy resolution (1σ) measured by using checking sources (^{241}Am, ^{57}Co and ^{55}Fe).

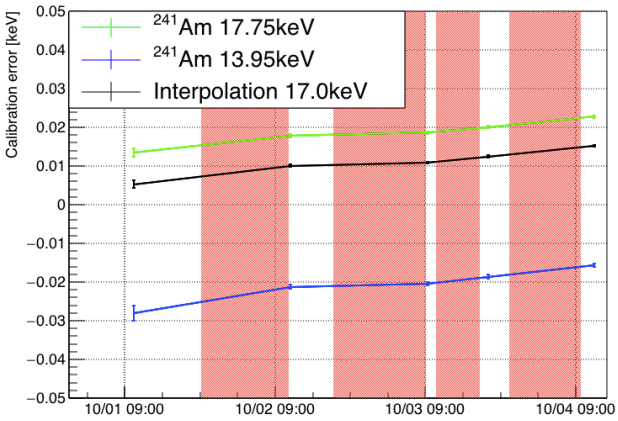

Figure 3.18: The stability of the germanium detector during the measurement of signal X rays. The calibration errors of X rays with a photon energy of 13.95 keV and 17.75 keV (^{241}Am) are shown by the blue and green data points. The calibration uses calibration constants measured at the first measurement. The black data points show the interpolated error at the signal energy (17 keV). The red areas represent the measurement of signal X rays.

3.5.4 Detection efficiency

The detection efficiency of the detector is also measured by using checking sources (^{241}Am, ^{57}Co and ^{55}Fe). The germanium detector has a thin window made of a 500 μm-thick beryllium foil, and there is a thin insensitive layer on the surface of the germanium crystal.

The thickness of the insensitive layer can be evaluated by comparing the mea-

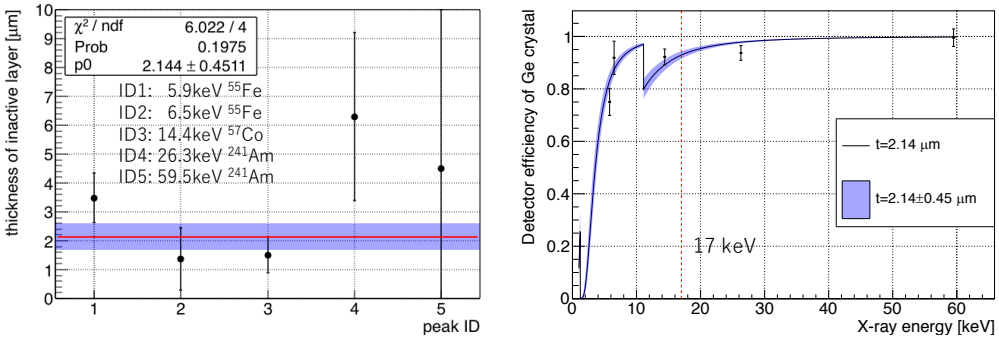

Figure 3.19: The measured thickness of the insensitive germanium layer. Left: the thickness of the insensitive layer. Right: the measured detection efficiency. The fitted value and the fitting uncertainty (1σ) are also shown by the solid line and the blue area, respectively.

sured detection rates of photons from checking sources, R_{M}, and Geant4 Monte Carlo simulation in which X-ray absorption by atmospheric molecules, windows of checking sources and the beryllium window are taken into account. The thickness of the insensitive layer, t_{il}, can be calculated from the detection rate expected by the simulation, R_{S}, as follows,

$$t_{il} = -\frac{1}{\mu_{\mathrm{Ge}}} \log\left(\frac{R_{\mathrm{M}}}{R_{\mathrm{S}}}\right) \tag{3.8}$$

where μ_{Ge} is the attenuation coefficient of germanium. The ratio, $\frac{R_{\mathrm{M}}}{R_{\mathrm{S}}}$, corresponds to the detection efficiency of the germanium crystal itself.

The measured and fitted values of t_{il} and $\frac{R_{\mathrm{M}}}{R_{\mathrm{S}}}$ are shown by Fig. 3.19. The thickness of the insensitive layer is evaluated to be 2.14 ± 0.45 μm (1σ), which is typical for germanium detectors. Reconverted X rays in this experimental setup are attenuated by 50 cm-thick air, two 125 μm-thick polyimide windows, two 275 μm-thick beryllium windows within the evacuated pipe, the detector window and the insensitive layer. The detection efficiency of signal X rays is shown by Fig. 3.20. The detection efficiency of signal X rays with a photon energy of 17 keV is estimated to be $82.0 \pm 1.2\%$ (1σ).

3.5.5 Detector shielding and background rate

Environmental X rays with a photon energy of $\sim$ 17 keV can be misidentified as the signal. The detector is covered with a two-layer shield to reduce environmental X rays. An outer shield made of 5 cm-thick lead blocks covers the detector almost all around to block environmental X rays. A 7.5 mm-thick inner brass shield absorbs X-ray fluorescence of lead.

Figure 3.21 shows the germanium detector equipped with the inner shield. An aluminum end cap of the detector contains a germanium crystal (ϕ16 mm/$\times$

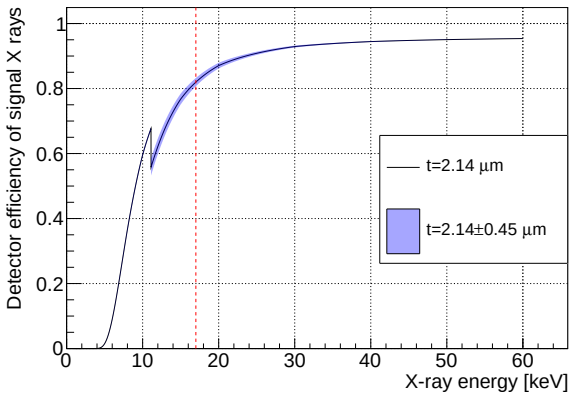

Figure 3.20: The detection efficiency of signal X rays. The uncertainty due to the thickness of the insensitive layer (1σ) is also shown by the blue area.

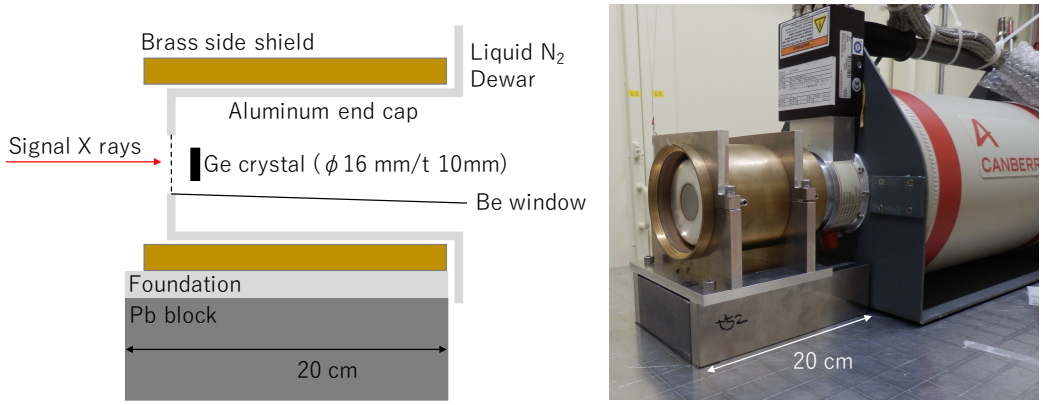

Figure 3.21: The germanium detector and its inner shield. Left: schematics of the detector and the inner shield. Right: a picture of the detector with the shield.

t10 mm) close to its edge. The 500-μm beryllium window is located in front of the germanium crystal. The inner shield is composed of a foundation and a brass cylinder covering the side of the end cap. The position of the detector crystal and the inner shield is aligned with the precision of 1 mm by using an alignment laser. The outer shield is shown by Fig. 3.22. The outer shield is composed of lead blocks with a geometry of $50 \times 100 \times 200$ mm^3. The lead block in front of the end cap has a hole with a diameter of 22 mm to introduce signal X rays into the detector.

The energy spectrum of environmental X rays is measured at EH3 before the measurement of signal X rays. The measured spectrum is shown by Fig. 3.23. The environmental X rays contain gamma rays from ^{210}Pb (46.5 keV) and X-ray fluorescence of lead ($\sim$10 keV). The detection rate of environmental X ray with a photon energy close to signal X rays (17 ± 0.23 keV) is 0.51 ± 0.10 mHz.

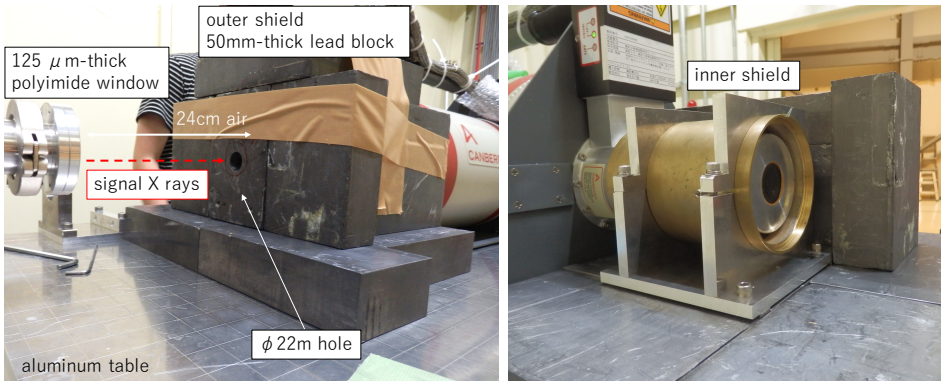

Figure 3.22: The outer shield of the germanium detector. Left: the outer shield and its position. Right: the inner shield within the outer shield.

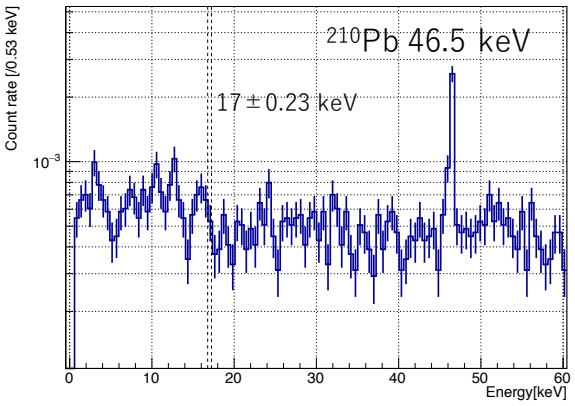

Figure 3.23: The energy spectrum of environmental X rays. The spectrum is measured before the measurement of signal X rays.

3.6 Alignment of the downstream optics

The downstream optics is aligned by the following procedure. An X-ray path in EH1 is obtained by using photon-sensitive papers. A He-Ne positioning Laser is adjusted to be coaxial to the obtained X-ray path. The Laser is used to install an optical bench parallel to the X-ray beams. The position of the channel-cut crystal is also adjusted by using the Laser.

The optics after the channel-cut crystal is aligned under the Bragg condition of the crystal. When X rays fall on the converter crystal under the Bragg condition, Laue-case X-ray diffraction within blades divides and reflect X rays as shown in Fig. 3.26 (T/R beams). The reflected X rays are subsequently reflected by the re-converter due to the parallelism between lattice planes within these crystals.

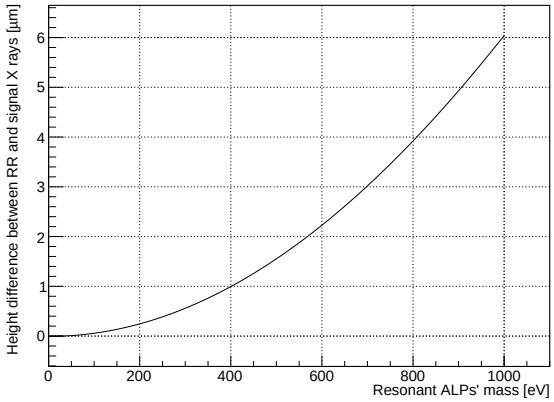

Figure 3.24: The height difference between RR beams and reconverted X rays as a function of the resonant ALPs' mass.

The X-ray beam reflected two times (RR) is almost coaxial to signal X rays as shown in Fig. 3.24. The figure shows the height difference between RR beams and reconverted X rays as a function of the resonant ALPs' mass. The difference between them is up to 6 μm (m_a = 1 keV). The positions of the four jaw slits between EH1 and EH2 are determined by monitoring the intensity of transmitted RR beams with a PIN photodiode installed in front of the germanium detector. An X-ray path within EH3 is also obtained by using photo-sensitive papers and the He-Ne Laser. The center of the germanium detector is adjusted by using the obtained X-ray path.

3.7 Rocking curve

The diffraction efficiency of the crystal depends on a detuning angle from the Bragg angle, $\Delta\theta$. The $\Delta\theta$ dependence of the efficiency is referred to as the rocking curve. The rocking curve provides important information about the goniometer angle and the X ray-ALP conversion efficiency. The diffraction efficiency of the converter and the re-converter (one time) is calculated by using the dynamical theory of X-ray diffraction as shown by the red line in Fig. 3.25. The calculation assumes that X rays are perfectly monochromatic and parallel. The transmission efficiency of X rays is also shown by the blue line. The calculated efficiencies oscillate as a function of $\Delta\theta$ due to the Bloch waves α/β within the crystals, which is referred to as the Pendellösung beat. The beating pattern is smeared in the rocking curve of the channel-cut crystal since injected X rays have finite energy bandwidth and angular divergence. The acceptable angular divergence of X-ray diffraction is 10.8 μrad (FWHM).

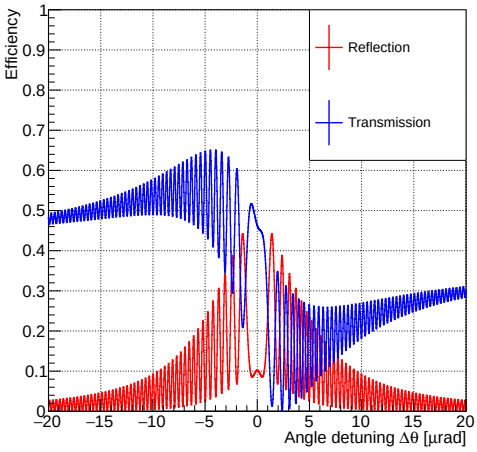

Figure 3.25: The theoretically calculated diffraction efficiency of the converter and the re-converter. The diffraction efficiencies of the reflected and transmitted beams are shown by the red and blue lines, respectively. The horizontal axis shows the detuning angle from the Bragg angle.

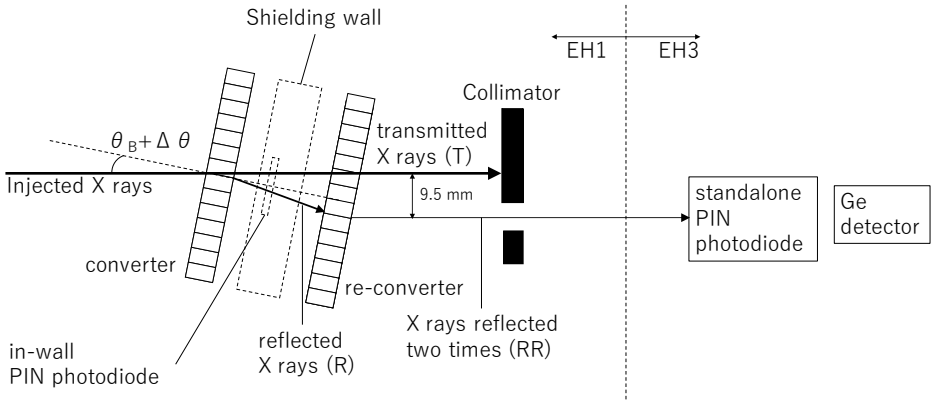

Figure 3.26: The Laue-case X-ray diffraction of the channel-cut crystal and the measurement of the rocking curve. The rocking curves of RR beams and T+R beams are measured by using a standalone PIN photodiode in front of the germanium detector and an in-wall one, respectively.

Method

The rocking curve of the channel-cut crystal is obtained by the following two methods as shown in Fig. 3.26. The rocking curve of the RR beams is measured by using a PIN photodiode (HAMAMATSU S3590-09) with a beryllium window installed in front of the germanium detector. The measured rocking curve is used to determine the zero of the detuning angle and the experimental sensitivity. The rocking

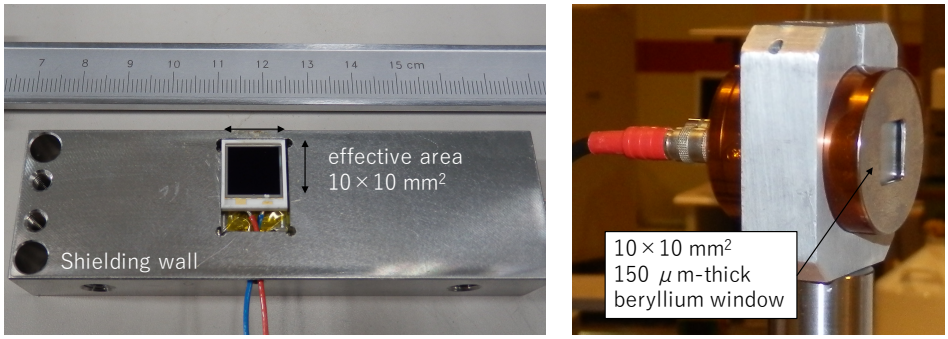

Figure 3.27: PIN photodiodes used for the measurement of rocking curves. Left: a HAMAMATSU S3590-09 PIN photodiode and the shielding wall without the aluminum window (the in-wall PIN photodiode). The photodiode is glued into a 4 mm-depth groove of the wall via a 2 mm-thick lead spacer. Right: a PIN photodiode with the beryllium window (the standalone PIN photodiode).

curve of T+R beams is also measured by using a PIN photodiode installed into the shielding wall to evaluate the drift of the goniometer angle during the measurement of signal X rays (the wall is closed). These PIN photodiodes are referred to as 'the standalone PIN photodiode' and 'the in-wall PIN photodiode' for the later convenience.

Fig. 3.27 shows the PIN photodiodes. The photodiodes have a 300 μm-thick depletion layer and an effective area of 10×10 mm^2. The photodiodes are equipped with the aluminum window shown in Sec. 3.4.3 and a 150 μm-thick beryllium window to shade the light. X rays injected into the PIN photodiodes ionize silicon atoms and generate DC-like currents, I. The X-ray intensity, N_γ, can be calculated from I by the following formula,

$$N_\gamma = \frac{W_{\mathrm{Si}} I}{e k_\gamma \epsilon_{\mathrm{PIN}}}, \tag{3.9}$$

where $W_{\mathrm{Si}} = 3.66$ eV [111] is the work function of Si and ϵ_{PIN} is the detection efficiency of PIN photodiodes.

The detection efficiency of the standalone PIN photodiode is evaluated by using GEANT4 Monte Carlo simulation. The detection efficiency of fundamental waves is estimated to be $37.51^{+0.16}_{-0}$%, where an uncertainty on an X-ray injection angle (~ 5 deg) is taken into account. The detection efficiency of the in-wall PIN photodiode is also evaluated by GEANT4 simulation and the dynamical theory of X-ray diffraction. Figure 3.28 shows the simulated detection efficiency of injected X rays. The detection efficiency depends on $\Delta\theta$ since X-ray diffraction within the converter changes the transmission efficiency of injected X rays. The measured rocking curve can be also used to determine the position of the Bragg angle. The absolute efficiency of the in-wall PIN photodiode is calibrated by using the standalone PIN photodiode.

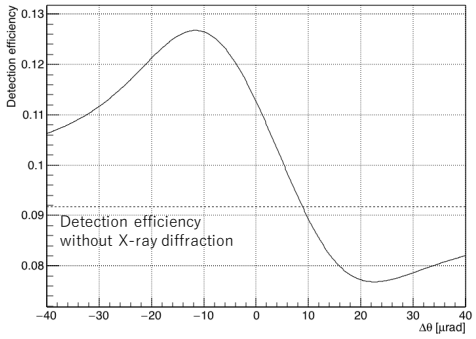

Figure 3.28: The calculated detection efficiency of the in-wall PIN photodiode. The solid line shows the detection efficiency of injected X rays as a function of $\Delta\theta$. The efficiency without X-ray diffraction is also shown by the dotted line.

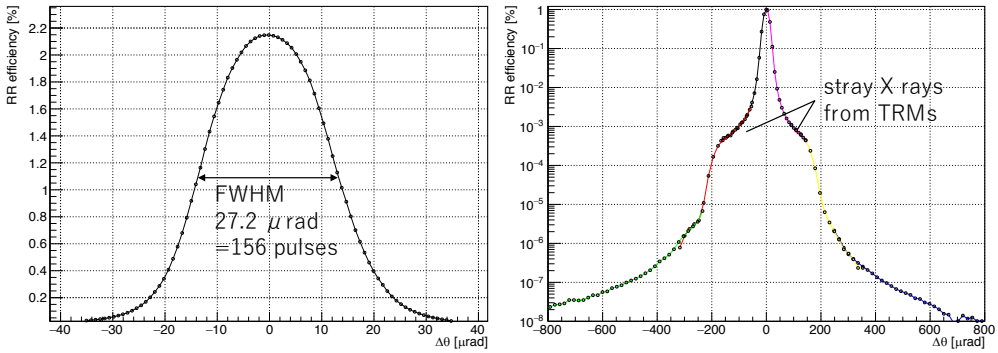

Figure 3.29: The measured rocking curve of the RR beams. Left: the rocking curve within the range of $|\Delta\theta| < 35$ μrad. Right: the broader rocking curve within the range of $|\Delta\theta| < 800$ μrad. The diffraction efficiency is normalized by the peak value. The rocking curve is measured by varying the gain of the PIN photodiode. The data points on the black, red, green, pink, yellow and blue solid lines are obtained with the relative gain of 1, 10^2, 10^5, 10, 10^3 and 10^5, respectively.

Measured rocking curve

Figures 3.29 show the rocking curves of the RR beams measured before the measurement of signal X rays. The left figure shows the rocking curve within the range of $|\Delta\theta| < 35$ μrad. The maximum diffraction efficiency is $2.15 \pm 0.01\%$, where the uncertainty is due to that of the PIN efficiency, and the width of the rocking curve is 27.2 μrad (156 pulses of the θ stage).

The Gaussian-like shape of the rocking curve represents the energy-angular distribution of the injected X rays. Figure 3.30 shows the comparison between the

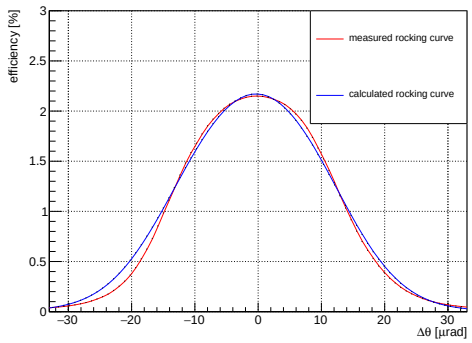

Figure 3.30: The comparison between the measured rocking curve and the calculated one.

measured rocking curve and a calculated one. The calculation assumes that the angular distribution of synchrotron radiation is Gaussian shaped with the angular divergence of 6.1 μrad (FWHM). The energy distribution of synchrotron radiation is approximated to be flat within the acceptable bandwidth of DCMs. The calculation also ignores the effect of TRMs. The calculated rocking curve has a peak efficiency of 2.17% and a width of 27.8 μrad (FWHM). These values are consistent with the measured rocking curve within the precision of 2%. The deviation between these rocking curves is considered to be due to the beam profile of synchrotron radiation and the effect of TRMs.

Injected X rays are effectively regarded as perfectly monochromatic beams with the angular divergence of $\Delta\theta_{\mathrm{BL}} = 27.2$ μrad based on the measured rocking curve. Injected X rays are assumed to have the same angular distribution as the rocking curve in the following analysis. The experimental sensitivity can be conservatively evaluated by the assumption since the width of the rocking curve is widened by X-ray diffraction at the channel-cut crystal.

Right figure of Figs. 3.29 shows a broader rocking curve within the range of $|\Delta\theta| < 800$ μrad. The side lobes in the range of $|\Delta\theta| > 200$ μrad originates from the efficiency of X-ray diffraction. The rocking curve also has an additional side lobe at $|\Delta\theta| = 100 \sim 200$ μrad. The side lobe is considered to be a speckle and stray X rays from TRMs. The number of X rays contributing to the side lobe is estimated to be 0.7% of injected X rays. The contribution of TRMs will be taken into account as a systematic uncertainty on the effective X-ray flux.

3.8 Simulation of X-ray heat load

Injected X rays are photoelectrically absorbed by the converter. The X-ray heat load on the injection point of the crystal is 41.5 mW for an X-ray flux of 2.47×10^{13} Hz during the measurement of signal X rays. Figure 3.31 shows a temperature rise under the X-ray heat load simulated by using Finite Element Method (ANSYS).

The simulation assumes that the all heat load is homogeneously applied within a parallelepiped parallel to X-ray beams with a geometry of 0.6(W)×0.5(H)×0.6(T) mm^3 (the FWHM of X-ray beams × the blade thickness), the conductivity of the silicon crystal is 148 $Wm^{-1}K^{-1}$, there are no heat conduction via the atmosphere and that the temperature of the root is constant (26 K). The maximum temperature rise at the injection point is $\Delta T = 0.34$ K.

The thermal deformation of the converter is also simulated by ANSYS from the simulated temperature rise. The simulation fixes the root of the converter, and uses the thermal expansion coefficient of $\alpha_l = 2.6 \times 10^{-6}$ K^{-1} (Si, 300 K) and the inhomogeneous young modulus of silicon [112]. The thermal deformation shifts the Bragg angle of the converter by the following two ways:

1. The X-ray heat load expands the lattice planes on the parallelepiped by $\frac{\Delta d}{d} = 5.49 \times 10^{-7}$ on the surfaces where the expansion is most significant. The expansion of the lattice planes shifts the Bragg angle by $-\frac{\Delta d}{d}\tan\theta_{\rm B} = -106.2$ nrad.

2. The heat stress distorts the crystal structure and inclines the lattice planes since X rays are injected diagonally. The lattice planes' inclination changes the effective Bragg angle of the converter by +10.4 nrad.

The overall shift of the Bragg angle is estimated to be $\Delta\theta_{\rm B} = -95.8$ nrad from them. Figure 3.32 shows the mesh-size dependence of the simulated effective shift. The mesh-size dependence is $\sim \pm 1\%$. The shift during the measurement of signal X rays is estimated to be 95.8 ± 1.5 nrad, where the uncertainty comes from the mesh-size dependence and the uncertainty on the X-ray flux shown in Chap. 4 (up to $\pm 1.3\%$). The efficiency of the conversion and the reconversion is numerically calculated to be $\epsilon_S = 84.1 \pm 0.4\%$.

3.9 Temperature monitor

The room temperature of EH3, the temperature around the goniometer, the detector and its electronics are monitored by platinum resistance thermometers during the measurement of signal X rays. The monitored temperature are shown by Fig. 3.33. An air-conditioning system of EH1/3 keeps the temperature change within ±0.2 K. The temperature drift of EH3 corresponds to the weather. The first and third day (10/1, 10/3) were sunny and the second and fourth day (10/2, 10/4) were cloudy. The jump of the detector temperature is possibly due to an electrical noise or a contact failure of the thermometer.

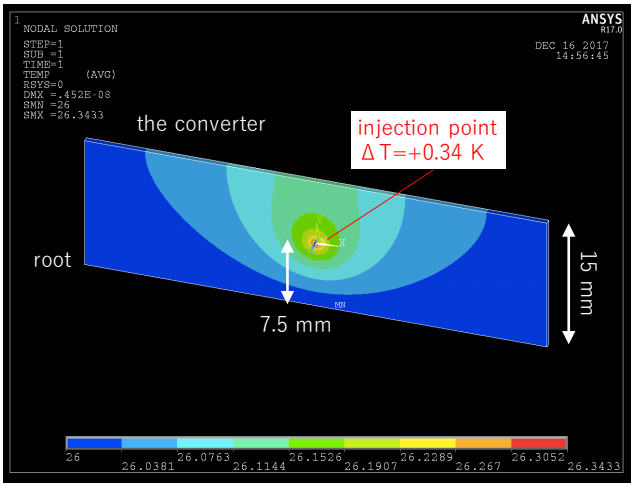

Figure 3.31: The simulated temperature rise under the maximum X-ray heat load of 41.5 mW during the measurement of signal X rays.

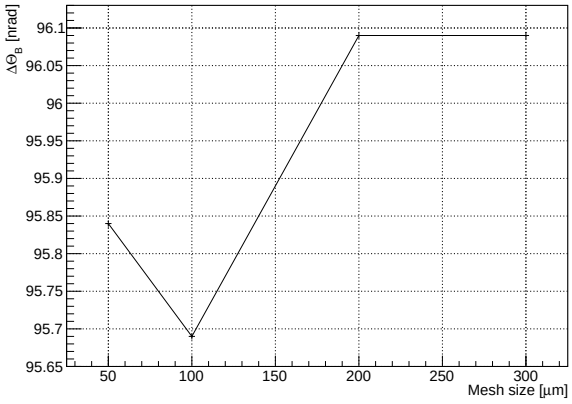

Figure 3.32: The simulated thermal deformation under the maximum X-ray heat load. The effective shift of the Bragg angle is shown as a function of a mesh size.

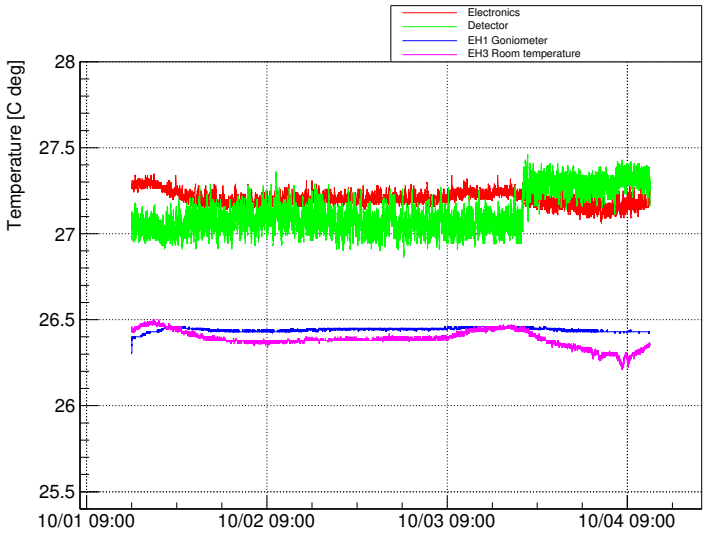

Figure 3.33: The room temperature during the measurement of signal X rays.

Chapter 4

Data taking and analysis

The experimental procedure for the measurement will be shown firstly. The experimental parameters related to the experimental sensitivity are explained secondly. The analysis and an upper limit will be given lastly. The detuning angle from the Bragg angle, $\Delta\theta$, is described by the number of stepping pulses (1 pulse=0.17 μrad) for the convenience of the analysis. The detected X rays within the energy window are referred to as 'signal X rays' in this section.

4.1 Data taking

The signal X rays are measured before the beam dump at 10/04 09:53. There are four datasets summarized in Table 4.1. The sum of the data acquisition time is 1.70×10^5 s (47.2 hour). Two beam dumps takes place during the third and fourth data takings. These datasets are obtained by the following procedures:

1. The shielding wall is closed. It takes about an hour until the goniometer angle is stabilized after the closure of the wall.

2. The rocking curve of the T+R beams is measured by using the in-wall PIN photodiode. The zero point of the detuning angle (the Bragg angle) is obtained from the rocking curve.

3. The detuning angle is scanned pulse-by-pulse with a stepping time of t_{DAQ} toward the direction in which the detuning angle increases (clockwise). The range of the scanning is set to include $0 < \Delta\theta < 4.7$ mrad (27000 pulses), which corresponds to the resonant ALP's mass of m_a <1 keV. Signal X rays are measured by the germanium detector.

4. The goniometer angle is reset to the Bragg angle. The rocking curve of the T+R beams is measured again to evaluate the drift of the goniometer angle, $\Delta\theta_{\mathrm{D}}$, after waiting about one hour.

Stability of the X-ray energy and profiles

The stability of the X-ray beams during the measurement of signal X rays is briefly discussed in this paragraph. The photon energy of X rays is selected by X-ray diffraction of DCM. The lattice constant on the X-ray injection point on DCM changes slightly due to the X-ray heat load, whose expansion rate is reduced by using the liquid nitrogen cooling of the crystals. It takes < 30 minutes for the injection point to reach the thermal equilibrium. The energy fluctuation under the thermal equilibrium is within the energy bandwidth and negligible [113].

The fluctuation of the beam profile is also evaluated by rocking curves of the RR beams in the same way as Sec. 3.7. The FWHM widths of these rocking curves are $\Delta\theta = 156$ pulses (measured before the first dataset, Sec. 3.7), $\Delta\theta = 155$ pulses (between the first and second datasets), 152 pulses (after the first beam dump) and 160 pulses (after the second beam dump). The large fluctuation of the last measurement is considered to be caused by the change of the beam current from 100 to 70 mA. Although the fluctuation of the beam profiles does not change the number of signal X rays, the S/N ratio of the experiment deteriorates when the beam profiles are wider due to the integration of environmental X rays as shown later. The effective width of the injected X rays is assumed to be the maximum value of $\Delta\theta_{\rm BL}$=156 pulses to evaluate the experimental sensitivity conservatively.

Table 4.1: The datasets of measured signal X rays. N_γ: the intensity of injected X rays. $\Delta\theta$: the detuning angle. $t_{\rm DAQ}$: the stepping time per pulse. $\Delta\theta_D$: the drift of the goniometer angle. $\Delta\theta_S$: the position of a sub peak around $\Delta\theta = 21300$ pulses.

No.	Period	N_γ [10^{13} Hz]	$\Delta\theta$ [pulse]	$t_{\rm DAQ}$ [s/pulse]	$\Delta\theta_D$ [pulse]	$\Delta\theta_S$ [pulse]
1	01 21:05∼02 11:11	$2.446^{+0.56\%}_{-0.71\%}$	−236 ∼27964	1.8	−90	21273
2	02 18:27∼03 08:56	$2.451^{+0.56\%}_{-0.71\%}$	−323 ∼27877	1.85	−35	21238
3	03 10:39∼03 17:39	$2.473^{+0.66\%}_{-0.79\%}$	−462 ∼22840	1.08	−62	21262
4	03 22:16∼04 09:52	$2.430^{+1.2\%}_{-1.3\%}$	−289 ∼18150	2.265	−74	none

4.2 Experimental parameters of datasets

As shown in Table 2.2 and Eq. (2.6), the experimental sensitivities to m_a and $g_{a\gamma\gamma}$ depend on the following parameters:

1. The effective angular divergence of injected X rays, $\Delta\theta_{\rm BL}$.
2. The reduction factor of the conversion probability due to X-ray heat load, ϵ_S.
3. The photon flux, N_γ.
4. The detuning angle, $\Delta\theta$.

5. The number of signal X rays per step, N_i^s.
6. The intensity of the effective electric fields within the crystal, E_T.
7. The effective conversion length, $L_{\rm eff}$.
8. The detection efficiency of signal X rays, ϵ_d.
9. The DAQ time, $T_{\rm DAQ}$.

The value of $\Delta\theta_{\rm BL}$ and ϵ_S are evaluated by the measured rocking curves of the fundamental waves and the thermodynamical simulation as shown in Chap. 3. The photon flux is monitored by the in-wall PIN photodiode. The drift of the detuning angle is also measured by using the PIN photodiode. The four datasets are combined to obtain an integrated number of signal X rays as a function of $\Delta\theta$ by taking into account the measured drift of the goniometer angle. These values will be explained in detail in the following subsections.

The values of E_T, $L_{\rm att}$ and ϵ_d have been explained in Chap. 3. The uncertainties on them will be discussed in the next section. The uncertainty on $T_{\rm DAQ}$ is negligible since the time is determined by a system clock of the operating computer.

4.2.1 Intensity of injected X rays: N_γ

The intensity of injected X rays, N_γ, is monitored by using the in-wall PIN photodiode. Figures 4.1 show the output of the PIN photodiode as a function of the detuning angle. The outputs have spikes with a width of $\Delta\theta = 1$ pulse possibly caused by electric noises. The intensity of the injected X rays is evaluated by the peak height of the rocking curve around the Bragg angle. The efficiency of the in-wall PIN photodiode is calibrated by comparing its output with that of the standalone PIN photodiode. The evaluated intensity has an uncertainty due to the uncertainty on the detection efficiency of the latter PIN photodiode, $^{+0\%}_{-0.43\%}$.

The monitored outputs have a sub peak around $\Delta\theta = 21300$ pulses=3.7 mrad as shown in Figs. 4.1. The peak is considered to be a rocking curve of lattice planes other than Si(220). The candidates for the lattice planes can be deduced geometrically as shown in Figs. 4.2. The left figure descries the Bragg condition of Si(220) lattice planes by using the reciprocal lattice space. The wavenumber vector of injected X rays, $\mathbf{k}_0$, is represented by a vector terminating on the origin of the space, (000), in the space. A sphere with a radius of $|\mathbf{k}_0|$ centered on the initial end of $\mathbf{k}_0$ is defined for the later convenience. The Bragg condition of (hkl) lattice planes is satisfied when a point (hkl) falls on the surface of the sphere. The wavenumber vector of diffracted X rays is given by the vector from the center of the sphere to the point (hkl). The origin of the sphere is $(-1, -1, 7.66)$, the radius of the sphere is 7.8 and the diffraction plane is parallel to $(0, 0, -1)$ in this experimental setup. The diffraction of Si(220) lattice planes can take place even if the whole system is rotated with an azimuth angle, ϕ, around the momentum transfer vector represented by $\mathbf{H}$.

The candidate for the sub peak can be deduced as shown in the right figure. The Bragg condition for (h', k', l') lattice planes is geometrically calculated by the sphere. And then the detuning angle from the Bragg condition of Si(220), $\Delta\theta$, and the azimuth angle, ϕ, are deduced as a function of the lattice index, (h', k', l'). Table 4.2 shows the candidates for the sub peak with $\Delta\theta = 3.7$ mrad and $\phi <$ 4 mrad. The azimuth angle ~ 3.8 mrad can be caused by the mechanical precision of the channel-cut crystal ~ 0.9 mrad, the alignment precision of the optical bench ~ 1 mrad and the fixation of the crystal.

Table 4.2: The candidate lattice planes for the sub peak.

(h', k', l')	azimuth angle [mrad]
$(-5, -1, 1)/(-1, -5, 1)$	3.8
$(-2, 0, 0)/(0, -2, 0)$	3.7

The output of the PIN photodiode fluctuates due to the fluctuation of the X-ray intensity itself and X-ray diffraction of other lattice planes. Since the regions $\Delta\theta < 6000$ pulses and $\Delta\theta > 16000$ are affected by X-ray diffraction of Si(220) and the sub peak, the fluctuation of the X-ray intensity during the data taking is evaluated by the fluctuation of the output in the range of $6000 < \Delta\theta < 16000$ pulses. Figure 4.3 shows the fluctuation in the range for the four datasets. Their outputs are consistent with each other within their fluctuation. The fluctuation of N_γ within the $\Delta\theta$ range for the first, second, third and fourth measurement are $\pm 0.56\%$, $\pm 0.56\%$, $\pm 0.63\%$ and $\pm 1.2\%$, respectively, where fine spikes due to electric noises are ignored. The enhancement of the fluctuation during the third and fourth measurement is possibly due to the instability of the storage ring. The uncertainty on N_γ is evaluated by the fluctuation and the uncertainty on the detection efficiency of the standalone PIN photodiode.

4.2.2 Drift of the goniometer angle: $\Delta\theta$

The drift of the goniometer angle is measured by the in-wall PIN photodiode before and after the data takings. The measured drift are -90, -35, $+67$ and -17 pulses during the first, second, third and fourth measurement, respectively. The drift of the first measurement is enhanced because only six hours have passed since the closure of EH1 (10/01 15:00) and the temperature around the goniometer fluctuates. The drift of the second measurement is three times smaller than that of the first measurement. The drift during the third and fourth measurement are measured with less accuracy because beam dumps take place.

The measured drift can be cross-checked by the position of the sub peak, $\Delta\theta_S$, shown in Figs. 4.1. The $\Delta\theta_S$ of the first and second measurement without the drift are estimated to be consistent with each other (21205/21211 pulses, respectively) by assuming that the drift is proportional to $\Delta\theta$. The drift during the third mea-

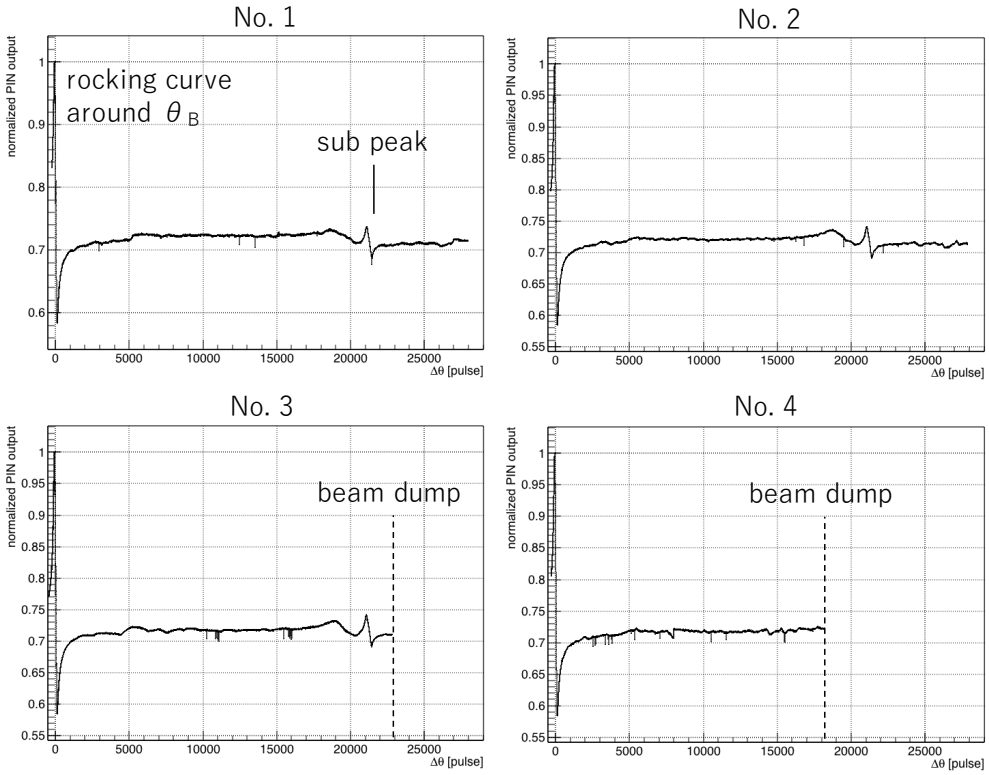

Figure 4.1: The monitored output of the PIN photodiode within the wall. The fine spikes on these spectrums last only $\Delta\theta = 1$ pulses and originates from the electric noise of the PIN photodiode and the DAQ system. Two beam dumps take place during the third and fourth measurement.

surement is evaluated to be -62 pulses from the measured $\Delta\theta_S$ of 21262 pulses and the position without the drift of 21205 pulses (based on the first measurement). The deviation between the estimated drift and the measured one may be attributed to the beam dump and checking works after the first beam dump (open and closure of the wall, measurements of rocking curve). The drift during the fourth measurement is conservatively estimated to be -74 pulses from the maximum drift during the first measurement by assuming that the drift is proportional to the DAQ time. The estimated drift, $\Delta\theta_D$, does not affect significantly the experimental sensitivity since the drifting speed is only 0.3% of the scanning one. However, the drift should be taken into account to integrate the four datasets since the goniometer angle drifts differently among them. The integration taking into account $\Delta\theta_D$ will be discussed in the next section.

The goniometer angle also changes momentarily when the stepping motor is driven. It is considered to be attributed to the distortion of the rotation coupler. Figure. 4.4 shows the magnified view of Fig, 4.1 around the Bragg angle (the third

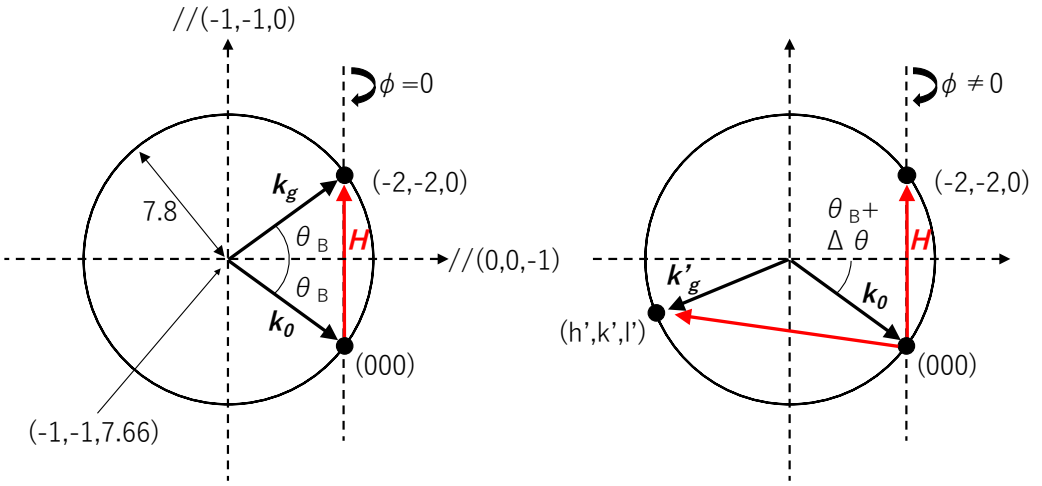

Figure 4.2: The geometrical expression of the Bragg condition. These schematics show the relation between wavenumber vectors of injected and reflected X rays on the reciprocal lattice space. Left: the Bragg condition of Si(220) with the designed geometry. Right: the Bragg condition of other lattice planes. The azimuth angle from the designed geometry, ϕ, is considered.

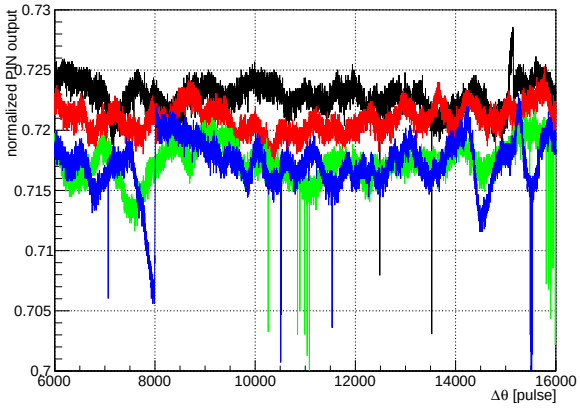

Figure 4.3: The fluctuation of the PIN output during the data taking. There are no significant effects due to X-ray diffraction in the $\Delta\theta$ range, 6000 pulses $< \Delta\theta <$ 16000 pulses. The PIN output is normalized by their maxima under the Bragg condition. Black: the first dataset. Red: the second one. Green: the third one. Blue: the fourth one.

measurement). The rocking curve has a periodic spikes due to the coincidence of the data logging with a period of 1 s and the driving with a period of 1.08 s. The duration of the temporal drift is estimated to be $\sim$0.17 s/pulse from the frequency of the spikes, which is consistent with that of the driving (0.16 s/pulse). The

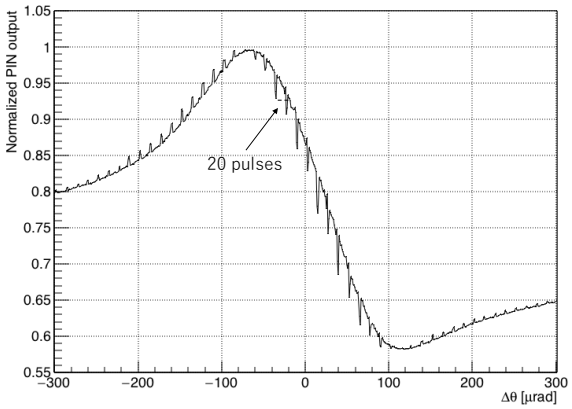

Figure 4.4: The magnified view of Fig. 4.1 around the Bragg angle (the third measurement). The spikes on the rocking curve correspond to the driving of the stepping motor.

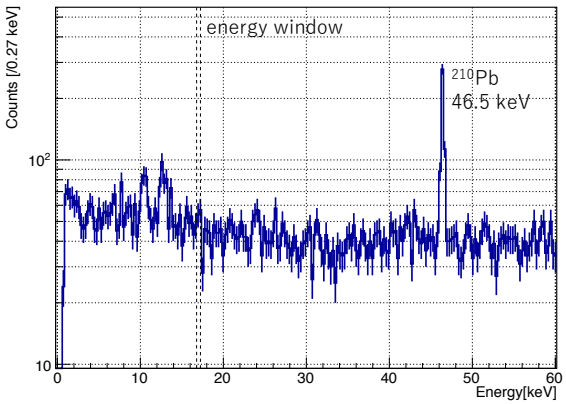

Figure 4.5: The energy spectrum of X rays detected during the measurement of signal X rays. The energy window for signal X rays is also shown by the dotted line.

fluctuation due to the movement of the goniometer changes the effective goniometer angle by $\Delta\theta_{\mathrm{TD}}$ =+20 pulses temporally. The temporal drift will be taken into account in the next section to integrate X-ray events with adjacent detuning angles.

4.2.3 Energy spectrum of detected X rays: N_i^s

The energy spectrum of detected X rays is shown in Fig. 4.5. The number and the detection rate of X rays within the energy window is 94 photons and 0.554 ± 0.057 mHz, respectively. The detection rate is consistent with the rate of environ-

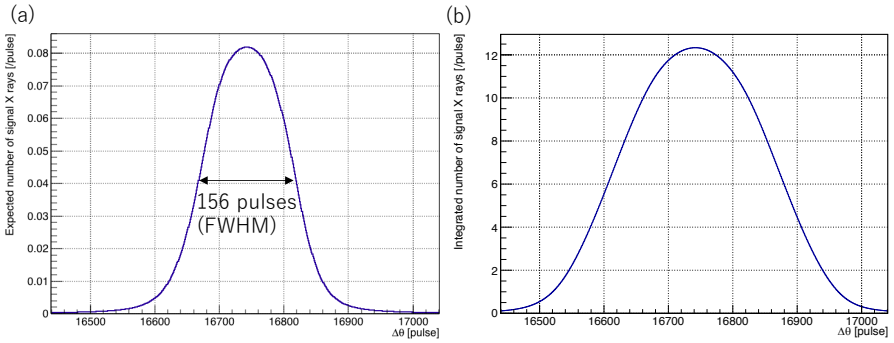

Figure 4.6: The expected distribution of signal X rays as a function of $\Delta\theta$ for the datasets. The ALPs' mass and the coupling constant are assumed to be $m_a = 794$ eV and $g_{a\gamma\gamma} = 5 \times 10^{-3}$ GeV^{-1}, respectively. (a) the expected number per pulse. (b) the integrated number of expected signals within a $\Delta\theta$ window shown below.

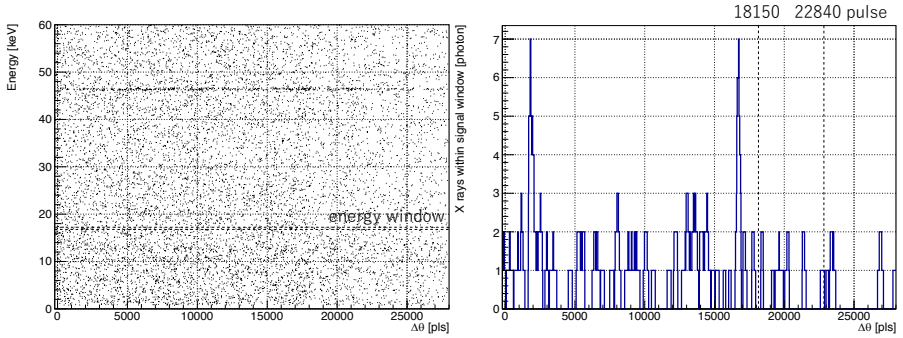

Figure 4.7: The $\Delta\theta$ distribution of the detected X rays within the signal region. Left: the energy-$\Delta\theta$ distribution of detected X rays. The simple sum of four datasets is used. The energy window for signal X rays is shown by the dotted line. Right: the integrated number of detected signal X rays within the $\Delta\theta$ windows.

mental X rays (0.51 ± 0.10 mHz) measured without X rays.

If ALPs exist, the detection rate of signal X rays is enhanced at a certain $\Delta\theta$ corresponding to the ALPs' mass. Figure 4.6 (a) shows a expected $\Delta\theta$ distribution of signal X rays for the datasets. The ALPs' mass and the coupling constant are assumed to be $m_a = 794$ eV and $g_{a\gamma\gamma} = 5 \times 10^{-3}$ GeV^{-1}, respectively. The signal X rays have a Gaussian-like distribution determined by the rocking curve with a center of $\Delta\theta = 16740$ pulses and a FWHM width of 156 pulses. The signal X rays can be integrated within a $\Delta\theta$ window to enhance the statistic of signal X rays as shown in Fig. 4.6 (b) since the measurement at adjacent detuning angles have the sensitivity to almost the same ALP's mass.

Figure 4.7 shows the $\Delta\theta$ distribution of the detected X rays. The left figure is

the energy-$\Delta\theta$ distribution obtained by simply summing four datasets. Detected X rays within the energy window are integrated with a $\Delta\theta$ window in order to evaluate the number of signal X rays related to a certain ALP's mass. The $\Delta\theta$ window for the integration should take into account the drift of the goniometer angle, $\Delta\theta_{\rm D}$ and $\Delta\theta_{\rm TD}$, to combine the four datasets. Figure 4.8 shows schematics of the integration. The analysis uses the second measurement as the standard of $\Delta\theta$ because the drift during the measurement is the smallest among the four datasets. The $\Delta\theta$ window represented by red dotted lines is determined as follows,

1. The $\Delta\theta$ window for $\Delta\theta = i$ pulses is set to be $[i-98, i+78]$ pulses in the second dataset. The window width is determined by the effective angular divergence, $\Delta\theta_{\rm BL} = 156$ pulses. The lower side of the window is widened by $\Delta\theta_{\rm TD}$=20 pulses to include the temporal drift of the goniometer angle. The drift during the measurement ($\Delta\theta_{\rm D} = -35$ pulses) can be ignored since the drifting speed is much slower than the scanning speed.

2. The drift during the first and the second measurement are estimated to be within the range of $[-90, 0]$ and $[-35, 0]$ pulses, respectively, from the measured values of $\Delta\theta_{\rm D}$. The maximum deviation of $\Delta\theta$ between them is $[-90, +35]$ pulses. The $\Delta\theta$ window in the first dataset is widened from the second dataset by $[-35, +90]$ pulses ($[i-133, i+168]$) to compensate the deviation.

3. The $\Delta\theta$ window in the third dataset is widened by $[-35, +62]$ pulses ($[i-133, i+140]$) by the same way as the first dataset.

4. The drift during the fourth measurement has uncertainty due to the beam dump. The drift is estimated to be $\Delta\theta_{\rm D} = -74$ pulses in this analysis. The $\Delta\theta$ window in the fourth dataset is widened by $[-35, +74]$ pulses ($[i-133, i+152]$).

All datasets are combined after the integration in each datasets. Figs. 4.7 also show the integrated number of detected X rays. The maximum number is 7 photons per pulse (1794∼1836 pulses and 16725∼16747 pulses). The peak around 16725∼16747 pulses is compared with the expected distribution as shown in Fig. 4.9. Although the measured distribution is consistent with the expected one ($g_{a\gamma\gamma} = 4.3 \times 10^{-3}$ GeV^{-1}), the statistics of detected X rays are too small to detect possible deviation between them. The peak can be also explained by accidental accumulation of environmental X rays.

Figure 4.10 shows the probability distribution function (PDF) of the maximum peak height caused by environmental X rays. The PDF is calculated by the following procedure. The number of detected X rays within the signal window during four data takings are 27, 25, 15 and 27 photons, respectively. The all X rays are assumed to be environmental X rays independent of $\Delta\theta$. These numbers are consistent with each other within their statistical uncertainties ($\sim 20\%$). The $\Delta\theta$ distribution of environmental X rays is numerically simulated for four data takings

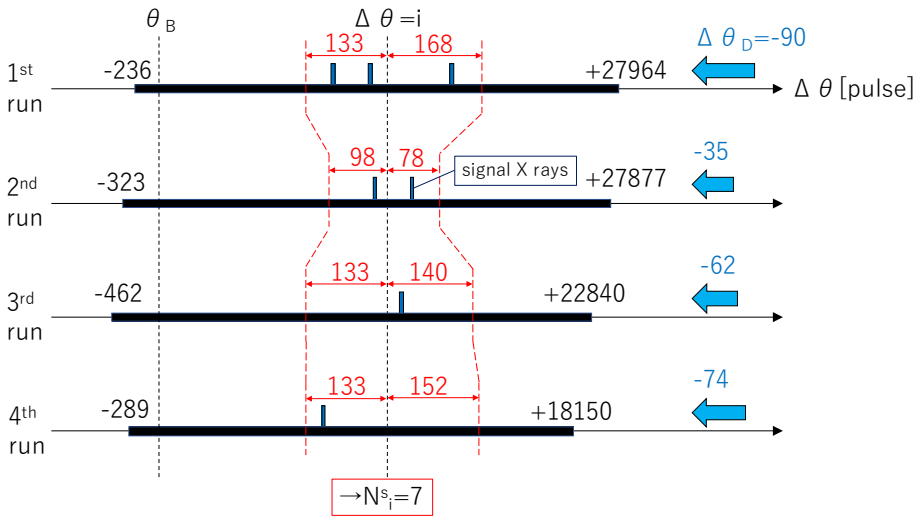

Figure 4.8: The integration of detected signal X rays and the combination of four datasets. The scanning ranges of $\Delta\theta$ in each datasets are shown by the black bands. The drifts of the goniometer angle during each measurements are shown by the blue arrows. The detected signal X rays are shown by the blue boxes as a function of $\Delta\theta$. The $\Delta\theta$ window for the integration is shown by the red dotted lines. The integrated number of signal X rays for $\Delta\theta = i$ is 3+2+1+1=7 in this figure.

by assuming that their intervals obey an exponential distribution with a rate parameter reproducing the numbers of detected X rays shown above. The statistical uncertainties on the numbers are taken into account by varying the rate parameter as a random number obeying the Gaussian distribution. The $\Delta\theta$ distribution of four data takings is combined by integrating within the $\Delta\theta$ window. The PDF is obtained by generating the integrated $\Delta\theta$ distribution 10^6 times.

The probability that environmental X rays make a peak higher than 6 photons is 4.4% ($\sim 1.7\sigma$), and the detected X rays are not significant enough to distinguish signals caused by ALPs with pseudo signals made by environmental X rays. The probability that environmental backgrounds make two or more peaks with a photon number of > 6 (away from each other by > 156 pulses) is also calculated to be 0.14% ($\sim 3\sigma$) by the same way. The significance due to the twin peaks may be explained by the possible fluctuation of environmental X rays since the statistic of detected X rays within the signal window is only $10^{1\sim2}$ for each data takings and the p-value of the twin peak strongly depends on the environmental X-ray rate. Although the peaks can be also interpreted as signals caused by twin ALPs with different masses and the possibility has to be verified by future searches, the sensitivity to $g_{a\gamma\gamma}$ can be arbitrarily enhanced by assuming multiple ALPs. The possibility is outside the reach of the analysis in this thesis.

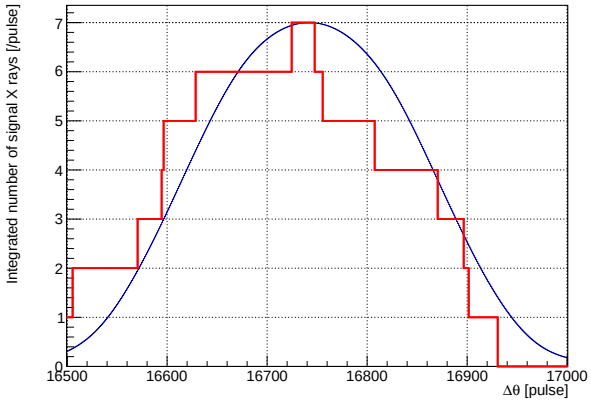

Figure 4.9: The comparison between expected distribution of integrated signal X rays and measured one. Red: the measured distribution around the peak at 16725∼16747 pulses. Blue: the expected distribution shown in Fig. 4.6 (b). The coupling constant is assumed to $g_{a\gamma\gamma} = 4.3 \times 10^{-3}$ GeV^{-1} in this case.

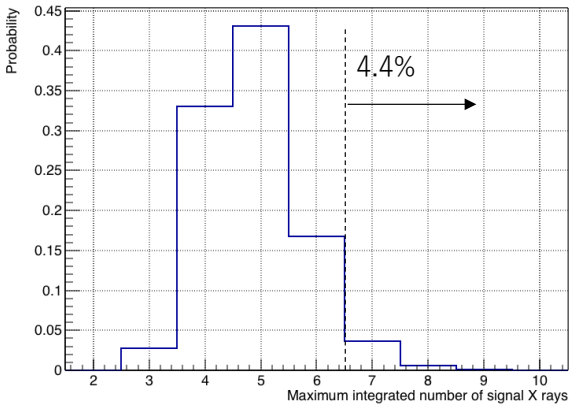

Figure 4.10: The probability distribution function of the peak height caused by environmental X rays in this analysis. The histogram takes into account the statistical uncertainty on the number of detected X rays within the signal window.

4.3 Analysis of the upper limit on $g_{a\gamma\gamma}$

Although significant signals are not observed, an upper limit for ALPs can be obtained by the experiment. The upper limit on $g_{a\gamma\gamma}$ can be calculated as a function of m_a by the following formula,

$$\sum_{\Delta\theta=\Delta\theta_i-78}^{\Delta\theta_i+78} \left(\int P^2(\Delta\theta + \theta_X, m_a) N_\gamma^i \frac{dF}{d\theta_X} d\theta_X \right) \epsilon_d \epsilon_S < N_{i,CL}^s \tag{4.1}$$

where $\Delta\theta_i$ is the detuning angle ([pulse]), $P^2(\Delta\theta, m_a)$ is the X ray-ALP conversion-reconversion probability, N_γ^i is a total number of injected X rays during $\Delta\theta = \Delta\theta_i$, $\frac{dF}{d\theta_X}$ is the effective angular distribution of X rays (the rocking curve) and $N_{i,CL}^s$ is an upper limit on the number of signal X rays during $\Delta\theta = \Delta\theta_i$. The value of $N_{i,CL}^s$ can be evaluated by assuming the Poisson distribution as follows,

$$\int_0^{N_{i,CL}^s} \frac{\mu^{N_i^s}}{N_i^s!}\exp(-\mu)d\mu = 1 - CL, \tag{4.2}$$

where N_i^s is the integrated number of detected events during $\Delta\theta = \Delta\theta_i$ as shown in the previous subsection and CL is a confidence level. The contribution from $\Delta\theta = \Delta\theta_i \pm 78$ pulses are summed since they share the same resonant ALP's mass. The calculation is performed for $\Delta\theta_i = -100 \sim 27800$ pulses, and the lowest upper limits among them are deduced as a function of m_a.

When the resonant conversion condition is fulfilled, the upper limit for the coupling constant can be simplified as follows,

$$g_{a\gamma\gamma} < \left(\frac{1}{2}E_T L_{\rm eff}\cos\theta_{\rm B}\right)^{-1}\left(\frac{N_\gamma'^i \epsilon_d \epsilon_S}{N_{i,CL}^s}\frac{\Delta\theta_{\rm CV}}{\Delta\theta_{\rm BL}}\right)^{-\frac{1}{4}}, \tag{4.3}$$

$$m_a = \sqrt{m_\gamma^2 + 2q_T\left(k_\gamma \sin(\theta_{\rm B} + \Delta\theta_i) - \frac{q_T}{2}\right)}, \tag{4.4}$$

where $N_\gamma'^i \sim 156 N_\gamma^i$ is the sum of N_γ^i within the $\Delta\theta$ window. The effective angular divergence, $\Delta\theta_{\rm BL}$, affects the experimental sensitivity only via $N_{i,CL}^s$ due to the relation, $N_\gamma'^i \propto \Delta\theta_{\rm BL}$. Systematic uncertainties related to the experimental sensitivity are examined in the following subsections.

4.3.1 Systematic uncertainties

Table 4.3 summarizes systematic uncertainties related to the sensitivity to $g_{a\gamma\gamma}$ and m_a. Each uncertainties will be subsequently explained in the following paragraphs.

Uncertainty on the effective electric field: E_T

The effective electric field, E_T, can be calculated with the Moliére approximation. The approximation assumes the atomic electric potential as the composition of screened coulomb potentials as shown in Eq. (A.67). Although the atomic potential deduced from the approximation is in a good agreement with measurement of high-energy electron/proton multiple scattering within an experimental precision of 2 to 3 % [114, 115], the atomic potential can be deviated from the one exactly calculated. The accurate solution for the atomic solution can be obtained by using the Dirac-Fock (DF) method [116,117]. The deviation between the effective electric fields calculated by the Moliére approximation and the DF method is 7.5%. The deviation is taken into account as the uncertainty on E_T.

uncertainty	factor	uncertainties on $g_{a\gamma\gamma}$	m_a
Moliér approximation	E_T	+7.5%	
blade thickness	$L_{\rm eff}/\Delta\theta_{CV}$	±0.48%	
the beam intensity	N_γ^i	±0.33%	
Stray X rays from TRMs	N_γ^i	+0.18%	
drift of $\Delta\theta$	$N_\gamma^i/\Delta\theta_i$	±0.08%	±0.15%
absolute accuracy of $\Delta\theta$	$\Delta\theta_i$		±0.18%
detector efficiency	ϵ_d	±0.37%	
conversion efficiency	ϵ_S	±0.26%	
Bormann effect of sub peak	$L_{\rm eff}$	0%/+3.7%/+1.4% (lower/Bragg/higher)	
Overall (conservative)		+9.2%/+12.9%/+10.6%	-0.33%

Table 4.3: Summary of systematic uncertainties on $g_{a\gamma\gamma}$ and m_a.

Uncertainty on the blade thickness: $L_{\rm eff}$

The machining accuracy of the channel-cut crystal is ±5 μm. The effective conversion length, $L_{\rm eff}$, is roughly proportional to the blade thickness, and the acceptable angular divergence of the conversion, $\Delta\theta_{CV}$, is inversely proportional to it. The uncertainty on $g_{a\gamma\gamma} \propto L_{\rm eff}^{-1}\Delta\theta_{CV}^{\frac{1}{4}}$ due to the machining accuracy is ±0.48%.

Uncertainty on the X-ray flux: N_γ

The intensity of injected X rays, N_γ^i, has uncertainties due to the calibration of PIN photodiodes and the fluctuation of X-ray intensity. The uncertainty on N_γ^i is up to ±1.3%, and the uncertainty on $g_{a\gamma\gamma} \propto \left(N_\gamma^i\right)^{-\frac{1}{4}}$ is ±0.33%.

Stray X rays from TRMs: N_γ

The injected X rays contain stray X rays scattered from TRMs. The contaminant X rays reduce the effective flux of injected X rays by 0.7%. The uncertainty on $g_{a\gamma\gamma} \propto \left(N_\gamma^i\right)^{-\frac{1}{4}}$ is +0.18%.

Uncertainty on the goniometer angle: $N_\gamma/\Delta\theta$

The drifting speed of the goniometer angle is up to 0.3% of the scanning speed. The drift can reduce the total intensity of injected X rays, N_γ^i, and the detuning angle, $\Delta\theta_i$ by 0.3%. The uncertainty on $g_{a\gamma\gamma}$ and $m_a \propto \sqrt{\Delta\theta_i}$ due to the drift is ±0.08% and ±0.15%, respectively. In addition to the drift, the goniometer has the absolute accuracy of ±0.36%. The absolute accuracy is measured by the deviation between the rocking curve of Si(220)/fundamental waves and that of

Si(10,10,0)/third harmonics as shown in Appendix B. The resonant ALP's mass has an additional uncertainty of ±0.18% from the absolute accuracy.

Uncertainty on the detection efficiency: ϵ_d

The detection efficiency of the germanium detector is $82.0 \pm 1.2\%$ for X rays with a photon energy of 17 keV. The uncertainty comes from the thickness of the insensitive layer on the detector crystal. The uncertainty on $g_{a\gamma\gamma} \propto \epsilon_d^{\frac{1}{4}}$ is ±0.37%.

Uncertainty on the conversion efficiency: ϵ_S

The injected X rays with high heat load change the Bragg angle of the converter by 95.8 ± 1.5 nrad, where the uncertainty comes from the mesh-size dependence of the thermodynamical simulation and the uncertainty on the X-ray flux (up to ±1.3%). The shift of the Bragg angle reduces the efficiency of the conversion and re-conversion, P^2, and the conversion efficiency, ϵ_S, is $84.5 \pm 0.4\%$. The uncertainty on $g_{a\gamma\gamma} \propto (\epsilon_S)^{-\frac{1}{4}}$ is estimated to be ±0.26%.

The Borrmann effect of sub peak: $L_{\rm eff}$

The X-ray attenuation length is affected by X-ray diffraction causing the sub peak (Borrmann effect). The effect can be evaluated by the reduction of the PIN output around the sub peak or later shown in Figs. 4.1. The reduction of the output and the attenuation length is estimated to be 4.9% (19500 pulses$< \Delta\theta <$22000 pulses) and 1.8% ($\Delta\theta >$22000 pulses). The effect reduces the sensitivity to $g_{a\gamma\gamma} \propto (L_{\rm eff})^{-\frac{3}{4}}$ by 0% ($\Delta\theta <$19500 pulses), 3.7% (19500 pulses$< \Delta\theta <$22000 pulses) and 1.4% ($\Delta\theta >$22000 pulses).

4.3.2 Final result

The uncertainties shown above are conservatively taken into account by shifting parameters by 1σ in the direction deteriorating the experimental sensitivity to $g_{a\gamma\gamma}$ and m_a. The obtained upper limit with 90% confidence level is shown in Fig. 4.11. The fluctuation of the upper limit on $g_{a\gamma\gamma}$ comes mainly from the integrated number of detected X rays, N_i^s. The experiment is insensitive to ALPs with a mass close to the plasma frequency of the silicon crystal, $m_\gamma \sim 31$ eV.

The obtained upper limit is represented by the highest upper limits in the mass range of $m_a < m_\gamma$ and $m_a > m_\gamma$ as follows,

$$g_{a\gamma\gamma} < 4.2 \times 10^{-3}\ \text{GeV}^{-1}\ (m_a < 10\ \text{eV}), \tag{4.5}$$

$$g_{a\gamma\gamma} < 5.0 \times 10^{-3}\ \text{GeV}^{-1}\ (46\ \text{eV} < m_a < 1020\ \text{eV}). \tag{4.6}$$

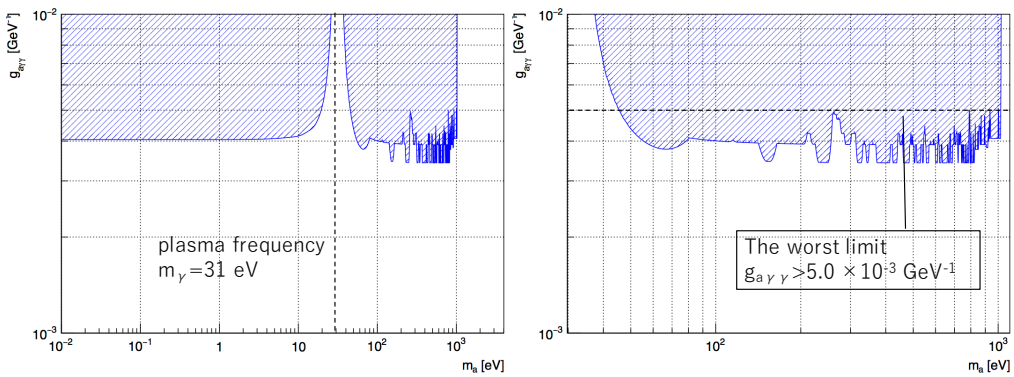

Figure 4.11: The obtained upper limit taking into account systematic uncertainties. The blue area is excluded by the experiment with a 90% confidence level. Left: the whole exclusion region. Right: the magnified view of the exclusion region higher than the plasma frequency.

Chapter 5

Discussion and prospect

The result shown in the previous chapter will be discussed firstly in this chapter. And then an upgrade for future experiments with higher sensitivity will be shown finally.

5.1 Significance of the experimental result

The upper limit obtained by this experiment is compared with previous laboratorial experiments as shown in Fig. 5.1. The figure shows the upper limits obtained by this experiment, a LSW experiment (ALPS) [70], X-ray LSW experiments [97,98], a LSW experiment using a neutrino beamline (NOMAD) [69] and a BMV experiment (PVLAS) [72]. Other laboratorial experiments are omitted since they are more insensitive to ALPs with a mass of 10^{-2} eV $< m_a$. The previous LSW experiments have resonant ALPs' masses of $m_a < \mathcal{O}(1)$ meV (ALPS), $m_a < \mathcal{O}(10^{-1})$ eV (X-ray LSW) and $m_a < 40$ eV (X-ray LSW). Their sensitivity to heavier ALPs are strongly reduced and less reliable due to the rapid oscillation of the conversion probability. This experiment provides the first reliable upper limits on ALPs with a mass up to 1 keV, which is $10^{2\sim3}$ orders of magnitude higher than previous LSW experiments. PVLAS experiment is sensitive to the inclusive contribution of ALPs to photon-photon interaction (box diagram). The resonant mass of the contribution is 1 meV, and sensitivities away from the resonance are also reduced and fluctuate. The sensitivity of this experiment exceeds that of PVLAS experiment in a mass range of $m_a > m_\gamma \sim 30$ eV.

This experiment imposed the most stringent and rigid upper limit on heaviest ALPs up to the sub-keV range as a laboratorial experiment. On the contrary to the axion, ALPs have no theoretical restriction on the relation between ALPs' mass, m_a, and the ALPs-photon coupling constant, $g_{a\gamma\gamma}$. The whole parameter space of m_a and $g_{a\gamma\gamma}$ is the target of ALPs searches. The experiment is scientifically important in that it searched the new parameter region of ALPs.

Although the exclusion region of this experiment is previously searched by helioscope experiments with an upper limit of $g_{a\gamma\gamma} \sim 10^{-9}$ GeV^{-1}, these previous ex-

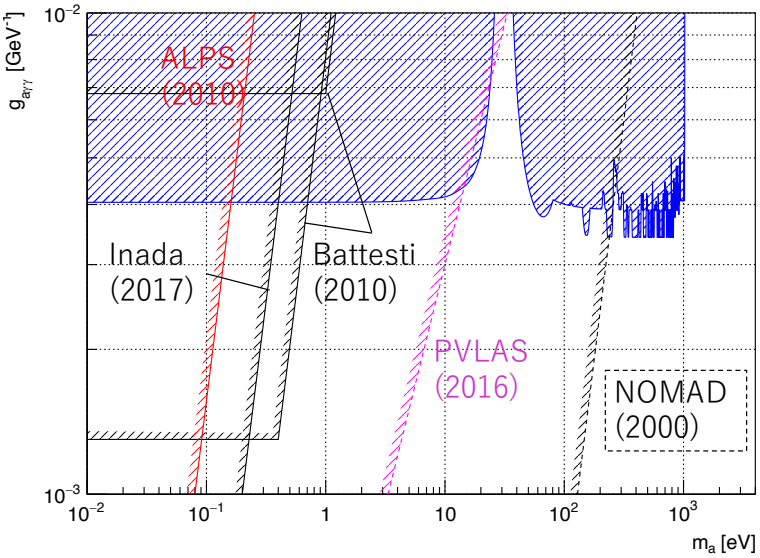

Figure 5.1: The comparison between the obtained limit and previous laboratorial experiments. The upper limits obtained by previous experiments are shown by black solid lines, the red solid line, the purple dotted line and the black dotted line. The figure shows only laboratorial experiments sensitive to ALPs with $m_a > 10^{-2}$ eV. ALPS experiment [70] is an optical LSW experiment (the red solid line). The block solid lines shows X-ray LSW experiments conducted by Battesti (2010) [97] and Inada (2017) [98]. PVLAS experiment [72] is a VMB experiment (the purple dotted line). NOMAD experiment [69] uses high energy photons from a neutrino beam line (the black dotted line).

periments are inevitably model-dependent. The upper limit obtained by helioscope experiments can be relaxed by possible reduction effects such as ALPs mass and couplings dependent on environmental parameters in the sun [78]. These helioscope experiments additionally require that solar axions can actually escape from the sun. The ALPs mean free path within the sun is estimated to be $\sim \left(\frac{g_{a\gamma\gamma}}{9\times10^{-4}\mathrm{GeV}^{-1}}\right)^{-2} R_\odot$, where $R_\odot$ is the solar radius [75]. Solar axions can evade the detection of these helioscope experiments with the sensitivity of $g_{a\gamma\gamma} > 1\times10^{-9}$ GeV^{-1} if the coupling constant $g_{a\gamma\gamma}$ has a value larger than $\sim 5\times10^{-3}$ GeV^{-1}. The obtained result can complement solar axion searches by excluding the evasion in the mass range up to 1 keV.

String theories predict multiple ALPs related to the compactification of the extra dimensions, which may include members within the sub-keV range. One viable candidate for such string ALPs is solar Kaluza-Klein axion, which is astronomically motivated to explain anomalies such as anomalous heating of the solar corona and stellar coronae [44]. The model assumes that string-motivated ALPs have members with sub-keV and keV-range masses and that solar ALPs are gravitationally trapped by the sun itself. These ALPs revolving around the sun decay to two photons and act as an X-ray source located between the sun and the earth. The benchmark coupling strength for the model is suggested to be $g_{a\gamma\gamma} = 9.2\times10^{-14}$ GeV^{-1} with two total extra dimensions, $\delta = 2$, $M_F = 100$ TeV and $R = 10^3$ keV^{-1}. The Kaluza-Klein axion has been previously searched by measuring decay products of ALPs around the earth with the XMASS-I detector [118]. The search imposed an 90% C. L. upper limit of 4.8×10^{-12} GeV^{-1} for a mean ALPs number density of $\bar{n}_a = 4.07\times10^{13}$ m^{-3}.

The upper limit obtained by this experiment becomes to $g_{a\gamma\gamma} \lesssim 10^{-4}$ GeV^{-1} for the benchmark model since the model has $\sim 3\times10^6$ excitations with a mass of $m_a < 1$ keV, which enhances the conversion probability, P^2. Although the upper limit is the first laboratorial one for Kaluza-Klein axions within the sub-keV range, this upper limit is much higher than the benchmark coupling strength and the upper limit obtained by the XMASS-I detector. The contribution from the Kaluza-Klein axion is proportional to the factor of $R_a \propto g_{a\gamma\gamma}^2 R^\delta$, where R_a represents the production rate of the gravitationally trapped solar ALPs. The strong coupling region excluded by this experiment contradicts SSM and the X-ray luminosity of the quiet sun in the benchmark model. However, there are possibility that the production rate, R_a, is reduced by other exotic effects within the sun [78].

5.2 Upgrade for future experiments

The new conversion scheme for a LSW experiment is proposed and performed by this thesis. The feasibility to convert and reconvert ALPs by atomic electric fields in a single crystal is theoretically and experimentally verified. This experimental scheme enables the first LSW experiment scanning the resonant ALPs' mass continuously.

Although this experiment imposes the first rigid upper limit on the sub-keV ALPs, the sensitivity to the coupling constant, $g_{a\gamma\gamma}$, is weaker than previous LSW experiments. It is mainly because the effective conversion length is limited by X-ray absorption within the conversion crystal. An upgrade for future experiments will be discussed in this section.

The experimental sensitivity of the conversion scheme is almost determined by the properties of conversion crystals. The sensitivity to $g_{a\gamma\gamma}$ depends strongly on the effective electric fields, E_T, and the effective conversion length, $L_{\rm eff}$. The resonant ALP's mass, m_a, is proportional to the root of the reciprocal lattice spacing, q_T, and the photon energy of X rays, k_γ. The experimental sensitivity can be enhanced by replacing the silicon channel-cut crystal with a more suitable one. The attenuation length and resonant ALPs' mass can be further enhanced by using X rays with a higher photon energy.

parameter	Si 17 keV	C(diamond) 26 keV	sensitivity enhancement $g_{a\gamma\gamma}$
E_T [10^{10} V/m]	4.4	6.8	1.5
$L_{\rm att}$ [mm]	0.65	32.2	50
$\Delta\theta_{\rm CV}$ [nrad]	204	2.5	0.33
N_γ [10^{13} Hz]	2.5	1	0.80
k_γ [keV]	17	26	1.1
q_T [keV]	6.46	9.85	1.1
Overall			24

Table 5.1: Summary of the sensitivity enhancement when two 32 mm-thick C(220) crystals and X rays with a photon energy of 26 keV are used.

Diamond(C) is the most suitable crystal for the conversion scheme because they have a longer attenuation length, higher effective electric fields and the sensitivity to heavier ALPs than silicon crystals. Figure 5.2 and Tab. 5.1 shows the sensitivity of a LSW experiment using two 32 mm-thick C(220) crystals and X rays with a photon energy of 26 keV. It is assumed in this figure that the detuning angle is scanned up to $\Delta\theta$ =2.0 mrad (m_a = 1 keV) with the same condition as this experiment and that no background X rays are observed. The effective electric field and the effective conversion length are enhanced from this experiment by 1.5 and 50, respectively. On the contrary, the acceptable angular divergence, $\Delta\theta_{\rm CV}$, is reduced from 204 nrad to 2.5 nrad. The X-ray flux of 26-keV X rays is $\sim 1\times10^{13}$ Hz for BL19LXU (the third harmonics). The detuning angle required to convert massive ALPs is reduced by a factor of 2.3 since the setup has higher k_γ and q_T. It enhances the effective DAQ time and the sensitivity to $g_{a\gamma\gamma}$. The sensitivity to $g_{a\gamma\gamma}$ can be enhanced by 24, which exceeds that of previous LSW experiments using X rays and NOMAD experiment.

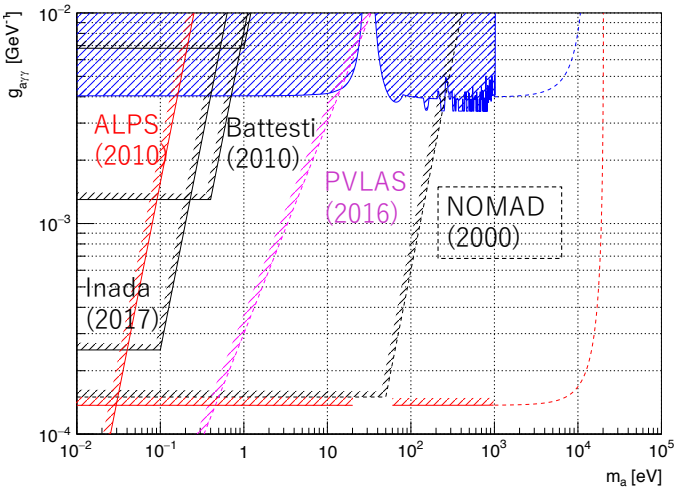

Figure 5.2: The expected sensitivity of future LSW experiments. The red solid line shows the sensitivity of an experiment with two 32 mm-thick C(220) crystals and 26-keV X rays. The experiment is insensitive to the mass region close to the plasma frequency (38 eV). The other conditions are the same condition as this experiment. The dotted lines show the experimental sensitivity to ALPs heavier than 1 keV.

A search for keV-range ALPs

The scanning range is now set to $m_a < 1$ keV for higher sensitivity to $g_{a\gamma\gamma}$. A search for keV-range ALPs with a mass up to ~ 10 keV is also available by lengthening the detuning angle. There are also specific motivations for keV-range ALPs as with sub-keV ones. String theories may have ALPs with a mass of $m_a = 1 \sim 10$ keV in the same way as ones within the sub-keV range. They can provide possible explanation for heat transport under solar corona (m_a ∼few keV), the soft X-ray excess phenomena [119–123] ($m_a \sim 2$ keV) and an unidentified 3.55 keV X-ray emission line recently observed in galaxy clusters [124] ($m_a \sim 7.1$ keV).

The conversion scheme also has the sensitivity to keV-range ALPs as shown by the dotted lines in Fig. 5.2. The scanning range of the detuning angle has to be widened by 100 to search ALPs with a mass of ∼10 keV. A 200-days beam time is required to realize the sensitivity shown by the dotted line. The sensitivity to $g_{a\gamma\gamma}$ is reduced by a factor of 3.2 when the overall DAQ time is the same as this experiment. The setup of the future experiment is also suitable to the search for keV-range ALPs since it has higher reciprocal lattice spacing, X-ray energy and relative sensitivity to $m_a = 10$ keV compared to the current experimental setup.

5.2.1 Requirement for the future experiment

The acceptable angular divergence of the conversion, $\Delta\theta_{\rm CV}$, is inversely proportional to the effective conversion length. Future experiments using diamond crystals require a more stringent condition on the angular alignment of the converter and the re-converter. The required angular precision for 32 mm-thick diamond crystals is $\Delta\theta_{\rm CV} = 2.5$ nrad. As opposed to silicon crystals, the lattice planes of diamond crystals are not sensitive to the X-ray heat load since the diamond crystals have much better thermal conductivity, lower thermal expansion coefficient and longer X-ray attenuation length. However, channel-cut crystals made of diamond are not available since the size of perfect diamond crystals is currently limited to $\mathcal{O}(1 \sim 10)$ mm. It is required to guarantee the parallelism between independent crystals in order to perform the LSW experiments using diamond crystals,

It is quite difficult to measure experimentally the angular parallelism among lattice planes with the precision of $\mathcal{O}$(nrad). One of the solutions for the problem is the measurement of a rocking curve with π-polarized X rays as shown in Fig. 5.3. When injected X rays are π-polarized, the acceptable angular divergence of X-ray diffraction is reduced by a polarization factor, $|P|$, defined as follows,

$$P = (\epsilon_0 \cdot \epsilon_s)^2 = (\cos 2\theta_{\rm B})^2, \tag{5.1}$$

where ϵ_0 and $\epsilon_{\mathbf{s}}$ are the polarization vector of injected X rays and diffracted X rays, respectively. The acceptable bandwidth can be reduced to as much as $\Delta\theta_{\rm CV} = 1$ nrad when the Bragg angle is close to 45 deg. The crystals are fixed to an external jag after the rocking-curve measurement in order to preserve the parallelism between crystals, and then they are rotated by 90 deg to the σ-polarization setup. One of the most suitable adhesive for the purpose is beeswax widely used in X-ray diffractometry. The beeswax has small thermal expansion coefficient, and it can be easily attached and detached only by heating.

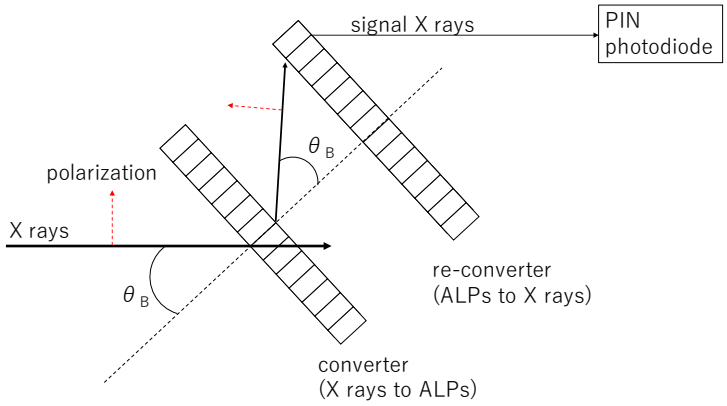

Figure 5.3: The rocking-curve measurement with π-polarized X rays. X rays with π-polarization are reflected two times by the converter and the re-converter. The polarization factor, $|P|$, reduces significantly the acceptable angular divergence of X-ray diffraction when the Bragg angle is close to 45 deg.

Chapter 6

conclusion

The thesis proposed and performed a LSW search for Axion Like Particles (ALPs) using the Laue-case conversion within a single crystal. The conversion scheme enables the first LSW experiment scanning the ALP's mass continuously. A novel X ray-ALP conversion system is developed by using a Si(220) Laue-case channel-cut crystal. The crystal converts and re-converts ALPs whose resonant mass depends on the X-ray injection angle. The experiment is performed at BL19LXU beam line of SPring-8 during the beam time from 2017/10/01 to 10/05 (96 hours).

The signal X rays reconverted from ALPs are measured by scanning the X-ray injection angle from the Bragg angle $\theta_{\rm B}$ to $\theta_{\rm B}+4.62$ mrad. No significant signals are observed, and the obtained upper limit on the ALPs-two photon coupling constant (90% C. L.) is represented as follows,

$$g_{a\gamma\gamma} < 4.2 \times 10^{-3}\ {\rm GeV}^{-1}\ (m_a < 10\ {\rm eV}), \tag{6.1}$$

$$g_{a\gamma\gamma} < 5.0 \times 10^{-3}\ {\rm GeV}^{-1}\ (46\ {\rm eV} < m_a < 1020\ {\rm eV}). \tag{6.2}$$

This limit is the most stringent and most rigid limit on ALPs around the sub-keV region (up to 1 keV) as a model-independent laboratorial search. The sensitivity to m_a and $g_{a\gamma\gamma}$ can be improved by future experiments using diamond crystals and higher-energy X rays.

Appendix A

Theoretical background

This section shows the first theoretical calculation considering the Laue-case conversion with reflecting lattice planes perpendicular to the crystal surfaces. The conversion probability is deduced by using the Darwin dynamical theory of X-ray diffraction. The theory divides all atoms in crystals into arbitral scattering planes. The conversion probability can be obtained by solving recurrence formulae between scattering amplitudes of X rays and ALPs on the planes.

A brief introduction to X-ray diffraction will be given firstly in this chapter. The conversion probability will be calculated in a phased manner secondly, and the discussion about its properties will be provided finally. The main part of the calculation in this chapter is cited from Ref. [1].

A.1 Introduction to theories of X-ray diffraction

There are two ways of treatment for describing the interaction between X rays and crystals: the kinematical theory and the dynamical theory of X-ray diffraction. X rays are coherently reflected by the lattice planes when incident X rays fall on a crystal under the Bragg angle. The reflected X rays can be subsequently reflected to the direction of the primary beam by the same lattice planes. Since the reflection amplitude of individual lattice planes is small, the re-reflection can occur only when the crystal structure is thick enough. The region where scattered X rays can interfere coherently is so small for imperfect crystals that the re-reflection contribution can be neglected as shown in Fig. A.1 (a). The kind of the treatment ignoring the re-reflection is called as the kinematical theory. The kinematical theory holds for X-ray diffraction in usual crystalline materials. On the contrary, the approximation neglecting the re-reflection can be allowed no longer when the crystal is perfect. The treatment considering the multiple reflection as shown in Fig. A.1 (b) is referred to as the dynamical theory.

The Laue-case conversion between X rays and ALPs in crystals is a phenomenon similar to X-ray diffraction. However, the conversion has been considered only by ignoring X-ray diffraction and absorption in Ref. [100]. The first calculation of the

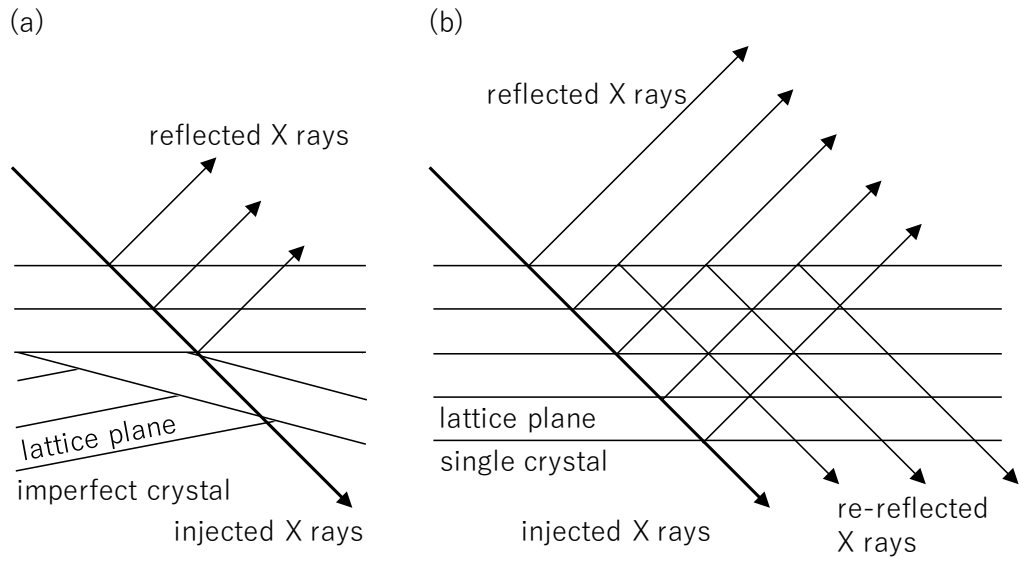

Figure A.1: Schematics of X-ray diffraction. (a): The kinematic theory of X-ray diffraction. The treatment is valid for imperfect crystals. (b): The dynamical theory of X-ray diffraction. It is valid for single crystals.

conversion will be provided in the following sections by using the Darwin dynamical theory of X-ray diffraction. The calculation utilizes both of the two treatments, the kinematical and dynamical theories, to deduce the conversion probability of the conversion. While the dynamical theory is used to describe the interaction between X rays and atoms in crystals, the conversion between X rays and ALPs are dealt with by the kinematical theory since the mixing interaction between X rays and ALPs is so weak that multiple conversion in crystals cannot occur.

A.2 Theoretical calculation of Laue-case conversion

The calculation of the conversion probability is performed by a stepwise manner: the conversion by an atom firstly, the conversion by a virtual 'scattering plane' perpendicular to the lattice planes secondly and the conversion by the whole crystal finally.

A.2.1 Conversion by an atom

The coherent conversion in crystals originates from Primakoff effect in intense electric fields of an atom. The electric fields can be described as $\mathbf{E} = -\nabla\phi$, where ϕ is the electric potential of the atomic electric field. Fig. A.2 shows the schematics of the conversion caused by the atom.

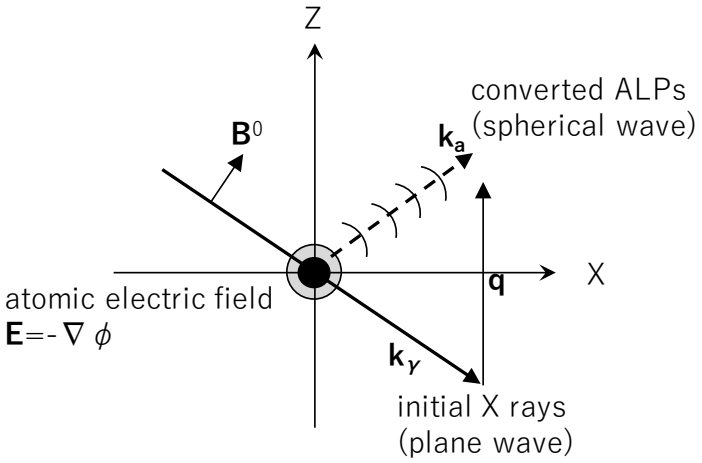

Figure A.2: Schematics of X ray-ALP conversion mediated by an atom. The electric field of an atom, $\mathbf{E}$, converts X-ray plane waves with the momentum of $\mathbf{k}_\gamma$ into ALPs spherical waves with $\mathbf{k}_a$. The momentum transfer, $\mathbf{q}$, is defined as $\mathbf{q} \equiv \mathbf{k}_a - \mathbf{k}_\gamma$.

The conversion process can be described by the following Euler-Lagrange equations,

$$(\Box^2 + m_a^2)a = -g_{a\gamma\gamma}\mathbf{E}\cdot\mathbf{B}, \tag{A.1}$$

$$\nabla\times\mathbf{B} - \frac{\partial}{\partial t}\mathbf{E} = -g_{a\gamma\gamma}\left(\mathbf{B}\frac{\partial}{\partial t} - \mathbf{E}\times\nabla a\right), \tag{A.2}$$

$$\nabla\cdot\mathbf{E} = g_{a\gamma\gamma}\mathbf{B}\cdot\nabla a, \tag{A.3}$$

where $\mathbf{B}$ is the magnetic field of X rays. When the incoming X rays is plane waves, the magnetic field can be rewritten to be

$$\mathbf{B}(t,\mathbf{x}) = \mathbf{B}^0\exp[i(\omega t - \mathbf{k}_\gamma\cdot\mathbf{x})], \tag{A.4}$$

where $\mathbf{B}^0$ is the amplitude of the magnetic field and $\omega, \mathbf{k}_\gamma$ are the energy and the wavenumber of X rays, respectively. Atomic electric field, $\mathbf{E}$, converts the incident X rays into ALPs spherical wave. The amplitude of the converted ALPs can be calculated from Eq. (A.1, A.2, A.3) as follows [99],

$$\dot{a}(t,\mathbf{x}) \equiv \frac{\partial}{\partial t}a(t,\mathbf{x}) = \frac{g_{a\gamma\gamma}F_a(\mathbf{q})}{4\pi}\hat{\mathbf{k}}_a\cdot\mathbf{B}^0\frac{1}{r}\exp[i(\omega t - \mathbf{k}_a\cdot\mathbf{x})], \tag{A.5}$$

$$F_a(\mathbf{q}) = {k_a}^2\int d^3\mathbf{x}\phi(\mathbf{x})\exp(i\mathbf{q}\cdot\mathbf{x}), \tag{A.6}$$

where $\mathbf{k}_a$ is the wavenumber of converted ALPs, $k_a \equiv |\mathbf{k}_a|$ is its norm and $\mathbf{q} \equiv \mathbf{k}_a - \mathbf{k}_\gamma$ is the momentum transfer of the conversion. The form factor, $F_a(\mathbf{q})$, is analogous to the atomic structure factor of X-ray scattering,

$$F_\gamma(\mathbf{q}) = \frac{1}{e}\int d^3\mathbf{x}\rho(\mathbf{x})\exp(i\mathbf{q}\cdot\mathbf{x}), \tag{A.7}$$

where e is the elementary electric charge and $\rho(\mathbf{x})$ is the atomic electron charge density. These form factors have the following relation,

$$F_a(\mathbf{q}) = \frac{e{k_a}^2}{q^2}[Z - F_\gamma(\mathbf{q})], \tag{A.8}$$

where $q \equiv |\mathbf{q}|$ and Z is the atomic number of the crystal. The forward conversion form factor, $F_a(\mathbf{0})$, vanishes from the relation and $F_\gamma(\mathbf{0}) = Z$.

The inverse process can be calculated by the same way from Eq. (A.1, A.2, A.3), [99]

$$\mathbf{B}(t, \mathbf{x}) = -\frac{g_{a\gamma\gamma}F_a(\mathbf{q})}{4\pi}\hat{\mathbf{k}}_\gamma \times (\hat{\mathbf{k}}_\gamma \times \hat{\mathbf{k}}_a)\dot{a}^0\frac{1}{r}\exp[i(\omega t - \mathbf{k}_\gamma \cdot \mathbf{x})]. \tag{A.9}$$

The X ray-ALP conversion occur only when the magnetic field, $\mathbf{B}^0$, is parallel to the conversion plane (σ polarization) due to the factors of $\mathbf{k}_a \cdot \mathbf{B}^0$ and $\hat{\mathbf{k}}_\gamma \times (\hat{\mathbf{k}}_\gamma \times \hat{\mathbf{k}}_a)$. These factors for σ-polarized X rays are reduced to $\sin\theta_s$, where θ_s is the angle between $\mathbf{k}_\gamma$ and $\mathbf{k}_a$.

A.2.2 Conversion by atoms on a virtual scattering plane

The conversion crystal is assumed to be composed of virtual 'scattering planes' perpendicular to the lattice planes for the convenience of the calculation. The scattering planes include all atoms in the crystal. The amplitude from the scattering plane will be deduced in this subsection. The scattering planes mediate X ray-ALP conversion and X-ray scattering. The scattering planes are defined as shown in Fig. A.3.

The conversion and X-ray diffraction take place on the X-Z plane, the lattice planes are parallel to the X-Y plane and the scattering plane is defined as the Y-Z plane in this schematics. The X-ray polarization is parallel to the Y axis (σ-polarization). The position of atoms on the scattering plane is defined as $(0, \tau, \epsilon)$, where $\epsilon = nd_{hkl}$ is the Z position of lattice planes and n is an integer. Incident waves (X rays or ALPs) from the point S are scattered or converted by the scattering plane towards the point P. When X-ray diffraction and X ray-ALP conversion in single crystals are considered, the distance $\overline{SO} \equiv R$ can be assumed to be much longer than $\overline{OP} \equiv r$. The angle of incident and outgoing waves to the X-Y plane are defined as θ_T and θ_S, respectively.

The scattering amplitude by an atom located at $(0, \tau, \epsilon)$ can be obtained from Eq. (A.5, A.9),

$$dS_p = -P_O\frac{g_{a\gamma\gamma}F_a(\mathbf{q})}{4\pi r_{\tau\epsilon}}\sin(\theta_T + \theta_S)\exp\left[\frac{2\pi i}{\lambda_T}(ct_T - R_{\tau\epsilon}) + \frac{2\pi i}{\lambda_S}(ct_S - r_{\tau\epsilon})\right]Md\tau d\epsilon, \tag{A.10}$$

where P_O is the amplitude of incident waves at O, M is the atomic density on the scattering planes, $R_{\tau\epsilon}/r_{\epsilon\eta}$ are the distance between $(0, \tau, \epsilon)$ and S/P, $t_{T,S}$ and $\lambda_{T,S}$ are the propagating time and the wavelengths of incident and outgoing waves. The

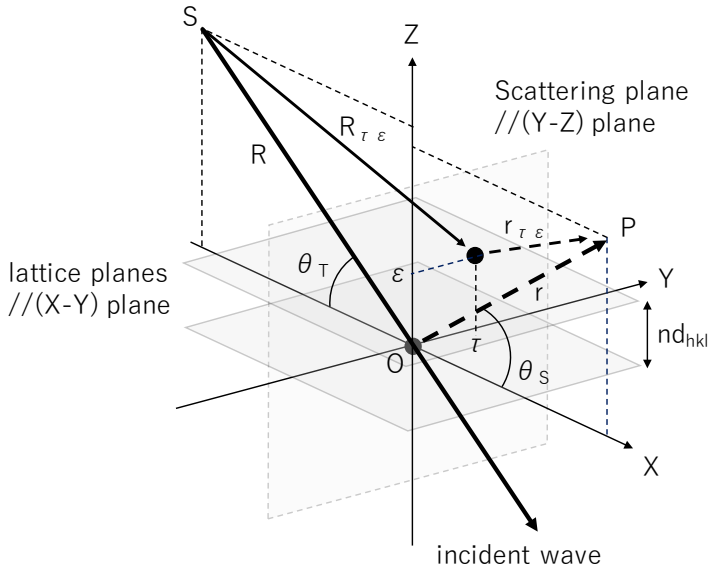

Figure A.3: Schematics of the conversion by a virtual scattering plane. The lattice planes of the crystal is parallel to the X-Y plane, the conversion occurs on the X-Z plane and scattering planes are parallel to the Y-Z plane and crystal surfaces. X rays are assumed to be σ-polarized.

phase of the amplitude does not affect the conversion probability. The phase is taken to be the same as X-ray scattering for later convenience.

The phase factor can be simplified from the relations, $R \gg r$ and $\tau, \epsilon \ll 1$, to be

$$2\pi i \left[\epsilon \left(\frac{\sin\theta_T}{\lambda_T} + \frac{\sin\theta_S}{\lambda_S} \right) - \frac{\epsilon^2 \cos^2\theta_S^2 + \tau^2}{2r\lambda_S} \right], \tag{A.11}$$

by ignoring terms higher than $\mathcal{O}(\epsilon^2, \eta^2)$ and terms proportional to R^{-1}. The coefficient of the first term, ϵ, is subject to the relation $\epsilon = nd_{hkl}$ due to the periodicity of lattice planes. The amplitudes from atoms on the scattering plane can interfere constructively with each other only when the following Fresnel condition satisfies,

$$k_T \sin\theta_T + k_S \sin\theta_S = q_T, \tag{A.12}$$

where $k_{T/S}$ are the wavenumber of the incident/outgoing waves and $q_T = \frac{2\pi}{d_{hkl}}$ is the reciprocal lattice spacing. This relation is equivalent to the momentum transfer of $\mathbf{q} = q_T \hat{\mathbf{z}}$.

The integrated amplitude at P can be calculated by approximating the summation of atoms as continuous integrals and using mean values of $\theta_{T,S}, t_{T,S}, r$ and

$F_a(\mathbf{q})$,

$$\begin{aligned} S_p &= -P_O \frac{g_{a\gamma\gamma} F_a(\mathbf{q})}{4\pi r} M \sin(\theta_T + \theta_S) \exp\left[2\pi i \left(\frac{ct_T - R}{\lambda_T} + \frac{ct_S - r}{\lambda_S}\right)\right] \\ &\quad \times \int\int \exp\left[-2\pi i \left(\frac{\epsilon^2 \cos\theta_S + \tau^2}{2r\lambda_S}\right)\right] d\tau d\epsilon, \end{aligned} \tag{A.13}$$

The double integral is reduced to the well-know Fresnel integrals as follows,

$$\int\int = \frac{r\lambda_S}{2\cos\theta_S}(1-i)^2 = -i\frac{r\lambda_S}{\cos\theta_S}. \tag{A.14}$$

The scattering amplitude by the scattering plane can be rewritten as follows,

$$S_P = P_O(i\zeta)\exp\left[2\pi i\left(\frac{ct_T - R}{\lambda_T} + \frac{ct_S - r}{\lambda_S}\right)\right], \tag{A.15}$$

$$\zeta = \frac{g_{a\gamma\gamma} M \lambda_S F_a(\mathbf{q})}{4\pi\cos\theta_S} \sin(\theta_T + \theta_S). \tag{A.16}$$

This result is completely analogous to X-ray scattering. The X-ray scattering amplitude by the scattering plane can be obtained by the following replacement,

$$\frac{g_{a\gamma\gamma}}{4\pi}\sin(\theta_T + \theta_S) \rightarrow r_e, \tag{A.17}$$

$$F_a(\mathbf{q}) \rightarrow F_\gamma(\mathbf{q}), \tag{A.18}$$

where r_e is the classical electron radius.

A.2.3 Conversion probability by the whole crystal

The conversion probability by the whole crystal will be calculated in this subsection. The following geometry is assumed for the convenience of the calculation: the crystal surfaces are parallel to the Y-Z plane and lattice planes are parallel to the X-Y plane. The geometry in which lattice planes are perpendicular to the surface is referred to as the Laue case. All atoms in the crystal are divided into scattering planes parallel to crystal surfaces as shown in Fig. A.4. The spacing and the number of scattering planes, r and N, are dummy variables subject to the relation $rN = H$, where H is the thickness of the crystal. These dummy variables will be excluded in the final phase of the calculation.

When incident X rays or ALPs fall on the crystal, X ray-ALPs conversion and X-ray diffraction in the crystal produce the following four waves: transmitted X rays T^γ, reflected X rays S^γ, transmitted ALPs T^a and reflected ALPs S^a. The angle between these waves and the lattice planes are defined as $\theta^{\gamma/a}_{T/S}$, respectively. These angles should obey the Fresnel condition from Eq. (A.11),

$$k_\gamma \sin\theta^\gamma_T + k_\gamma \sin\theta^\gamma_S = k_\gamma \sin\theta^\gamma_T + k_a \sin\theta^a_S = k_a \sin\theta^a_T + k_\gamma \sin\theta^\gamma_S = q_T, \tag{A.19}$$

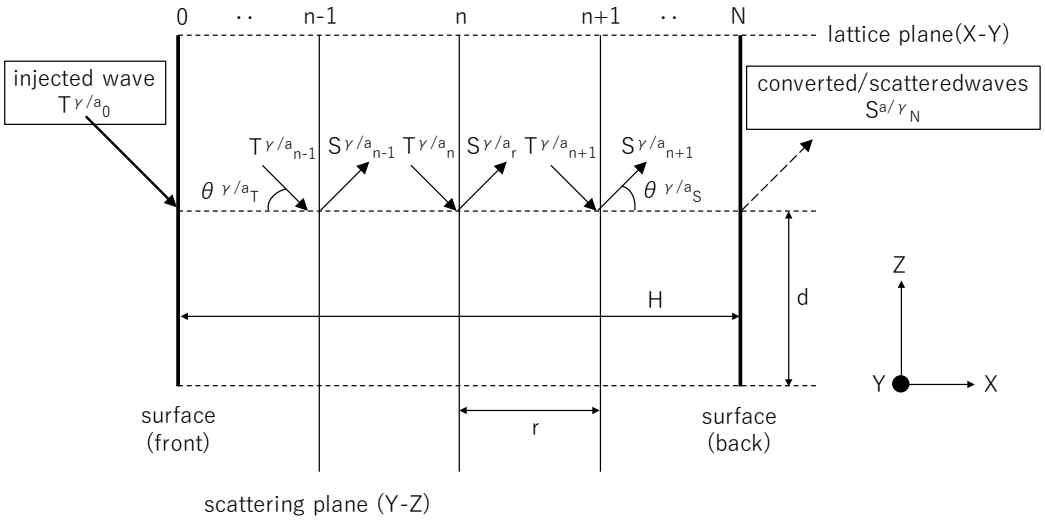

Figure A.4: Schematics of crystal configuration for the Darwin dynamical theory of X-ray diffraction. The figure is cited from Ref. [1]. The whole crystal is divided into scattering planes parallel to crystal surfaces with the spacing of r.

where k_γ is the wavenumber of X rays. The condition determines $\theta_{T/S}^{\gamma/a}$ and the momentum transfer, $\mathbf{q}$, as a function of the injection angle, $\theta_T^{\gamma/a}$. When the incident angle is away from the Bragg angle by $\Delta\theta$, $\theta_T^{\gamma/a} \simeq \theta_{\rm B} + \Delta\theta$ and $\theta_S^{\gamma/a} \simeq \theta_{\rm B} - \Delta\theta$. The detuning from the Bragg angle provides an additional momentum transfer in the x direction,

$$q_x = \begin{cases} \frac{2q_T(k_\gamma \sin\theta_T^\gamma - \frac{q_T}{2})}{2k_\gamma \cos\theta_T^\gamma} & (T^\gamma \text{ to } S^\gamma,\ \gamma\gamma) \\ -\frac{m_a^2 - 2q_T(k_\gamma \sin\theta_T^\gamma - \frac{q_T}{2})}{2k_\gamma \cos\theta_T^\gamma} & (T^\gamma \text{ to } S^a,\ \gamma a), \end{cases} \tag{A.20}$$

where the approximation, $q_x \ll 1$, is used in the denominators. These momentum transfers are equivalent to the phase change due to the X-ray diffraction and X ray-ALP conversion. Resonant conditions for X-ray diffraction and X ray-ALP conversion are equivalent to the condition, $q_x \simeq 0$. The resonant condition of X ray-ALP conversion can satisfy away from the Bragg condition due to the ALPs mass, m_a.

The Laue-case conversion in the crystal originates from the transition between the four waves. The transition is mediated by X ray-ALP conversion ($T^\gamma \leftrightarrow S^a, T^a \leftrightarrow S^\gamma$), X-ray scattering ($T^\gamma \leftrightarrow S^\gamma$) and forward scattering ($T^\gamma \to T^\gamma$, $S^\gamma \to S^\gamma$) on scattering planes. The scattering amplitudes of these transition are

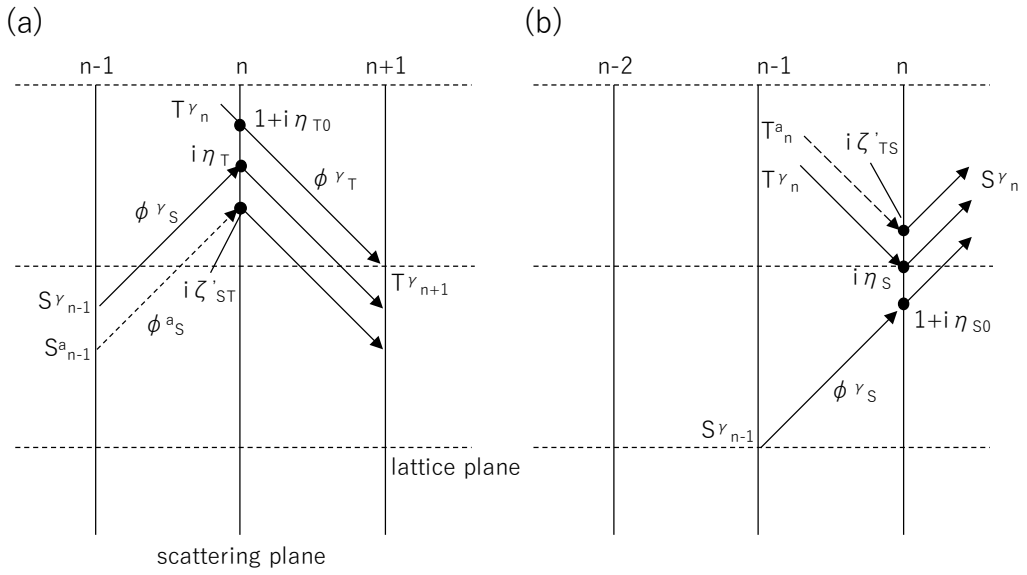

Figure A.5: The transition between X-ray/ALP waves in the crystal. (a) The transition into transmitted X rays, T^{γ}_{n+1}. (b) The transition into reflected X rays, S^{γ}_{n}.

deduced from Eq. (A.16, A.17, A.18) as follows,

$$\eta_i \equiv \eta_i(\mathbf{q}) = \frac{r_e M \lambda_\gamma F_\gamma(\mathbf{q})}{\cos\theta^\gamma_i}, \tag{A.21}$$

$$\eta_{i0} \equiv \eta_i(\mathbf{0}), \tag{A.22}$$

$$\zeta_{jk} = \frac{g_{a\gamma\gamma} M \lambda_a F_a(\mathrm{q})}{4\pi\cos\theta^a_k}\sin(\theta^\gamma_j + \theta^a_k), \tag{A.23}$$

$$\zeta'_{jk} = \frac{g_{a\gamma\gamma} M \lambda_\gamma F_a(\mathrm{q})}{4\pi\cos\theta^\gamma_k}\sin(\theta^a_j + \theta^\gamma_k), \tag{A.24}$$

where the subscripts are $i = (T/S)$, $(j,k) = (T,S)/(S,T)$, η_i is the X-ray scattering amplitude, η_{i0} is the X-ray forward scattering amplitude and ζ_{jk}/ζ'_{jk} are the X ray-ALP/ALP-X ray conversion amplitude. $\lambda_{\gamma/a}$ are the wavelengths of X rays and ALPs. The effective atomic density on the scattering planes, M, is defined as $M = \frac{F_c}{V} r$, where F_c is the coefficient of the crystal structure factor and V is the volume of unit cells.

The transition between four waves can be described by a recurrence relation between their amplitudes at the n^{th} scattering plane, $T^{\gamma/a}_n$ and $S^{\gamma/a}_n$. For example, the transmitted X rays, T^{γ}_{n+1}, is composed of the three components as shown in Fig. A.5 (a): the transmission and the forward scattering from T^{γ}_n, the reflection from S^{γ}_{n-1} and the conversion from S^{a}_{n-1}. In the same way the reflected X rays, S^{γ}_n, is composed of the transmission and the forward scattering of S^{γ}_{n-1}, the reflection

from T_n^γ and the conversion from T_n^a as shown in Fig. A.5 (b). The waves obtain the following phases during the propagation between scattering planes,

$$\phi_{T/S}^{\gamma/a} = k_{\gamma/a} r \cos\theta_{T/S}^{\gamma/a}. \tag{A.25}$$

The amplitudes of ALPs can be obtained in the same way except that ALPs are not scattered by scattering planes. The recurrence relation between X-ray/ALP waves can be deduced from the above discussion as the following formulae,

$$\begin{aligned} T_{n+1}^\gamma &= T_n^\gamma(1+i\eta_{T0})e^{-i\phi_T^\gamma} + S_{n-1}^\gamma(i\eta_T)e^{-i(\phi_S^\gamma+\phi_T^\gamma)} \\ &\quad + S_{n-1}^a(i\zeta'_{ST})e^{-i(\phi_S^a+\phi_T^\gamma)}, \qquad \text{(A.26)} \\ S_n^\gamma &= T_n^\gamma(i\eta_S) + S_{n-1}^\gamma(1+i\eta_{S0})e^{-i\phi_S^\gamma} + T_n^a(i\zeta'_{TS}), \qquad \text{(A.27)} \\ T_{n+1}^a &= T_n^a e^{-i\phi_T^a} + S_{n-1}^\gamma(i\zeta_{ST})e^{-i(\phi_S^\gamma+\phi_T^a)}, \qquad \text{(A.28)} \\ S_n^a &= S_{n-1}^a e^{-i\phi_S^a} + T_n^\gamma(i\zeta_{TS}). \qquad \text{(A.29)} \end{aligned}$$

The conversion probabilities between X rays and ALPs, $P_{\gamma\to a}$ and $P_{a\to\gamma}$, can be calculated by

$$P_{\gamma\to a} = \left|\frac{S_N^a}{T_0}\right|^2 \quad (T_0^\gamma = T_0, T_0^a = 0), \tag{A.30}$$

$$P_{a\to\gamma} = \left|\frac{S_N^\gamma}{T_0}\right|^2 \quad (T_0^\gamma = 0, T_0^a = T_0), \tag{A.31}$$

where T_0 is the amplitude of incident waves.

The conversion probability from X rays into ALPs is calculated firstly with the boundary condition of $T_0^\gamma = T_0$ and $T_0^a = 0$. The amplitudes of ALPs are rewritten by using Eq.(A.28,A.29) as follows,

$$\begin{aligned} T_{n+1}^a &= (i\zeta_{ST})\sum_{k=0}^{n-1} R_k^\gamma e^{-i(\phi_S^\gamma+\phi_T^a(n-k))}, \qquad \text{(A.32)} \\ S_n^a &= (i\zeta_{TS})\sum_{k=0}^{n} T_k^\gamma e^{-i(\phi_S^a(n-k))}. \qquad \text{(A.33)} \end{aligned}$$

The contribution of ALPs waves in Eq.(A.26,A.27) are estimated to be the order of ζ_{ij}^2 from the expression. The re-conversion contribution can be ignored since the X ray-ALP conversion amplitude is considered to be tiny. This approximation is equivalent to the Born approximation. The recurrence relations between X rays, Eq.(A.26,A.27), are reduced to the same one as usual X-ray diffraction in Laue-case crystals by the approximation. The solution of T_n^γ can be obtained by using characteristic functions [125],

$$T_n^\gamma = T_0(C_\alpha x_\alpha^n + C_\beta x_\beta^n). \tag{A.34}$$

The parameters in the solution are defined as follows,

$$C_{\alpha/\beta} \equiv \frac{1}{2}\left[1 \pm \frac{\sin\Delta\phi_\gamma(1+i\eta_0)}{u}\right], \tag{A.35}$$

$$x_{\alpha/\beta} \equiv e^{-\phi_\gamma}[(1+i\eta_0)\cos\Delta\phi_\gamma \mp iu], \tag{A.36}$$

$$u \equiv [\eta^2 + (1+i\eta_0)^2\sin^2\Delta\phi_\gamma]^{\frac{1}{2}}, \tag{A.37}$$

$$\eta \equiv \eta(\mathbf{q}) = \frac{r_e M \lambda_\gamma F_\gamma(\mathbf{q})}{\cos\theta_{\rm B}}, \tag{A.38}$$

$$\eta_0 \equiv \eta(\mathbf{0}), \tag{A.39}$$

$$\phi_\gamma \equiv \frac{1}{2}(\phi_T^\gamma + \phi_S^\gamma), \tag{A.40}$$

$$\Delta\phi_\gamma \equiv \frac{1}{2}(\phi_T^\gamma - \phi_S^\gamma) = -\frac{r}{2}q_{x,\gamma\gamma}, \tag{A.41}$$

where the approximation, $\sqrt{\eta_T\eta_S} \simeq \eta$, $\sqrt{\eta_{T0}\eta_{S0}} \simeq \eta_0$ and $\eta_{T0} + \eta_{S0} \simeq 2\eta_0$, are used. The characteristic functions originate from standing waves caused by X-ray diffraction, which are referred to as the Bloch waves α and β. The amplitude of converted ALPs, S_N^a, can be rewritten by using Eq. (A.33, A.34) as

$$S_N^a = T_0(i\zeta_{TS})e^{-iN\phi_S^a}\sum_{j=\alpha/\beta} C_j \frac{1-(x_j e^{i\phi_S^a})^{N+1}}{1-x_j e^{i\phi_S^a}}. \tag{A.42}$$

The parameters, $\Delta\phi_\gamma, u, \eta$ and η_0, are proportional to the dummy variable, r. The higher order terms of these variables can be ignored by taking $r \to 0$ with the constraint of $rN = H$. The parameters in Eq. (A.42) are reduced by the approximation to

$$C_{\alpha/\beta} = \frac{1}{2}\left(1 \pm \frac{\Delta\phi_\gamma}{u}\right), \tag{A.43}$$

$$x_{\alpha/\beta}e^{i\phi_S^a} = 1 + i(\eta_0 \mp u + \Delta\phi_\gamma - 2\Delta\phi_a), \tag{A.44}$$

$$u = \sqrt{\eta^2 + \Delta\phi_\gamma^2}, \tag{A.45}$$

where the following representation is used,

$$\Delta\phi_a \equiv \frac{1}{2}(\phi_T^\gamma - \phi_S^a) = -\frac{1}{2}q_{x,\gamma a}. \tag{A.46}$$

The phase difference, $\Delta\phi_a$, is directly related to the resonant condition of the X ray-ALP conversion. The conversion amplitude, Eq. (A.42), are finally rewritten by using Eq. (A.43, A.44, A.45) as

$$S_N^a = \frac{T_0}{2}(i\zeta_{TS}N)e^{-N\phi_S^a}\sum_{\pm(\frac{\alpha}{\beta})}\left(1 \pm \frac{\Delta\phi_\gamma}{u}\right)\frac{\exp(i(\eta_0 \mp u + \Delta\phi_\gamma - 2\Delta\phi_a)N)}{(\eta_0 \mp u + \Delta\phi_\gamma - 2\Delta\phi_a)N}, \tag{A.47}$$

where the approximation, $\lim_{x\to 0}(1+x)^{y/x} \simeq e^y$, is used.

In the inverse case with the boundary condition of $T_0^A = T_0$ and $T_0^G = 0$, the amplitude of re-converted X rays, R_N^G, can be also deduced by using the Born approximation. The X-ray amplitude, S_N^γ, can be considered as a superposition of X rays converted from ALPs at $k^{\rm th}$ scattering planes. The solution of S_N^γ is as follows,

$$S_N^\gamma = T_0(i\zeta'_{TS})\sum_{k=0}^{N} e^{-i\phi_T^a}(C_\alpha x_\alpha^{N-k} + C_\beta x_\beta^{N-k}), \tag{A.48}$$

where the following representation is used,

$$\Delta\phi_\gamma \equiv \frac{1}{2}(\phi_S^\gamma - \phi_T^\gamma), \tag{A.49}$$

$$\Delta\phi_a \equiv \frac{1}{2}(\phi_S^\gamma - \phi_T^a). \tag{A.50}$$

The expression is equivalent to Eq. (A.47), except that ζ_{TS} is replaced by ζ'_{TS}.

A.2.4 Expression using macroscopic parameters

The conversion probability is obtained by using microscopic parameters, $\zeta, \zeta', \eta, \eta_0$ and $\Delta\phi_{\gamma/a}$, proportional to r in the above discussion. The macroscopic expression for these parameters are provided for later convenience.

The X ray-ALP conversion amplitudes, ζ and ζ', can be rewritten as follows,

$$\zeta_{jk}^{(\prime)} N = \frac{1}{2} g_{a\gamma\gamma} E_T H D, \tag{A.51}$$

$$E_T \equiv q_T \frac{F_c}{V}\int d^3\mathbf{x}\phi(\mathrm{x})\exp(i\mathbf{q}\cdot\mathbf{x}), \tag{A.52}$$

$$D \equiv \begin{cases} \frac{k_a}{q_T}\frac{\sin(\theta_T^\gamma+\theta_S^a)}{\cos\theta_S^a} & (\gamma\to a) \\ \frac{k_a^2}{k_\gamma q_T}\frac{\sin(\theta_T^a+\theta_S^\gamma)}{\cos\theta_S^\gamma} & (a\to\gamma) \end{cases} \tag{A.53}$$

where E_T is the effective electric field in the crystal. The factor, D, can be reduced to unity under the Bragg condition ($\theta_{T/S}^{\gamma/a} \simeq \theta_{\rm B}$ and $k_\gamma \simeq k_a$).

The X-ray scattering amplitudes, η and η_0, are complex variables whose real and imaginary parts have different physical meanings. The forward scattering amplitude, η_0, is related to the properties of X rays in the crystal. It has the following relation,

$$\mathrm{Re}(\eta_0)N = \frac{m_\gamma^2 L}{2k_\gamma}, \tag{A.54}$$

$$\mathrm{Im}(\eta_0)N = \frac{L}{2L_{\rm att}}, \tag{A.55}$$

where m_γ is the plasma frequency of the crystal, $L = \frac{H}{\cos\theta_{\rm B}}$ is the path length within the crystal and $L_{\rm att}$ is the X-ray attenuation length of the crystal. The contribution

of X-ray scattering amplitude, η, modifies these macroscopic parameters. The modifications can be parametrized as

$$\Delta m_\gamma^2 \equiv m_\gamma^2 \frac{\mathrm{Re}(\eta)}{\mathrm{Re}(\eta_0)}, \tag{A.56}$$

$$\kappa \equiv \frac{\mathrm{Im}(\eta)}{\mathrm{Im}(\eta_0)}. \tag{A.57}$$

The phase difference, $\Delta\phi_{\gamma/a}$, are related to the resonant condition of X-ray diffraction and X ray-ALP conversion. Their macroscopic expression can be described from Eq. (A.20) as follows,

$$\Delta\phi_\gamma N = \frac{H}{4k_\gamma \cos\theta_\mathrm{B}} \left[-2q_T \left(k_\gamma \sin\theta_T^\gamma - \frac{q_T}{2}\right)\right] \simeq -\frac{q_T H}{2}\Delta\theta \tag{A.58}$$

$$\Delta\phi_a N = \frac{L}{4k_\gamma} \left[m_a^2 - 2q_T \left(k_\gamma \sin\theta_T^\gamma - \frac{q_T}{2}\right)\right], \tag{A.59}$$

where $\Delta\theta \equiv \theta_T^\gamma - \theta_B$ is the detuning angle.

A.3 Resonant condition and conversion probabilities

The conversion probability shown by Eq. (A.47) can be enhanced when the conversion amplitude from constituents of the crystal are constructively interfered with each other. The resonant condition of the X ray-ALP conversion is affected by the effect of X-ray diffraction. It is important to note that the resonance condition of the X ray-ALP conversion dose not necessarily require the Bragg condition. The following two cases are considered in this section: the case under the Bragg condition and the case where the X-ray injection angle is far away from the Bragg angle.

Resonance under the Bragg condition

When the Bragg condition is fulfilled ($\Delta\phi_\gamma \simeq 0$), Eq. (A.43, A.45) are reduced to $u \simeq \eta$ and $C_{\alpha/\beta} = \frac{1}{2}$. The conversion probability can be calculated from Eq.(A.47) to be

$$P_{a\leftrightarrow\gamma} = \left|\frac{S_N^a}{T_0}\right|^2 \simeq \frac{1}{4}(\zeta_{TS}N)^2 \left|\sum_{j=\pm(\alpha/\beta)} \frac{1-\exp[i(\eta_0 \mp \eta - 2\Delta\phi_a)N]}{(\eta_0 \mp \eta - 2\Delta\phi_a)N}\right|^2. \tag{A.60}$$

The conversion probability has two maxima corresponding to the Bloch waves under the following condition,

$$\begin{aligned} & \eta_0 \mp \eta - 2\Delta\phi_a = 0 \\ \leftrightarrow \quad & m_a^2 = m_\gamma^2 \mp \Delta m_\gamma^2, \end{aligned} \tag{A.61}$$

where the relations Eq. (A.54,A.56,A.59) are used. Their widths at a half maximum of $(P_{\gamma\leftrightarrow a})^2$ are as follows,

$$\left|m_a^2 - (m_\gamma^2 \mp \Delta m_\gamma^2)\right| < \begin{cases} \frac{4k_\gamma}{L} & L \ll L_{\mathrm{att},\alpha/\beta} \\ \frac{\sqrt{\sqrt{2}-1}k_\gamma}{L_{\mathrm{att},\alpha/\beta}} & L \gg L_{\mathrm{att},\alpha/\beta} \end{cases}. \tag{A.62}$$

The right hand side under the condition, $L \sim L_{\mathrm{att},\alpha/\beta}$, can be approximated to be $\frac{4k_\gamma}{L}$ without a large loss of precision. The conversion probability under the resonant condition, Eq. (2.5), can be deduced by using Eqs. (A.51, A.55, A.57) and approximating $D = 1$.

Resonance far away from the Bragg condition

When the X-ray injection angle is much larger than the Bragg angle ($\theta_T^\gamma \gg \theta_\mathrm{B}$, $|\Delta\phi_\gamma| \gg \eta$ and $u \simeq -\Delta\phi_\gamma$), Eq. (A.43) are reduced to $C_\alpha = 0$ and $C_\beta = 1$. The conversion is mediated only by the Bloch wave β in this case as follows,

$$P_{a\leftrightarrow\gamma} = \left|\frac{S_N^a}{T_0}\right|^2 \simeq \frac{1}{2}(\zeta_{TS}N)^2 \left|\frac{1-\exp[i(\eta_0 - 2\Delta\phi_a)N]}{(\eta_0 - 2\Delta\phi_a)N}\right|^2. \tag{A.63}$$

The conversion probability has its single maxima under the condition

$$\begin{aligned} & \mathrm{Re}(\eta_0) - 2\Delta\phi_a = 0 \\ \leftrightarrow \quad & m_a = \sqrt{m_\gamma^2 + 2q_T\left(k_\gamma \sin\theta_T^\gamma - \frac{q_T}{2}\right)} && \text{(A.64)} \\ & \simeq \sqrt{m_\gamma^2 + 2q_T k_\gamma \cos\theta_\mathrm{B}\Delta\theta} && \text{(A.65)} \end{aligned}$$

where Eq. (A.54, A.59) are used. The width of the resonance at a half maximum of $(P_{\gamma\leftrightarrow a})^2$ is as follows,

$$\left|m_a^2 - m_\gamma^2 - 2q_T\left(k_\gamma \sin\theta_T^\gamma - \frac{q_T}{2}\right)\right| < \begin{cases} \frac{4k_\gamma}{L} & L \ll L_{\mathrm{att},\alpha/\beta} \\ \frac{\sqrt{\sqrt{2}-1}k_\gamma}{L_\mathrm{att}} & L \gg L_\mathrm{att} \end{cases}. \tag{A.66}$$

The right hand side can be approximated as shown in the discussion below Eq. (A.62). The conversion probability under the resonant condition, Eq. (2.7), can be deduced by the same way as Eq. (2.5).

A.4 Crystals suitable for the conversion scheme

The conversion probability depends on the following properties of the crystal: the effective electric field, E_T, the X-ray attenuation length, L_att, and the ratio, κ, defined by Eq. (A.57). These parameters depend strongly on the kinds of crystals. The dependency of these parameters will be discussed in this section. The candidate for the crystals are diamond-like crystals such as C(diamond), Si and Ge crystals. They are widely used in X-ray optics.

Effective electric fields

The effective electric field in crystals, E_T, depends on the Fourier transform of the atomic electric potential as shown in Eq. (A.52). It can be calculated by using the Moliere approximation [126, 127] as follows,

$$E_T = q_T \frac{F_c}{d_0^3} \sum_{i=1}^{3} \frac{Ze\alpha_i}{\beta_i^2 + q_T^2}, \tag{A.67}$$

$$\alpha_{1,2,3} \equiv 0.10,\ 0.55,\ 0.35, \tag{A.68}$$

$$\beta_i \equiv 8.25 \times 10^{-3} Z^{-\frac{1}{3}} b_i m_e, \tag{A.69}$$

$$b_{1,2,3} = 6.0,\ 1.2,\ 0.3, \tag{A.70}$$

where m_e is the electron mass. E_T depends on two parameters: q_T and F_c. They are determined by indexes of reflecting lattice planes. The field is stronger for lattice planes with lower indexes since the electric field is approximately proportional to q_T^{-1}. The factor, F_c, of diamond-like crystals is as follows,

$$F_c = \begin{cases} 8 & (h,k,l \text{ are all odd/even}, h+k+l = 4m) \\ 4\sqrt{2} & (h,k,l \text{ are all odd/even}, h+k+l = 4m \pm 1)\ , \\ 0 & (\text{otherwise}) \end{cases} \tag{A.71}$$

where m is an integer. The factor forbids the conversion by lattice planes such as (110) lattice planes. It is referred to as the extinction rule of X-ray diffraction. The (220) lattice planes are the most suitable ones since the dependency of F_c favors lattice planes with $h + k + l = 4m$.

Attenuation lengths

X rays are absorbed by atoms in crystals when incident or reconverted X rays propagate through the crystal. The photoelectric absorption has the largest cross section in the X-ray region among other interaction between X rays and atoms. The attenuation length and effective conversion length are longer for crystals with lower Z and higher-energy X rays since the cross section of photoelectric absorption has the dependency of $Z^5 k_\gamma^{-\frac{7}{2}}$.

The factor κ

The factor, κ, determines the attenuation length of the Bloch waves under the Bragg condition. The Bormann effect enhances the attenuation length of the Bloch wave α significantly when κ is close to unity. The factor is equivalent to the Debye-Waller factor, e^{-M}, related to the thermal motion of atoms. The Debye-Waller factor can

be calculated as follows,

$$M = B\left(\frac{\sin\theta_{\mathrm{B}}}{\lambda}\right)^2, \tag{A.72}$$

$$B \equiv \frac{6h^2T}{m_{atom}k_B\Theta_D^2}\left[\phi'(x)+\frac{x}{4}\right], \tag{A.73}$$

$$\phi'(x) \equiv \frac{1}{x}\int_0^x \frac{\xi}{e^{\xi}-1}d\xi, \tag{A.74}$$

where h is the plank constant, T is the temperature of the crystal, m_{atom} is the atomic mass, k_B is the Boltzmann constant, Θ_D is the Debye temperature of the crystal and $x \equiv \frac{\Theta_D}{T}$. Hard crystals such as diamonds have higher Debye temperature, smaller M and κ closer to unity.

Summary

The parameters of C(220), Si(220) and Ge(220) crystals are summarized in Tab. 2.1. The X-ray energy is assumed to be 17 keV. The dependency of the attenuation length favors low-Z crystals such as C and Si crystals. The diamond crystals have the most ideal properties with strong electric fields, long attenuation lengths and κ close to unity. On the contrary, Ge crystals are not suitable for the conversion scheme due to its short attenuation length.

A.5 Effect of other lattice planes

There is possibility that the Bragg condition of other lattice planes, $(h'k'l')$, is accidentally satisfied during the scanning of the detuning angle. This section briefly studies the effect of other lattice planes on the experimental sensitivity.

Figure A.6 shows the schematics of the X ray-ALP conversion under the Bragg condition of $(h'k'l')$ lattice planes. X ray diffraction takes place on a plane other than the conversion plane (X-Z plane). It is assumed that the Bragg condition of (hkl) lattice planes is not satisfied. Although the amplitude of converted ALPs can be represented by Eq. (A.33), the amplitude of transmitted X rays is affected by X-ray diffraction of $(h'k'l')$ lattice planes as follows,

$$T_n^{\gamma} = T_0\left[C'_{\alpha}(x'_{\alpha})^n + C'_{\beta}(x'_{\beta})^n\right] \tag{A.75}$$

where the parameters with prime marks represents the $(h'k'l')$ lattice planes' counterpart of parameters in Eq. (A.34). In the same way as the discussion below Eq. (A.34), the amplitude of converted ALPs can be calculated as follows,

$$S_N^a = \frac{T_0}{2}(i\zeta_{TS}N)e^{-N\phi_S^a}\sum_{\pm\left(\frac{\alpha}{\beta}\right)}\left(1\pm\frac{\Delta\phi'_{\gamma}}{u'}\right)\frac{\exp(i(\eta_0\mp u'+\Delta\phi'_{\gamma}-2\Delta\phi_a)N)}{(\eta_0\mp u'+\Delta\phi'_{\gamma}-2\Delta\phi_a)N} \tag{A.76}$$

where the parameters with prime marks represents the $(h'k'l')$ lattice planes' counterpart of parameters in Eq. (A.47). The X-ray forward scattering amplitude η_0' is the same as that of (hkl) lattice planes, η_0. When the Bragg condition of the $(h'k'l')$ lattice planes is exactly satisfied ($\Delta\phi_\gamma' = 0$ and $u' = \eta'$), the conversion probability can be represented as follows,

$$P_{a\leftrightarrow\gamma} = \left|\frac{S_N^a}{T_0}\right|^2 \simeq \frac{1}{4}(\zeta_{TS}N)^2 \left|\sum_{j=\pm(\alpha/\beta)} \frac{1-\exp[i(\eta_0 \mp \eta' - 2\Delta\phi_a)N]}{(\eta_0 \mp \eta' - 2\Delta\phi_a)N}\right|^2 . \quad \text{(A.77)}$$

The conversion probability has two maxima under the following condition,

$$\begin{aligned} & \eta_0 \mp \eta' - 2\Delta\phi_a = 0 \\ \leftrightarrow \quad & m_a = \sqrt{m_\gamma^2 \mp (\Delta m_\gamma^2)' + 2q_T\left(k_\gamma \sin\theta_T^\gamma - \frac{q_T}{2}\right)} \quad \text{(A.78)} \\ & \simeq \sqrt{m_\gamma^2 \mp (\Delta m_\gamma^2)' + 2q_T k_\gamma \cos\theta_{\rm B}\Delta\theta} \quad \text{(A.79)} \end{aligned}$$

X-ray diffraction of $(h'k'l')$ lattice planes provide the additional factor $(\Delta m_\gamma^2)' \sim \Delta m_\gamma^2 = \mathcal{O}(10\text{ eV})$. The shift can be ignored since it is much smaller than that due to an uncertainty on the X-ray injection angle. The sensitivity to ALPs with a mass between these maxima is reduced in the same way as that under the Bragg condition of (hkl) lattice planes. However, the insensitive region is smeared out since the injected beams have an finite angular divergence in the Y direction.

The maximum conversion probability can be calculated in the same way as Eq. (2.5),

$$\begin{aligned} P_{a\leftrightarrow\gamma} &= \left(\frac{1}{4}g_{a\gamma\gamma}E_T L'_{{\rm eff},\alpha/\beta} D\cos\theta_{\rm T}\right)^2 \\ &= 8.6\times10^{-8}\times(D\cos\theta_{\rm T})^2\times\left(\frac{g_{a\gamma\gamma}}{10^{-3}\text{ GeV}^{-1}}\frac{E_T}{10^{11}\text{ V/m}}\frac{L\prime_{\alpha/\beta}}{1\text{ mm}}\right)^2 \quad \text{(A.80)} \\ L'_{\alpha/\beta} &\equiv 2L'_{{\rm att},\alpha/\beta}\left(1-\exp\left(-\frac{L_T}{2L'_{{\rm att},\alpha/\beta}}\right)\right), \quad \text{(A.81)} \end{aligned}$$

where $L'_{{\rm att},\alpha/\beta}$ is the attenuation length of the Bloch waves due to X-ray diffraction of $(h'k'l')$ lattice planes. The Bormann effect of $(h'k'l')$ lattice planes can affect the conversion probability by changing the transmission efficiency of X rays.

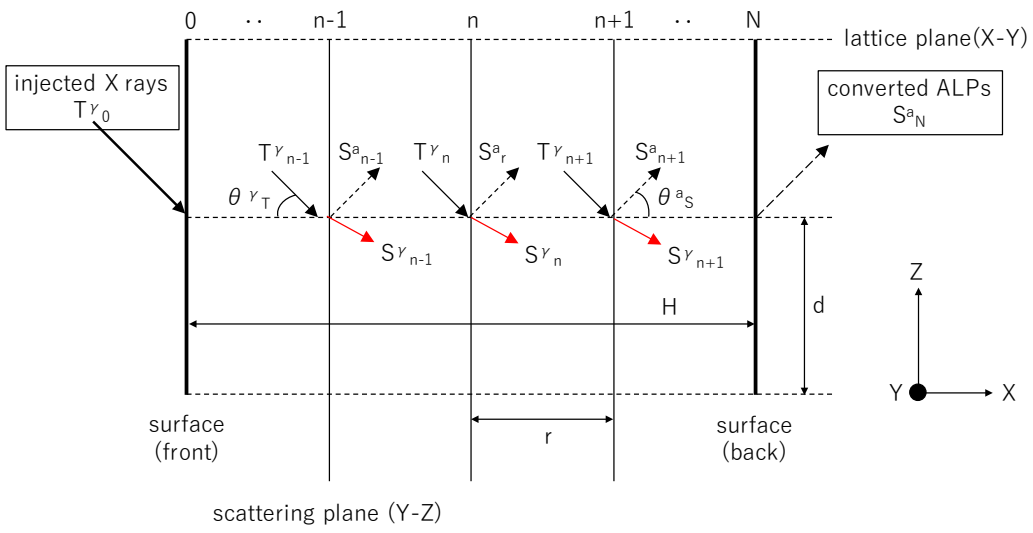

Figure A.6: The X ray-ALP conversion under the Bragg condition of other lattice planes. X-ray diffraction takes place on a plane other than the X-Z plane. See also Fig. A.4.

Appendix B

Higher harmonics' rocking curve

The rocking curve of Si(10,10,0)/third harmonics is also measured during the beam time to evaluate the absolute precision of the goniometer angle. X-ray diffraction of third harmonics additionally has higher sensitivity to the effective shift of the Bragg angle caused by X-ray heat load than fundamental waves. This appendix also provides brief discussion about the effective shift experimentally measured.

B.1 Rocking curve of higher harmonics

This rocking curves with the Bragg angle of $\theta'_{\mathrm{B}} = 18.45$ deg also depends on the detuning angle from θ'_{B} in the same way with the fundamental waves. X-ray diffraction of higher harmonics has much narrower acceptable angular divergence than that of the fundamental waves. The diffraction efficiency of the RR beams is proportional to the following integral,

$$g(\Delta\theta_{\mathrm{B}}) \equiv \int_{-\infty}^{\infty} f(\theta) f(\theta + \Delta\theta_{\mathrm{B}}) d\theta, \tag{B.1}$$

where $f(\theta)$ represents the rocking curve of the R beams. Rocking curve of higher harmonics and higher lattice planes is sensitive to $\Delta\theta_{\mathrm{B}}$ due to the small acceptable angular divergence. Figure B.1 shows the theoretically calculated reflection efficiency of the converter, $f(\theta)$, for the third harmonics/Si(10,10,0) lattice planes and the $\Delta\theta_{\mathrm{B}}$ dependence of the integral, Eq. (B.1). The integral strongly depends on the value of $\Delta\theta_{\mathrm{B}}$ within the range of $\Delta\theta_{\mathrm{B}} = 0 \sim \Delta\theta_{\mathrm{CV}} = 204$ nrad since the width of the rocking curve, 77.1 nrad (FWHM), is smaller enough than $\Delta\theta_{\mathrm{CV}}$. The value of $\Delta\theta_{\mathrm{B}}$ can be also experimentally evaluated from the diffraction efficiencies of the RR beams by changing the X-ray flux injected into the converter since the shift, $\Delta\theta_{\mathrm{B}}$, is proportional to X-ray heat load.

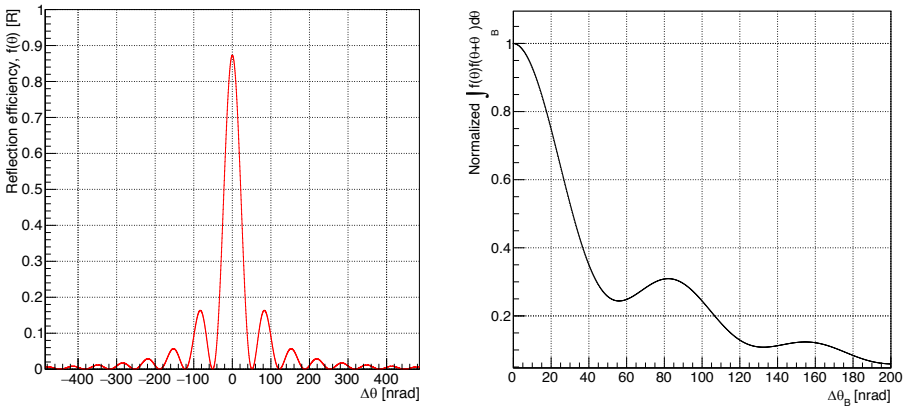

Figure B.1: The theoretically calculated diffraction efficiency of third harmonics. The reflecting lattice planes are Si(10,10,0). Left: the rocking curve of reflected beams, $f(\theta)$. Right: the $\Delta\theta_{\rm B}$ dependence of the integral, $g(\Delta\theta_{\rm B})$, normalized by the value at $\Delta\theta_{\rm B} = 0$. The integral is equivalent to the relative diffraction efficiency of the RR beams.

B.1.1 Method

The rocking curve of the third harmonics (51 keV, RR) is measured by using a NaI detector (OKEN SP-10, Fig. B.2) as shown in Fig. B.3. TRMs are removed in the measurement to enhance the intensity of the third harmonics. The intensity of fundamental waves is $3.784 \pm 0.016 \times 10^{13}$ Hz, and the X-ray heat load on the converter is 64.1 mW in the setup. The NaI detector is installed into EH1 since the RR beams are lowered by 15.8 mm and cannot pass through the downstream optics. The transmitted fundamental waves and higher harmonics are attenuated by a 15 mm-thick stainless steal plate and a 15 mm-thick aluminum plate. The reflected third harmonics are also attenuated by a 2mm-thick copper plate, and X-ray fluorescence from the copper plate is absorbed by a 2mm-thick aluminum plate.

An aluminum plate with a thickness of 1/2 mm is additionally inserted before and after the channel-cut crystal to change the effect of the X-ray heat load, $\Delta\theta_{\rm B}$. The additional aluminum plates with a thickness of 1 and 2 mm attenuate fundamental waves to c_1 =22.6% and c_2 =5.1%, respectively. The count rate of the NaI detector is measured by a single channel analyzer as a function of the detuning angle from $\theta'_{\rm B}$. Background X rays caused by higher harmonics with $n > 3$ are deducted in these rocking curves. The $\Delta\theta_{\rm B}$ under the maximum X-ray heat load will be estimated from the measured $\Delta\theta_{\rm B}$ dependence of the diffraction efficiency and theoretically-calculated one, Fig. B.1.

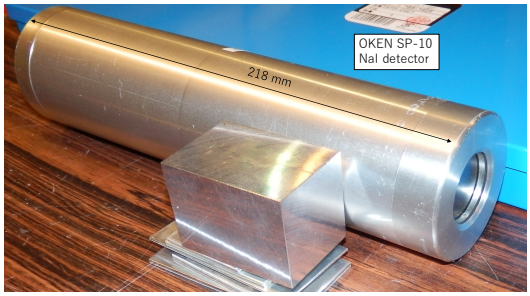

Figure B.2: The NaI detector used to measure the rocking curve of higher harmonics. The detector is composed of a NaI scintillator with a geometry of $\phi 1$ inch$\times t2$ mm and a photomultiplier tube.

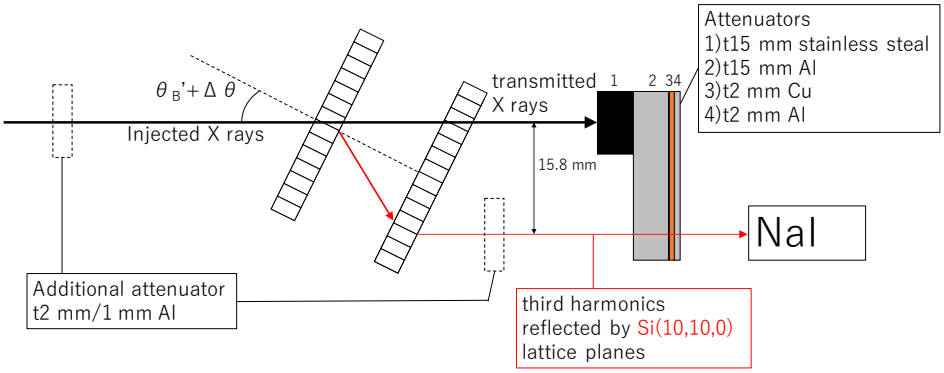

Figure B.3: The measurement of the higher-harmonics rocking curve.

B.1.2 Measured rocking curves

Figures B.4 show the measured rocking curves of the third harmonics. The center of the rocking curve is away from that of Si(660) ($\Delta\theta = 10.95$ deg) by +753190 pulses. The absolute accuracy of the stepping angle is evaluated to be $\pm 0.36\%$ since the difference between them is 7.50525 deg (750525 pulses). The shape of the rocking curve is determined by the beam profile of the third harmonics and the X-ray heat load on the converter.

The diffraction efficiency with an aluminum plate inserted into the upstream of the crystal is enhanced since the intensity and the heat load of injected X rays are reduced. The enhancement factors are evaluated to be $r_1 = 4.26 \pm 0.20$ for the 1 mm-thick aluminum plate and $r_2 = 7.00 \pm 0.34$ for the 2 mm-thick one. These ratios are calculated at the peak of the rocking curve, where the effect of the X-ray heat load is strongest, and the errors are calculated from statistical uncertainties on the diffracted X rays.

The change of the Bragg angle, $\Delta\theta_{\rm B}$, is fitted by using these ratios and the $\Delta\theta_{\rm B}$ dependence of the diffraction efficiency, $g(\Delta\theta_{\rm B})$, shown by Fig. B.1. The fitting

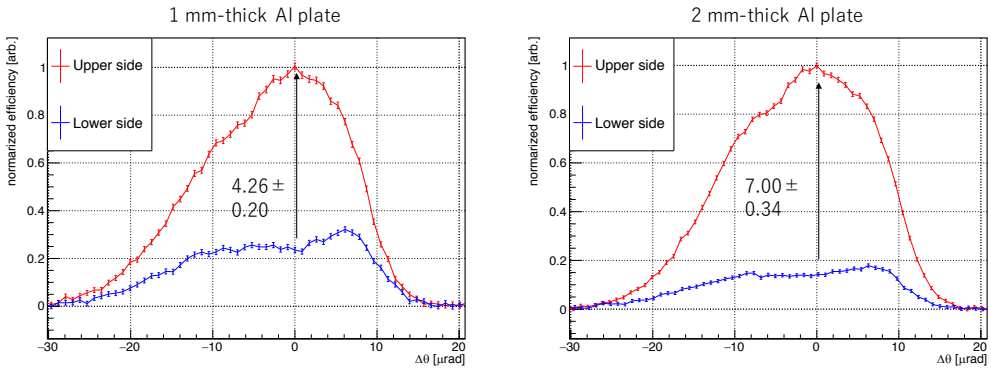

Figure B.4: The measured rocking curves of the third harmonics. The red and blue lines represent the rocking curves with an aluminum plate installed into the upstream and the downstream of the channel-cut crystal, respectively. The rocking curves are normalized by the maxima of the red lines. Left: the thickness of the aluminum plate is 1 mm. Right: 2 mm.

parameter is $\Delta\theta_{\mathrm{B}}$ under the maximum X-ray heat load. The diffraction efficiency under the maximum X-ray heat load is fixed to $g(\Delta\theta_{\mathrm{B}})$, and two data points corresponding to the measurements with aluminum plates, $(c_1\Delta\theta_{\mathrm{B}},\ r_1 g(\Delta\theta_{\mathrm{B}}))$ and $(c_2\Delta\theta_{\mathrm{B}},\ r_2 g(\Delta\theta_{\mathrm{B}}))$, are fitted with $g(\Delta\theta_{\mathrm{B}})$. Figure B.5 shows the result of the fitting. The fitted value of $\Delta\theta_{\mathrm{B}}$ without attenuation plates is 117.42 ± 0.64 nrad.

The fundamental waves passing through the converter (36%) can also warm the re-converter. The temperature rise at the injection point on the re-converter is estimated to be $\sim 3\%$ of the converter from the simulation shown in Sec. 3.8. The fitted value shown above contains this effect, and the $\Delta\theta_{\mathrm{B}}$ of the converter itself is estimated to be 121 nrad.

B.2 Comparison between simulation and experiment

The effective shift of the Bragg angle is evaluated to be $\Delta\theta = -251$ nrad by simulation similar to the one shown in Sec. 3.8. The measured value of $\Delta\theta_{\mathrm{B}}$ is ~ 2 times smaller than the simulated one. The deviation is considered to be caused by the following effects:

1. The heat conduction via the atmosphere may cool the crystal.

2. The simulation approximates the beam profile as a homogeneous rectangular. The approximation enhances the density of the heat load by $\sim 10\%$.

3. The X-ray attenuation length of the third harmonics (L'_{att}=10 mm) is longer than that of fundamental waves. The third harmonics can be reflected at a deeper part of DCM when the crystal lattices close to its surface are thermally

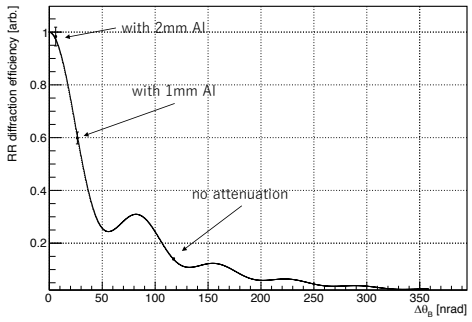

Figure B.5: The change of the Bragg angle fitted from the rocking curve of higher harmonics. The relative vertical and horizontal position of three data points are determined by the X-ray attenuation of aluminum plates, $c_{1,2}$, and the measured ratio of diffraction efficiency, $r_{1,2}$, respectively. The χ^2, NDF and p-value of the fitting are 0.12, 1 and 74%, respectively.

distorted by X rays. The effect heightens the path of the third harmonics by up to $L'_{\rm att}\sin 2\theta'_{\rm BD}$=2.3 mm. The temperature rise and the thermal expansion can be halved at the injection point of the third harmonics if the shift is $\sim$ 2 mm.

The effective shift experimentally measures is considered to be consistent with the simulation shown in Sec. 3.8 by taking into account the effects shown above.

Appendix C

List of symbols

Table C.1 shows the list of main symbols used in this thesis.

Table C.1: List of main symbols used in this thesis (a∼F)

symbol	attribution
a/A	ALP or axion field,
	A is also used as atomic mass number
$a_{1\sim3}$	axises of crystal lattices
$b_{1\sim3}$	parameters of the Moliére approximation
$B_{(0)}$	magnetic field (strength)
	or parameter of the Debye-Waller factor
$c_{1/2}$	X-ray attenuation by aluminum plates
$CL(C.L.)$	confidence level
$C_{\alpha/\beta}$	amplitudes of the Bloch waves
d_{hkl}	lattice constant of (hkl) lattice planes
d_n	neutron electric dipole moment (nEDM)
$d_{(0\sim3)}$	lattice constants of crystals
D	reduction factor due to detuning
e	elementary charge or the Napier number
E	electric field, electromagnetic anomaly,
	or energy of X-ray and electron beams
E_T	effective electric field within conversion crystals
$f_{a/A}$	symmetry breaking scale of additional $U(1)$ symmetries
f_π	pion decay constant
F	the Fano factor
F_c	coefficient of crystal structure factors
$F_{\gamma/a}$	atomic structure factor and form factor of the conversion

continued on the next page...

continued from the previous page...

symbol	attribution
$\mathcal{F}^{\mu\nu}/\tilde{\mathcal{F}}_{\mu\nu}$	electromagnetic field strength tensor and its dual
$g_{a\gamma\gamma}/g_{A\gamma\gamma}$	ALP/axion-two photon coupling constant
g_s	strong coupling constant
$\mathcal{G}^{b\mu\nu}/\tilde{\mathcal{G}}^b_{\mu\nu}$	gluonic field strength tensor and its dual
h	the Plank constant
(hkl)	lattice index
(h', k', l')	lattice index of the sub peak
H	thickness of conversion crystals
$\mathbf{H}$	momentum transfer vector
i	imaginary unit
I	DC-like current from PIN photodiodes
k_a	wavenumber of ALPs
k_{B}	the Boltzmann constant
$k_{T/S}$	wavenumber of transmitted/converted waves
k_γ	wavenumber (equivalent to energy) of photons
$\mathbf{k_{0/g}}$	wavenumber vectors of injected/diffracted X rays
K	property of the undulator
L	X-ray path length within conversion crystals
L_{att}	X-ray attenuation length
$L_{\mathrm{att},\alpha/\beta}$	attenuation lengths of the Bloch waves
L_{B}	conversion length of Bragg-case conversion
L_{CV}	length of magnetic fields
L_{eff}	effective conversion length
$L_{\mathrm{eff},\alpha/\beta}$	effective conversion lengths of the Bloch waves
L_T	path length of X rays/ALPs within conversion crystals
$m_{a/A}$	ALPs' or Axion's mass
m_{a_n}	mass of Kaluza-Klein axions
m_{atom}	atomic mass
m_e	electron mass
$m_{u/d}$	up and down quark mass
m_γ	plasma frequency
m_π	pionic mass
M	quark mass matrix, atomic density on scattering planes, or exponent of the Debye-Waller factor
M_F	fundamental scale of string theory
n	X-ray refractive index, or an integer
$\bar{n}_a$	mean number density of Kaluza-Klein axions

continued on the next page...

continued from the previous page...

symbol	attribution
$n_{1...\delta}$	integers labeling Kaluza-Klein axions
N	number of scattering planes
N_{BG}	number of environmental X rays
N_γ^i	total number of injected X rays at i pulses
$N_\gamma^{\prime i}$	sum of N_γ^i within the $\Delta\theta$ window
N_i^s	number of detected signal X rays at i pulses
$N_{i,CL}^s$	upper limit on the number of detected signal X rays
N_γ	number of injected photons
P	polarization factor
$P_{\gamma\leftrightarrow a}$	conversion and reconversion efficiency
P^2	conversion-reconversion probability
q	momentum transfer
q_T	reciprocal lattice spacing
q_x	momentum transfer in the x direction
r	spacing of scattering planes
r_e	classical electron radius
$r_{1,2}$	enhancement factors of higher-harmonics diffraction efficiency
R	compactification radius of extra dimensions
R_a	production rate of gravitationally-trapped solar ALPs
$R_{S/M}$	simulated/measured detection efficiency of the Ge detector
$R/r_{\tau\epsilon}$	distance from the origin of the conversion
$R_\odot$	solar radius
s	model-dependent parameter of ALPs
$S_n^{\gamma/a}$	amplitudes of converted X rays/ALPs at n^{th} scattering plane
t_{DAQ}	data acquisition time per pulse
t_{il}	thickness of the insensitive layer on the Ge detector
$t_{\mathrm{T/S}}$	flight time of transmitted/converted waves
T	temperature
T_{DAQ}	data acquisition time
$T_n^{\gamma/a}$	amplitude of transmitted X rays/ALPs at n^{th} scattering plane
u	parameter of the Bloch waves
V	volume of unit cells
$W_{\mathrm{Si/Ge}}$	work functions of Si/Ge
$x_{\alpha/\beta}$	characteristic functions of the Bloch waves
z	ratio of up and down quark mass
Z	atomic number

continued on the next page...

continued from the previous page...

symbol	attribution
α_c	critical angle of X-ray total refraction
α_l	linear thermal expansion coefficient
$\alpha_{(s)}$	(strong) fine-structure constant
$\alpha_{1\sim3}$	parameters of the Moliére approximation
$\beta_{1\sim3}$	parameters of the Moliére approximation
γ	Lorentz factor
δ	number of extra dimensions, or reduction factor of X-ray refractive index from the unity
Δd	fluctuation of lattice constants within a perfect crystal
ΔE_{FW}	acceptable bandwidth of DCM
Δm_γ	correction to plasma frequency due to X-ray diffraction
ΔT	temperature rise due to X-ray heat load
$\Delta\theta$	detuning angle from the Bragg angle
$\Delta\theta_{\mathrm{B(d/R/T)}}$	shifts of the Bragg angle due to Δd, X-ray refraction and heat load
$\Delta\theta_{\mathrm{BL}}$	effective angular divergence of injected X rays
$\Delta\theta_{\mathrm{CV}}$	required parallelism between lattice planes within conversion crystals
$\Delta\theta_{\mathrm{D}}$	drift of the goniometer angle during data takings
$\Delta\theta_{\mathrm{FW}}$	acceptable angular divergence of DCM
$\Delta\theta_{\mathrm{i}}$	detuning angle at i pulses
$\Delta\theta_{\mathrm{S}}$	measured angular position of the sub peak
$\Delta\phi_{\gamma/a}$	phase differences of X-ray scattering and X ray-ALP conversion
ϵ	infinitesimal value
ϵ_d	detection efficiency of signal photons
ϵ_{PIN}	detection efficiency of PIN photodiodes
ϵ_S	reduction of reconversion probability due to X-ray heat load
$\epsilon_{0/s}$	polarization vector of injected/diffracted X rays
$\zeta^{(\prime)}_{(jk)}$	conversion/reconversion amplitudes
$\eta_{(T/S)}$	X-ray scattering amplitude
$\eta_{(T/S)0}$	X-ray forward scattering amplitude
$\theta/\bar{\theta}$	phase parameter of QCD
θ_{B}	the Bragg angle
$\theta^{(\prime)}_{\mathrm{BD}}$	the Bragg angle of DCM (with X-ray refraction)
$\theta_{\mathrm{T/S}}$	angle of injected/converted ALPs/X rays
$\theta^{\gamma}_{\mathrm{TD}}$	X-ray injection angle to DCM
$\theta^{\gamma/a(A)}_{T/S}$	angles of transmitted/scattered X rays/ALPs(axion)
Θ_{D}	the Debye temperature

continued on the next page...

continued from the previous page...

symbol	attribution
κ	ratio of imaginary parts of X-ray scattering amplitudes
$\lambda_{T/S}$	wavelengths of injected/converted ALPs/X rays
λ_u	magnetic period of undulators
$\lambda_{\gamma/a(A)}$	wavelength of X rays and ALPs(axion)
λ_1	wavelength of fundamental X rays
μ_{Ge}	X-ray attenuation coefficient of germanium
π	number π, polarization state
π_0	neutral pion
ρ	electron density of the media in which X rays propagate
σ	energy resolution of the Ge detector, polarization state or standard deviation
σ_0	electric noise of the Ge detector
τ	infinitesimal value
ϕ	azimuth angle, an exotic scalar field or atomic electric potential
ϕ'	parameter of the Debye-Waller factor
$\phi_{\gamma/a}$	phases of X-ray scattering and X ray-ALP conversion
$\phi_{T/S}^{\gamma/a}$	phases corresponding to the propagation between scattering planes
ω	X-ray photon energy
ω_1	X-ray photon energy of fundamental waves

End.

Acknowledgements

Firstly, I would like to express the deepest appreciation to my supervisor Prof. Shoji Asai for providing me with generous support and the opportunity for performing experiments including the one described in this thesis. Without his continued guidance and encouragement, this thesis would not have been possible.

Also I would like to show my greatest gratitude to Associate Prof. Toshio Namba. He has been extraordinary tolerant and supportive from the begging to the end of my course. I owe a great deal to him for techniques and the way of thinking as experimentalists.

I would like to offer my special thanks to Associate Prof. Takayuki Yamazaki for his cooperation in the theoretical calculation and the basic experimental design described in this thesis. He provides me with insightful feedbacks which greatly sophisticate the theory and the experiment.

Special thanks also to Mr. Yudai Seino for helping me with performing the experimental program during the beam time of BL19LXU.

The experiment has been performed in cooperation with researchers of SPring-8/SACLA. In particular, I owe a very important debt to the BL19LXU manager Prof. Kenji Tamasaku for the revision of the theory and the experiment at BL19LXU. Also I would like to offer my special thanks to Prof. Yuichi Inubushi, Prof. Kei Sawada, Prof. Yoshihito Tanaka for useful discussions about X-ray physics and optics.

I would also like to thank all the staffs and students of International Center for Elementary Particle Physics for living a fruitful researching time. In particular the discussion with Associate Prof. Akira Ishida and Dr. Toshiaki Inada provides we with great help.

Finally, I would like to express my gratitude to my family, who always support me absolutely and unconditionally.

The research described in this thesis is funded by the Japan Society for Promotion of Science (Grant number 15J00509), and the experiment at BL19LXU is approved by RIKEN with the proposal number of 20170021.

Bibliography

[1] T. Yamaji et al., Phys. Rev. D **96**, 115001 (2017).

[2] G. 't Hooft, Phys. Rev. Lett. **37**, 8 (1976).

[3] G. 't Hooft, Phys. Rev. D **14**, 3432 (1976).

[4] R. Jackiw and C. Rebbi, Phys. Rev. Lett. **37**, 172 (1976).

[5] C. G. Callan et al., Phys. Lett. B **63**, 334 (1976).

[6] J. Jaeckel and A. Ringwald, Ann. Rev. Nucl. Part. Sci. **60**, 405 (2010).

[7] P. W. Graham et al., Ann. Rev. Nucl. Part. Sci. **65**, 485 (2015).

[8] C. A. Baker et al., Phys. Rev. Lett. **97**, 131801 (2006).

[9] J. M. Pendlebury et al., Phys. Rev. D **92**, 092003 (2015).

[10] R. D. Peccei and H. R. Quinn, Phys. Rev. Lett. **38**, 1440 (1977).

[11] R. D. Peccei and H. R. Quinn, Phys. Rev. D **16**, 1791 (1977).

[12] S. Weinberg, Phys. Rev. Lett. **40**, 223 (1978).

[13] F. Wilczek, Phys. Rev. Lett. **40**, 279 (1978).

[14] W. A. Bardeen and S. H. H. Tye, Phys. Lett. B **76**, 580 (1978).

[15] W. A. Bardeen, R. D. Peccei, and T. Yanagida, Nucl. Phys. B **279**, 401 (1987).

[16] H. Leutwyler, Phys. Lett. B **378**, 313 (1996).

[17] H. Primakov, Phys. Rev. **81**, 899 (1951).

[18] K. V. Bibbler et al., Phys. Lett. B **59**, 759 (1987).

[19] W. A. Bardeen, S. H. H. Tye, and J. A. M. Vermaseren, Phys. Lett. B **74**, 229 (1978).

[20] D. B. Kaplan, Nucl. Phys. B **260**, 215 (1985).

[21] M. Srednicki, Nucl. Phys. B **260**, 689 (1985).

[22] J. E. Kim, Phys. Rev. Lett. **43**, 103 (1979).

[23] M. A. Shifman, A. I. Vainshtein, and V. I. Zakharov, Nucl. Phys. B **166**, 493 (1980).

[24] A. R. Zhitnitsky, Sov. J. Nucl. Phys. **31**, 260 (1980).

[25] M. Dine, W. Fischler, and M. Srednicki, Phys. Lett. B **104**, 199 (1981).

[26] J. E. Kim and G. Carosi, Rev. Mod. Phys. **82**, 557 (2010).

[27] A. Ringwald, arXiv:1407.0546 (2014).

[28] Y. Chikashige, R. N. Mohapatra, and R. D. Peccei, Phys. Lett. B **98**, 265 (1981).

[29] G. B. Gelmini and M. Roncadelli, Phys. Lett. B **99**, 411 (1981).

[30] F. Wilczek, Phys. Rev. Lett. **49**, 1549 (1982).

[31] Z. G. Berezhiani and M. Y. Khlopov, Sov. J. Nucl. Phys. **51**, 739 (1990).

[32] J. Jaeckel, Phys. Lett. B **732**, 1 (2014).

[33] E. Witten, Phys. Lett. B **149**, 351 (1984).

[34] J. P. Conlon, J. High Energy Phys. **0605**, 078 (2006).

[35] P. Svrček and E. Witten, J. High Energy Phys. **06**, 051 (2006).

[36] P. Arias et al., Astropart. Phys. **1206**, 013 (2012).

[37] A. Ringwald, Phys. Dark Universe **1**, 116 (2012).

[38] M. Meyer, D. Horns, and M. Raue, Phys. Rev. D **87**, 035027 (2013).

[39] G. I. Rubtsov and S. V. Troitsky, JETP Lett. **100**, 355 (2014).

[40] J. Isern et al., AstroPhys. J. **682**, L109 (2008).

[41] A. Arvanitaki et al., Phys. Rev. D **81**, 123530 (2010).

[42] B. S. Acharya et al., JHEP **11**, 105 (2010).

[43] M. Cicoli et al., J. High Energy Phys. **10**, 146 (2012).

[44] L. DiLella and K. Zioutas, Astropart. Phys. **19**, 145 (2003).

[45] L. DiLella, Phys. Rev. D **62**, 125011 (2000).

[46] T. R. Burnight, Phys. Rev. **76**, 165 (1949).

[47] H. Friedman et al., Phys. Rev. **83**, 1025 (1951).

[48] R. Tousey et al., Phys. Rev. **83**, 792 (1951).

[49] J. H. M. M. Schmitt, Astron. Astrophys. **318**, 215 (1997).

[50] V. Krasnoselskikh et al., Astron. Astrophys. **382**, 713 (2002).

[51] J. H. M. M. Schmitt et al., Nature **349**, 583 (1991).

[52] L. Spitzer and Jr., AstroPhys. J. **124**, 20 (1956).

[53] R. Giacconi et al., Phys. Rev. Lett. **9**, 439 (1962).

[54] C. S. Bowyer et al., Nature **223**, 573 (1969).

[55] J. Trümper, Q. J. R. Astr. Soc **33**, 165 (1992).

[56] G. G. Raffelt, Phys. Rev. D **33**, 897 (1986).

[57] G. G. Raffelt and D. S. P. Dearborn, Phys. Rev. D **36**, 2211 (1987).

[58] J. W. Brockway et al., Phys. Lett. B **383**, 439 (1996).

[59] J. A. Grifols et al., Phys. Rev. Lett. **77**, 2372 (1996).

[60] S. DePanfilis et al., Phys. Rev. Lett. **59**, 839 (1987).

[61] W. Wuensch et al., Phys. Rev. D **40**, 3153 (1989).

[62] C. Hagmann et al., Phys. Rev. D **42**, 1297 (1990).

[63] J. Hoskins, Phys. Rev. D **84**, 121302 (2011).

[64] M. Arik et al., Phys. Rev. D **92**, 021101 (2015).

[65] F. T. Avignone et al., Phys. Rev. Lett. **81**, 5068 (1998).

[66] A. Morales et al., Astropart. Phys. **16**, 325 (2002).

[67] Z. Ahmed et al., Phys. Rev. Lett. **103**, 141802 (2009).

[68] R. Bernabei et al., Phys. Lett. B **515**, 6 (2001).

[69] P. Astier et al., Phys. Lett. B **479**, 371 (2000).

[70] K. Ehret et al., Phys. Lett. B **689**, 149 (2010).

[71] R. Ballou et al., Phys. Rev. D **92**, 092002 (2015).

[72] F. D. Valle et al., Eur. Phys. J. C **76**, 24 (2016).

[73] G. G. Raffelt, Phys. Lett. B **166**, 402 (1986).

[74] J. Isern et al., AstroPhys. J. **682**, L109 (2008).

[75] G. G. Raffelt, Lect. Notes Phys. **741**, 51 (2008).

[76] P. Skivie, Phys. Rev. Lett. **51**, 1415 (1983).

[77] Y. Inoue et al., Phys. Lett. B **668**, 2 (2008).

[78] J. Jaeckel et al., Phys. Rev. D **75**, 013004 (2007).

[79] R. N. Mohapatra and S. Nasri, Phys. Rev. Lett. **98**, 050402 (2007).

[80] H. Schlattl, A. Weiss, and G. G. Raffelt, Astropart. Phys. **10**, 353 (1999).

[81] O. Halpern, Phys. Rev. **44**, 855 (1933).

[82] B. D. Tollis, Nuovo Cimento **32**, 757 (1964).

[83] B. D. Tollis, Nuovo Cimento **35**, 1182 (1965).

[84] A. Cadéne et al., Eur. Phys. J. D. **68**, 16 (2014).

[85] J. Redondo and A. Ringwald, Comtemp. Phys. **52**, 211 (2011).

[86] G. Ruoso et al., Z. Phys. C **56**, 505 (1992).

[87] R. Cameron et al., Phys. Rev. D **47**, 3707 (1993).

[88] C. Robilliard et al., Phys. Rev. Lett. **99**, 190403 (2007).

[89] M. Fouché et al., Phys. Rev. D **78**, 032013 (2008).

[90] A. S. Chou et al., Phys. Rev. Lett. **100**, 080402 (2008).

[91] A. Afanasev et al., Phys. Rev. Lett. **101**, 120401 (2008).

[92] A. Afanasev et al., Phys. Lett. B **679**, 317 (2008).

[93] K. Ehret et al., Nucl. Instrum. Methods Phys. Res. Sect. A **612**, 83 (2009).

[94] P. Pugnat et al., Phys. Rev. D **78**, 092003 (2008).

[95] R. Rabadán, A. Ringwald, and K. Sigurdson, Phys. Rev. Lett. **96**, 110407 (2006).

[96] A. G. Dias and G. Lugones, Phys. Lett. B **673**, 101 (2009).

[97] R. Battesti et al., Phys. Rev. Lett. **105**, 250405 (2010).

[98] T. Inada et al., Phys. Rev. Lett. **118**, 071803 (2017).

[99] W. Buchmüller and F. Hoogeveen, Phys. Lett. B **237**, 278 (1990).

[100] W. Liao, Phys. Lett. B **702**, 55 (2011).

[101] E. A. Paschos and K. Zioutas, Phys. Lett. B **323**, 367 (1994).

[102] R. J. Creswick et al., Phys. Lett. B **427**, 235 (1998).

[103] G. Borrmann, Z. Phys. **127**, 297 (1950).

[104] M. von Laue, Acta. Cryst. **2**, 106 (1949).

[105] U. Bonse and M. Hart, Appl. Phys. Lett. **6**, 155 (1965).

[106] M. Yabashi et al., Nucl. Instrum. Methods Phys. Res. Sect. A **678**, 467 (2001).

[107] T. Tanaka, SPring-8/SACLA INFORMATION **6**, 113 (2001).

[108] M. Yabashi et al., Proc. SPIE **3773**, 2 (1999).

[109] H. Yamazaki et al., Nucl. Instrum. Methods Phys. Res. Sect. A **467**, 643 (2001).

[110] T. Inada et al., Phys. Lett. B **732**, 356 (2014).

[111] F. Scholze et al., Nucl. Instrum. Methods Phys. Res. Sect. A **439**, 208 (2000).

[112] M. A. Hopcroft et al., J. Microelectromech. Sys. **19**, 229 (2010).

[113] K. Tamasaku et al., SPring-8 INFORMATION **6**, 390 (2001).

[114] A. O. Hanson et al., Phys. Rev. **84**, 634 (1951).

[115] B. Gottchalk et al., Nucl. Instrum. Methods Phys. Res. Sect. B **74**, 467 (1993).

[116] J. P. Desclaux, Computer Phys. Commun. **9**, 31 (1975).

[117] M. Zhabitsky, DIRAC Note **06**, 1 (2014).

[118] N. Oka et al., Prog. Theor. Exp. Phys. **2017**, 103 (2017).

[119] M. Gliozzi et al., Astron. Astrophys. **377**, 44 (2001).

[120] T. J. Turner et al., AstroPhys. J. **561**, 131 (2001).

[121] F. Frontera et al., AstroPhys. J. **561**, 1006 (2001).

[122] G. Matt et al., Astron. Astrophys. **377**, 31 (2002).

[123] P. Romano et al., AstroPhys. J. **564**, 162 (2002).

[124] E. Bulbul et al., AstroPhys. J. **789**, 13 (2014).

[125] B. E. Warren, *X-ray diffraction*, Addison-Wesley, MA, 1969.

[126] G. Moliére, Z. Nat **2**, 133 (1947).

[127] V. N. Barier, V. M. Katkov, and V. M. Strakhovenko, *Electromagnetic Processes at High Energies in Oriented Crystals*, World Scientific, Singapore, 1998.